



HAL
open science

Supernova remnants as PeVatron candidates : analysis and modeling of simulated data from the Cherenkov Telescope Array

Ziwei Ou

► **To cite this version:**

Ziwei Ou. Supernova remnants as PeVatron candidates : analysis and modeling of simulated data from the Cherenkov Telescope Array. High Energy Astrophysical Phenomena [astro-ph.HE]. Université Paris-Saclay, 2019. English. NNT : 2019SACLS421 . tel-02493037

HAL Id: tel-02493037

<https://theses.hal.science/tel-02493037>

Submitted on 27 Feb 2020

HAL is a multi-disciplinary open access archive for the deposit and dissemination of scientific research documents, whether they are published or not. The documents may come from teaching and research institutions in France or abroad, or from public or private research centers.

L'archive ouverte pluridisciplinaire **HAL**, est destinée au dépôt et à la diffusion de documents scientifiques de niveau recherche, publiés ou non, émanant des établissements d'enseignement et de recherche français ou étrangers, des laboratoires publics ou privés.

Supernova remnants as PeVatron candidates: analysis and modeling of simulated data from the Cherenkov Telescope Array

Thèse de doctorat de l'Université Paris-Saclay
préparée à l'Université Paris-Sud

Ecole doctorale n°576 Particules, Hadrons, Énergie, Noyau, Instrumentation, Imagerie,
Cosmos et Simulation (PHENIICS)
Spécialité de doctorat : Astroparticules et Cosmologie

Thèse présentée et soutenue à Orsay, le 5 Novembre 2019, par

ZIWEI OU

Composition du Jury :

Pierre Desesquelles Professeur (LPGP, Université Paris-Sud)	Président
Corinne Berat Directeur de Recherche (LPSC, CNRS)	Rapporteur
Zahia Djouadi Maître de Conférences (IAS, Université Paris-Sud)	Rapporteur
Arache Djannati-Atai Directeur de Recherche (APC, CNRS)	Examineur
Jonathan Biteau Maître de Conférences (IPN, Université Paris-Sud)	Co-encadrant
Tiina Suomijarvi Professeur (IPN, Université Paris-Sud)	Directrice de thèse

Résumé

L'origine du genou dans le spectre des rayons cosmiques aux énergies autour du PeV reste une question ouverte. En raison de leur budget énergétique élevé, les restes de supernovae (SNR) sont des candidats plausibles pour ces dénommés PeVatrons. Les particules chargées accélérées interagissent avec la matière environnante et produisent des pions neutres qui se désintègrent ensuite en rayons γ de haute énergie. Ces rayons γ , qui sont aux énergies du TeV pour les PeVatrons, peuvent ensuite être détectés par des télescopes Cherenkov ou d'autres observations en rayons γ . Dans ce travail de thèse, nous étudions le potentiel du réseau de télescopes Cherenkov CTA à observer de tels rayons γ . Après avoir sélectionné les candidats potentiels PeVatrons Galactiques présents dans le Data Challenge One (DC-1) de CTA, nous reconstruisons leur distribution spectrale d'énergie (SED) à l'aide du package ctools. Si des données mesurées existent à d'autres longueurs d'onde, nous les combinons aux SED simulés pour effectuer une analyse multi-longueur d'onde (MWL). Les SED sont ensuite ajustées à l'aide de différents modèles radiatifs non thermiques mis en oeuvre dans le logiciel Naima, en particulier la composante pion neutre hadronique. Plusieurs résultats sont obtenus. Les paramètres spectraux reconstruits sont en bon accord avec les paramètres utilisés dans le DC-1. Les simulations donnent ainsi confiance dans le processus d'analyse des données. Parmi les SNRs étudiés, certains candidats PeVatrons potentiels ayant des spectres d'énergie durs sont trouvés. Il est également montré que les données MWL donnent une bonne contrainte pour la modélisation des SED et permettent de déterminer si une composante hadronique est présente dans les données. Si les spectres des SNRs observables avec CTA suivaient ceux simulés pour le DC-1, nous pourrions exclure la plupart des sources en tant que PeVatrons. La combinaison des données de *Fermi*-LAT et des données CTA permettrait cependant de contraindre ou de mesurer les contributions relatives hadroniques et leptoniques à l'émission γ des SNRs. Des améliorations possibles des modèles spectraux à simuler pour le prochain Data Challenge de CTA sont proposées.

Abstract

The origin of the knee in the cosmic-ray spectrum at PeV energies is still an open question. Due to their large energy budget, Supernova Remnants (SNRs) are plausible candidates for these so-called PeVatrons. The accelerated charged particles interact with surrounding matter and produce π^0 particles that consequently decay into high-energy γ rays. These γ rays, which are at TeV energies for PeVatrons, can then be detected by Cherenkov telescopes or other γ -ray observations. In this thesis work, we study the potential of the Cherenkov Telescope Array (CTA) to observe such γ rays.

After selecting potential Galactic PeVatron candidates present in the simulated Data Challenge One (DC-1) of CTA, we reconstruct their spectral energy distribution (SED) by using the *ctools* package. In case measured data at other wavelengths exist, we combine them to the simulated SEDs to perform Multi-Wavelength (MWL) analysis. The SEDs are then fitted by using different non-thermal radiative models implemented in *Naima* package, including hadronic π^0 component.

Several results are obtained. The spectral parameters are reconstructed in good agreement with parameters used in DC-1. Simulations thus give confidence in the data analysis process. Some potential PeVatron candidates having hard energy spectra are found among the studied SNRs. It is also shown that the MWL data gives good constrain for SED modelling and allows us to determine whether a hadronic component is present in the data. If the spectra of SNRs observable by CTA followed the DC-1 simulation, we could rule out most of the sources as PeVatrons. The combination of *Fermi*-LAT data with CTA data would at the same time enable firm constraints on or measurements of the hadronic and leptonic relative contributions to the γ -ray emission of SNRs. Possible improvements in the input spectral models to be simulated for the next Data Challenge of CTA are proposed.

Introduction

Cosmic rays (CRs) carry information on the most energetic processes in the universe. The energy spectrum of CRs up to 10^{20} eV has been measured with high precision. There is a break in the all-particle energy spectrum around 4×10^{15} eV (4 PeV) which is called the ‘knee’. The origin of the knee of the CR spectrum is still an open question. CRs with energy up to a few PeV are thought to originate from accelerators in our Galaxy, which are called PeVatrons. Supernova remnants (SNRs) are one kind of potential astrophysical accelerators expected to accelerate CRs up to the knee and are thus PeVatron candidates. Most detected γ -ray SNRs locate in the Galactic Plane. Therefore, low Galactic latitude SNRs are primary targets.

Cosmic rays being charged particles, they are deflected by magnetic fields, thus losing the directional information on their sources. Accelerated charged particles produce electromagnetic (EM) radiation. Constraining the energy distribution of EM radiation is a key to unveil the acceleration of the parent charged particles. In the EM spectrum, very-high-energy (VHE) γ -rays (30 GeV to 300 TeV) have opened ‘the last window’. This EM window is relative to particle acceleration from TeV to PeV energies. The acceleration of electrons to hundreds of TeV has been supported by γ -ray observations. However, the acceleration of protons to PeV energies, where they are expected to contribute to the all-particle cosmic-ray spectrum, is still an open question.

γ -rays from SNRs have been detected by the space telescope *Fermi-LAT* and by ground-based γ -ray telescopes (e.g. H.E.S.S., MAGIC, VERITAS). The interactions of γ -rays in the atmosphere produce showers of secondary particles, inducing the emission of Cherenkov light. Thanks to Imaging Atmospheric Cherenkov Telescopes (IACT), γ -rays from 30 GeV to 300 TeV can be detected on the ground. However, they have not yet uncovered direct evidence for CR acceleration in SNRs up to the knee. The Cherenkov Telescope Array (CTA) is a next-generation IACT with better sensitivity and broad energy range. It can find much more sources compared to current IACTs and, most importantly for PeVatron searches, reconstruct their spectral and morphological properties with unprecedented accuracy. With detected energies up to 300 TeV, CTA will be a powerful instrument for searching PeVatrons.

This thesis presents a study of TeV SNRs as PeVatron candidates, in preparation for CTA first light. The aim is to identify the best PeVatron candidates among SNRs detected by current-generation IACTs, model their spectral energy distribution (SED) with radiative models, includ-

ing leptonic and hadronic components, and determine the spectrum of accelerated particles. In particular, the maximum energy reached by the proton spectrum, or proton cutoff energy, appears to be a key parameter to sort the PeVatron candidates.

This work is organized as follows. In chapter 1, an introduction of γ -ray astronomy and its relation with CR observations are presented. Chapter 2 summarizes the basic concepts involved in the detection of γ -rays by IACTs, through the Extensive Air Showers produced by γ -rays in the atmosphere. In that respect, the performance of CTA and the corresponding science case will be outstanding. In chapter 3, one of analysis pipelines developed for CTA, *ctools*, and its application to the first data challenge (DC-1) of the CTA Consortium are presented. We reconstruct with *ctools* spectra of SNRs simulated in DC-1 to assess the potential of this upcoming observatory to detect emission up to the highest γ -ray energies. In chapter 4, different non-thermal radiative processes, of leptonic and hadronic origin, are fit to multi-wavelength data to constrain the underlying particle populations. We conclude on the potential of CTA to constrain PeVatrons and propose possible improvements in the preparation for their search.

In addition to working on PeVatrons, part of this thesis was dedicated to variability studies of AGN within the CTA Consortium. This work is summarized in the proceedings in Appendix B, published by the French Society of Astronomy and Astrophysics (SF2A).

Acknowledgement

I would like to thank my supervisor, Tiina Suomijarvi, who gives the support on research, life and future. I acknowledge the support of Jonathan Biseau, who gives lots of help for my PhD study. I express my gratitude to all my family and my friends for their support.

I am indebted to Zizhao Zong, Barbara Biasuzzi and Pooja Sharma; to all the staff in IPN Orsay, especially for Jean-Yves Zana, Nathalie Cherel, Laure-Amelie Couturie, Vincent Lafage, David Verney and Elisabeth Seibert; to all the members in CTA Collaboration, especially for the Galactic Science Working Group and the AGN Working Group; to Miguel Araya (Universidad de Costa Rica), Bingbing Wang (IHEP, China) for helping me to understand *Naima*, to Matteo Gioni (DESY) for helping me to compute AGN visibility, to Luigi Tibaldo (IRAP) for helping me to understand *ctools*; to Corinne Berat and Zahia Djouadi as Rapporteur, Pierre Desesquelles and Arache Djannati-Atai as Examineur.

Contents

1	Gamma-ray Astronomy	17
1.1	CR Observations	17
1.2	Acceleration of CRs	18
1.3	Propagation of Radiation	19
1.4	Gamma-ray Astronomy	20
1.4.1	Gamma-ray AGN	23
1.4.2	Gamma-ray Supernova Remnants	24
1.4.3	Gamma-ray Pulsars	27
1.4.4	Diffuse Gamma-ray Emissions	27
1.5	CTA Science	27
1.6	A Brief Summary	29
2	Extensive Air Showers and Experimental Technique	31
2.1	Gamma-ray Detectors	31
2.1.1	Space-based Gamma-ray Detectors	31
2.1.2	Ground-based Gamma-ray Detectors	32
2.1.2.1	Electromagnetic Cascades	32
2.1.2.2	Cherenkov Radiation	32
2.1.3	Reconstruction of the Parameters of the Showers for IACTs	36
2.1.4	Performance of IACTs	37
2.2	Cherenkov Telescope Array	40
2.2.1	Telescopes	40
2.2.2	CTA Performance	40
2.3	A Brief Summary	42
3	Data Analysis	43
3.1	Analysis Chain	43
3.1.1	Selection of observations and model building	45
3.1.2	Generation of data and instrument model cube	46
3.1.3	Source model	47

3.1.4	Reconstruction of a source best-fit model	48
3.2	Supernova remnants simulated in the DC-1 of CTA	50
3.2.1	The Galactic Plane Survey of DC-1	50
3.2.2	Candidate PeVatrons in DC-1	50
3.2.3	Distance Measurement	51
3.3	Supernova remnants reconstructed from DC-1	52
3.3.1	Analysis of a typical source: HESS J1614+516	52
3.3.2	Analysis of DC-1 PeVatron candidates	57
3.3.3	DC-1 spectra and visibility of PeVatron candidates	58
3.4	Conclusion	67
4	Comparison to Radiative Models	71
4.1	Radiative Models	71
4.1.1	Bremsstrahlung	72
4.1.2	Compton and Inverse Compton Scattering	72
4.1.3	Synchrotron Radiation	73
4.1.4	Pion-decay	74
4.2	Maximum Likelihood, Monte Carlo Markov Chain and Naima	74
4.2.1	Model Fitting with Naima	74
4.2.2	Radiative Model Parameters	75
4.3	Multi-wavelength Analysis Results	77
4.3.1	Group (1): With X-ray, <i>Fermi</i> -LAT and DC-1 Data	82
4.3.1.1	RX J1713.7-3946	82
4.3.1.2	HESS J1731-347	83
4.3.1.3	W 49B	84
4.3.1.4	Conclusions for group (1)	84
4.3.2	Group (2): With <i>Fermi</i> -LAT and DC-1 Data	85
4.3.2.1	HESS J1745-303	86
4.3.2.2	HESS J1800-240A	87
4.3.2.3	W 28	88
4.3.2.4	W 51C	89
4.3.2.5	Conclusions for group (2)	89
4.3.3	Group (3): With DC-1 Data Only	89
4.3.3.1	HESS J1614-518	90
4.3.3.2	HESS J1912+101	91
4.3.3.3	Conclusions for group (3)	91
4.4	Possible Improvements for DC-1	96
4.5	Discussion	98
4.6	Conclusion	100

A	Comparison of spectra between H.E.S.S. and DC-1	105
B	AGN flare simulation	111
	Bibliography	117

Glossary

4FGL The Fourth *Fermi* Large Area Telescope Catalog.

AGILE Astro rivelatore Gamma a Immagini Leggero.

AGN Active Galactic Nuclei.

AMS-02 Alpha Magnetic Spectrometer.

CMB Cosmic Microwave Background.

DSA Diffusive Shock Acceleration.

EAS Extensive Air Shower.

EBL Extragalactic Background Light.

ECPL Exponential Cutoff Power Law.

EGB Extragalactic γ -ray Background.

FoV Field of View.

GPS Galactic Plane Survey.

GRB γ -ray Burst.

GZK Greisen-Zatsepin-Kuzmin.

H.E.S.S. High Energy Stereoscopic System.

HAWC High-Altitude Water Cherenkov Observatory.

HGPS H.E.S.S. Galactic Plane survey.

IACT Imaging Atmospheric Cherenkov Telescope.

IGMFs Intergalactic Magnetic Fields.

IMFs Interstellar Magnetic Fields.

INTEGRAL INTernational Gamma-Ray Astrophysics Laboratory.

IR InfraRed.

IRFs Instrument Response Functions.

KASCADE-Grande KARlsruhe Shower Core and Array DETector Grande.

KSP Key Science Project.

LAT Large Area Telescope on board *Fermi*.

LST Large Size Telescope.

MAGIC Major Atmospheric Gamma Imaging Cherenkov Telescopes.

MC Molecular Cloud.

MCMC Markov chain Monte Carlo.

MST Medium Size Telescope.

PAMELA Payload for Antimatter Matter Exploration and Light-nuclei Astrophysics.

PI Pion decay.

PSF Point Spread Function.

PWN Pulsar Wind Nebula.

SED Spectral Energy Distribution.

SNR Supernova Remnant.

SSC Synchrotron self-Compton radiation.

SST Small Size Telescope.

UV UltraViolet.

VERITAS Very Energetic Radiation Imaging Telescope Array System.

VHE Very high energy, 30 GeV to 300 TeV.

Chapter 1

Gamma-ray Astronomy

The acceleration and propagation of cosmic-rays (CRs) play an important role in understanding astrophysical objects and the universe. The interaction between CRs and the medium (particles, magnetic fields, photon fields) can produce electromagnetic (EM) radiation, which can be used as tracer of CR acceleration and propagation. γ -rays have the highest energy among the EM spectrum, which makes them the best candidates to study particle acceleration. In this chapter, we introduce some basic aspects about CR physics and γ -ray astronomy, including the acceleration and propagation of CRs and radiation, main results of CR observations and high-energy γ -ray observations.

1.1 CR Observations

Several ground-based (e.g. KASCADE-Grande,¹ Pierre Auger Observatory²) and satellite-based CR experiments (e.g. PAMELA, AMS-02³) have obtained important results. Below the knee, satellite-based experiments observe CR with lower energy than ground-based CR experiments. This is due to the fact that satellite-based CR experiments have small geometrical acceptance and need higher flux. The main reviews used for this section are Ref. [17, 70, 85].

Fig. 1.1 shows the CR spectrum of all particles from different experiments [85]. A broken power law (E^{-s}) can describe such a spectrum. Below the knee (4×10^{15} eV), the index is $s = 2.7$. Between the knee and the ankle (10^{18} eV), it is softened, with $s = 3$. The different values of the index in these two regions illustrate that the transition from Galactic to extragalactic CRs, is 10^{15} eV to 10^{18} eV. However, we do not know whether Galactic CRs can reach energies only around the knee or can even reach up to the ankle. In the end of the spectrum, a flux suppression is observed [4, 1]. For the moment, it is not clear if the suppression is due to propagation effect (Greisen-Zatsepin-Kuzmin, GZK for protons) or due to maximum acceleration power of CR

¹<https://web.iqp.kit.edu/KASCADE/>

²<https://www.auger.org/>

³<http://www.ams02.org/>

sources. CRs with large Lorentz factors suffer photo-production of pairs and pions by interacting with the Cosmic Microwave background (CMB). Such an effect results in a cut-off above a few 10^{19} eV, which is called the GZK cut-off [69, 118].

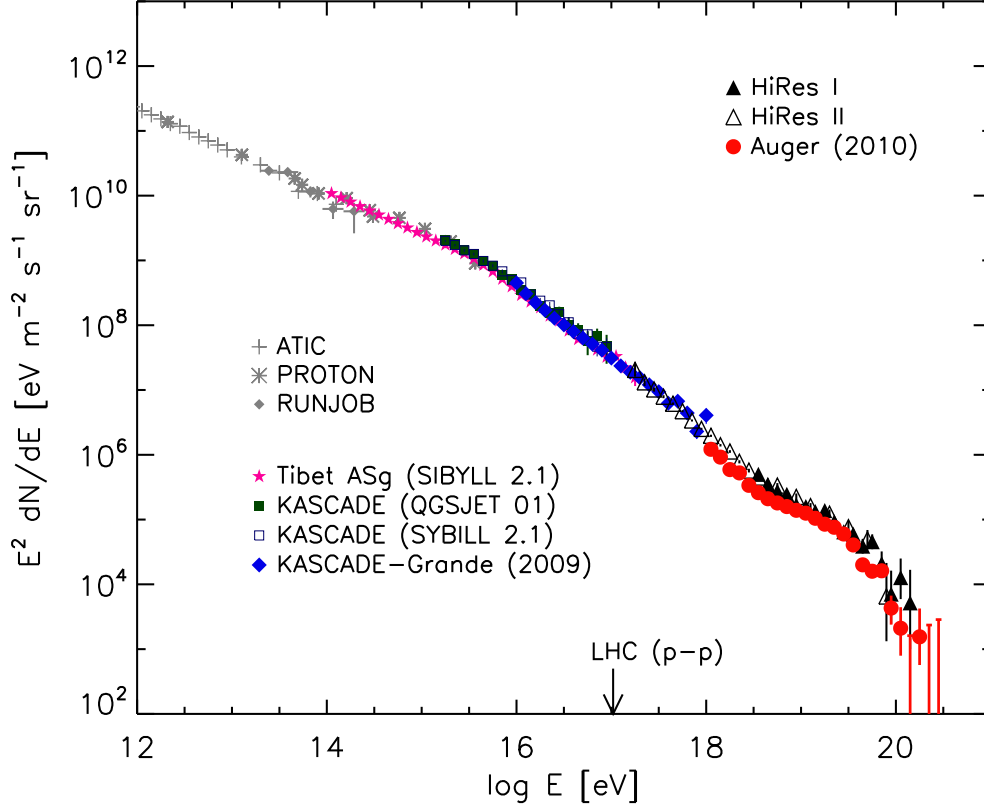


Figure 1.1: All particle spectrum multiplied by E^2 [85]

The origin of the knee has also remained a puzzle. A possible explanation is the acceleration limit of the Galactic CR sources [14, 104]. Following the proposal, we can ask several questions. What is the origin of CRs with energy up to the knee? How astrophysical objects accelerate particles? Why is the CR spectrum close to a power law?

1.2 Acceleration of CRs

Several kinds of astrophysical objects can accelerate particles above GeV energies, such as SNRs, Pulsar Wind Nebulae (PWNs), pulsar, Globular Clusters, Massive Star Clusters, Active Galactic Nuclei (AGNs), γ -ray Bursts (GRBs), Starburst Galaxies [22] and Clusters of Galaxies [25]. The most energetic particle acceleration occurs in relativistic outflows [21]. Diffusive Shock Acceleration (DSA) is a primary mechanism in which particles get to non-thermal energies in shock waves. For example, when SNR ejecta interact with the interstellar medium (ISM), the particles can be accelerated up to PeV energies by shocks [26].

In 1949, Enrico Fermi first gave the principle of transfer of energy [62, 90]. We call it second-order Fermi acceleration. The average energy gain per collision in each acceleration mechanism is:

$$\left\langle \frac{\Delta E}{E} \right\rangle = \frac{8}{3} \left(\frac{v}{c} \right)^2, \quad (1.1)$$

where v is the velocity of ‘magnetic mirrors’. Second-order Fermi acceleration mainly happens in environments modeled as moving magnetized gas clouds.

Later, first-order Fermi acceleration was found to be more efficient than second-order Fermi acceleration. This type of acceleration can occur for simply in SNR shocks. The average energy gain per collision is:

$$\left\langle \frac{\Delta E}{E} \right\rangle = \frac{2}{3} \frac{v}{c}. \quad (1.2)$$

The spectrum of first-order Fermi acceleration (in shocks) is given by:

$$\frac{dN(\epsilon)}{d\epsilon} \propto \epsilon^{-s}, \quad (1.3)$$

where the spectral index $s \geq 2$. First-order Fermi acceleration mainly happens in shocks while second order acceleration mainly in turbulent media [16]. The spectral index of first-order Fermi acceleration is consistent with the observations, which make this acceleration process attractive over years.

Based on the Fermi acceleration theory of DSA mentioned above, we believe SNRs can accelerate CRs up to 1 PeV [100, 113]. Furthermore, by considering only 10% of supernova kinetic energy, one can maintain the population of Galactic CRs up to the knee. Therefore, SNRs appear to be one of the best candidate sources of Galactic CRs [11].

1.3 Propagation of Radiation

Several interaction can affect the propagation of high-energy CRs and γ -rays. CRs can produce γ -rays from pion-decay (PI) induced by proton-proton interaction: $pp \rightarrow pp + \pi^0 \rightarrow pp + 2\gamma$. Besides this, CRs can also produce γ -rays when relativistic electrons transfer energy to low-energy photons. The Klein-Nishina effect is prominent for SNR γ -rays beyond 10 TeV, which means electrons have strong radiative energy losses and the resulting inverse Compton (IC) spectrum shows a cut-off. It is a key process to constrain electron acceleration.

One may wonder whether PeV CRs and the corresponding secondary γ -rays could originate from extragalactic sources. The cosmic γ -ray horizon is determined by interaction of γ -rays photon with the extragalactic background light (EBL). EBL is composed of the light at ultraviolet (UV), optical and infrared (IR) wavelengths which are originated from stars and interstellar dust. It is important for observations of extragalactic objects (e.g. TeV blazars) since pair production dominates the absorption in TeV astronomy. Considering electron-positron production from

interaction between EBL and γ -rays, we can estimate how the γ -rays escape. Fig. 1.2 shows the mean free path (MFP) λ of electron-positron pair production of different energies [112]. Above 10^{14} eV, the MFP decreases steeply down to 10^{-2} Mpc. Since the Galactic radius is about 15 kpc, it is difficult to observe γ -rays above 10^{14} eV. After the minimum, MFP increases and could encompass the Milky Way and the Local Group of galaxies. The attenuation length being of about 4.5 Mpc above EeV (10^{18} eV) energies.

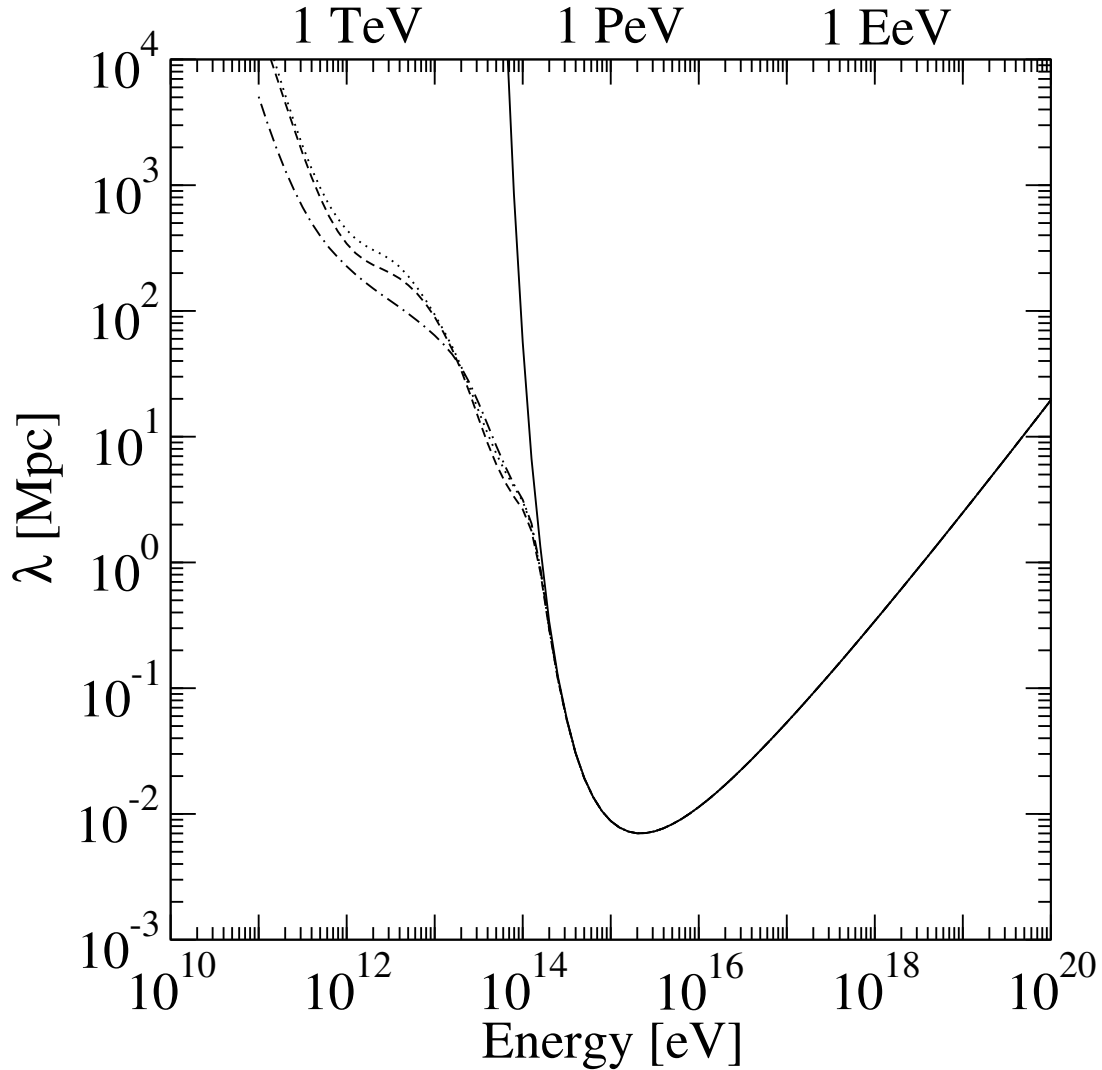


Figure 1.2: Pair production mean free path for γ -ray propagation [112]. Solid line: photon background consisting of the CMB radiation. Dashed and dotted lines: EBL radiation for different models.

1.4 Gamma-ray Astronomy

Very-high-energy (30 GeV to 300 TeV, VHE) γ -rays are key objects for understanding the origin of CRs and the physics of relativistic outflows. CRs are deflected by interstellar magnetic fields

(IMFs) and intergalactic magnetic fields (IGMFs), which makes it difficult to locate the position of the CR sources. Therefore, γ -rays produced by CRs are necessary for searching the origin of CRs. The main reviews of ground-based γ -ray astronomy are Ref. [54, 87], space-based γ -ray astronomy are Ref. [19, 99], and Ref. [67] cover both topics.

Observations from space-based (e.g. *Fermi*-LAT) and ground-based (e.g. H.E.S.S., MAGIC, VERITAS) γ -ray telescopes have accumulated lots of results at GeV and TeV energies. In the GeV band, pulsars and blazars are the major populations of Galactic and extragalactic sources, respectively. However, above TeV energies, SNRs and PWNe are the major populations in our Galaxy. Blazar is the major population for extragalactic TeV objects.⁴

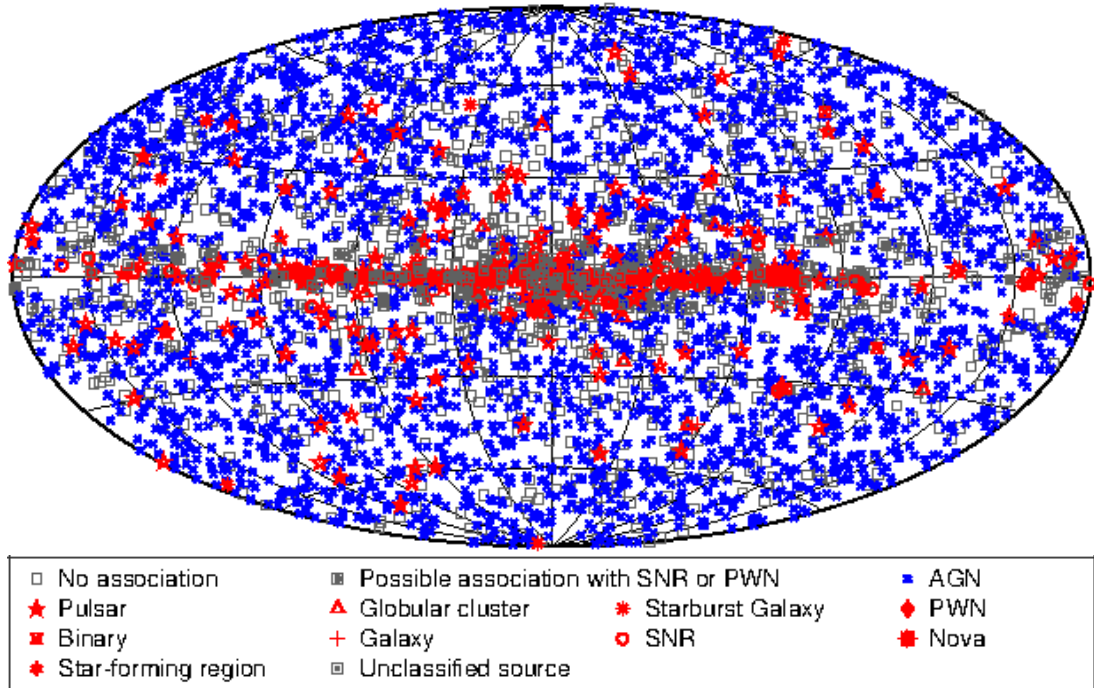


Figure 1.3: The fourth *Fermi*-LAT source catalog full sky map in Galactic coordinates [48].

Fig. 1.3 shows a skymap of a preliminary version of the fourth *Fermi*-LAT source catalog (4FGL) based on eight years of data [48]. There are 5098 sources above 4σ significance between 0.05 GeV and 1 TeV. There are 3131 blazars in the 4FGL, which is the largest population, 1323 unassociated sources, 38 radio galaxies, 241 pulsars, 40 SNRs, 18 PWNe, 30 globular clusters, and the others (are mainly unknown sources⁵).

⁴<http://tevcat.uchicago.edu/>

⁵sources associated to counterparts of unknown nature

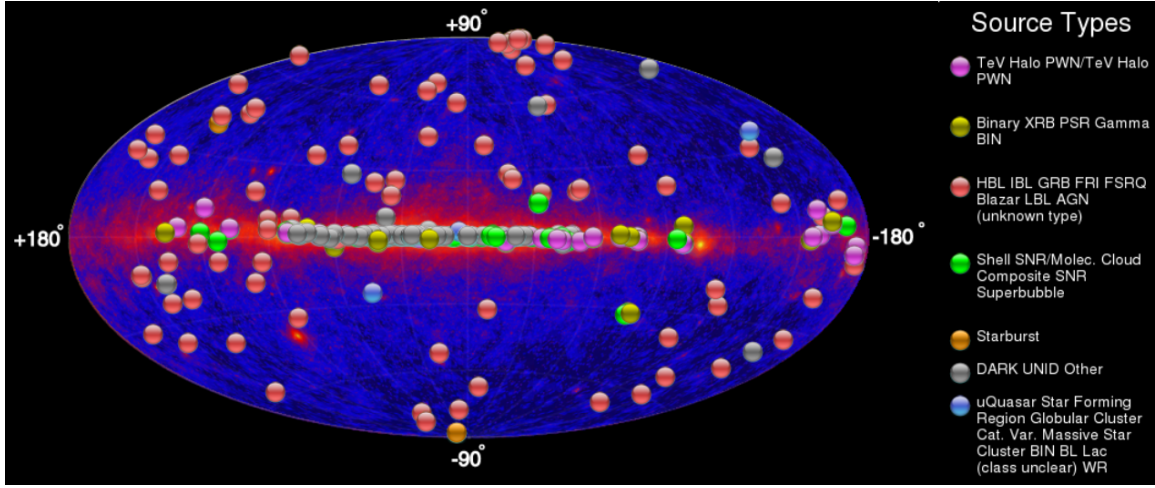


Figure 1.4: TeVCat full sky map (May 2019) in Galactic coordinates from TeVCat.

Fig. 1.4 shows the skymap of γ -ray sources with energy above 1 TeV. There are 28 SNRs, 36 PWNe, and 75 AGNs. For comparison, blazars are still the dominant population for extragalactic sources. However, pulsars are not the dominant population for Galactic TeV sources.

The H.E.S.S. Galactic Plane survey (HGPS) maps sources at TeV energies [76]. With ten years of observations, HGPS observations amount to nearly 2700 h of selected data, which covers the Galactic plane at longitudes from 250° to 65° and latitudes less than 3° . It contains 78 VHE sources. Fig. 1.5 illustrates the HGPS region and compares this region to the structure of the Galaxy, including the all-sky *Planck* CO(1-0)⁶ map and the regions of other surveys performed by different ground-based γ -ray telescopes. Since the *Planck* CO(1-0) map is a good tracer of matter density profile, it was used as reference in HGPS.

Considering the major γ -ray populations and our research topic, we introduce AGNs, SNRs, pulsars, and diffuse emissions in the following subsections, including their basic characteristics.

⁶The rotational emission line $J = 1 \rightarrow 0$ of CO excited by collisions with H_2 makes it a good tracer to discover molecular clouds (MC).

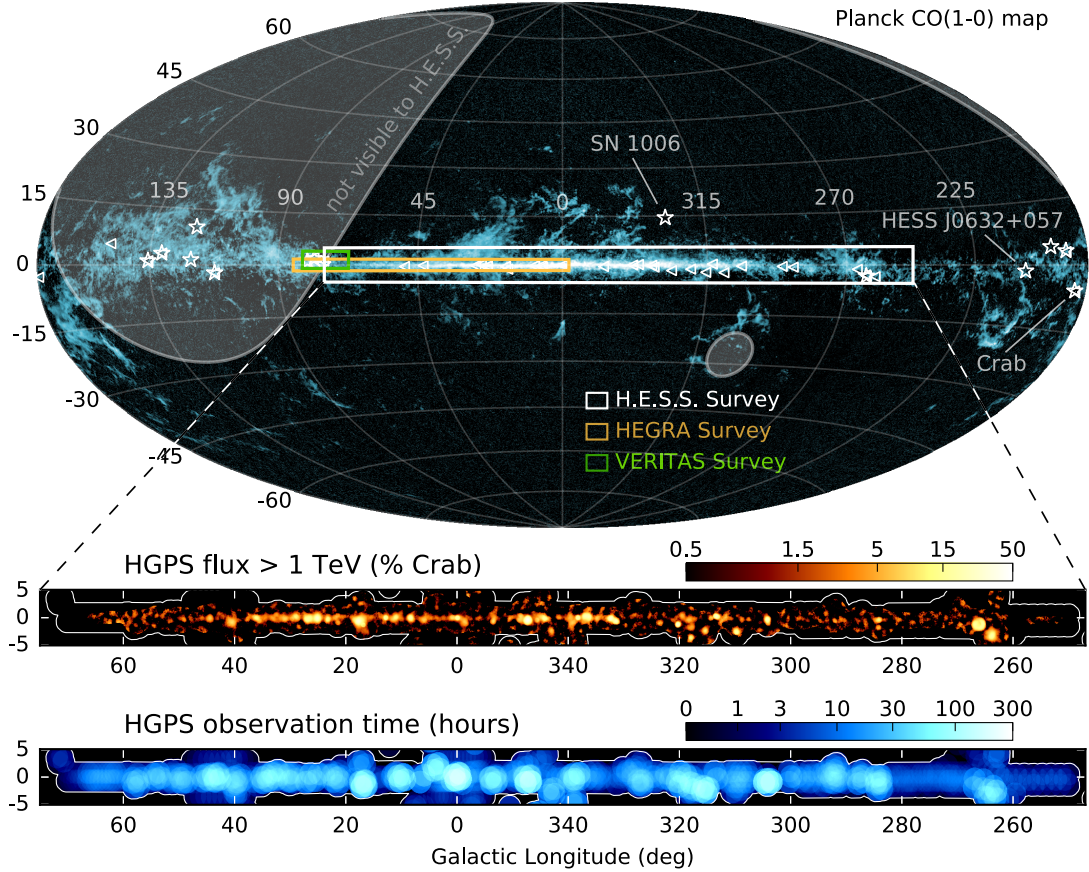


Figure 1.5: Illustration of H.E.S.S. Galactic plane survey region superimposed on an all-sky image of *Planck* CO(1-0) data in Galactic coordinates. Triangles denote the Second Catalog of Hard *Fermi*-LAT Sources (2FHL) γ -ray sources identified as Galactic, and stars indicate the 15 Galactic VHE γ -ray sources outside the HGPS region [76].

1.4.1 Gamma-ray AGN

The fourth *Fermi*-LAT catalog of Active Galactic Nuclei includes 2863 AGNs located at Galactic latitudes higher than 10° and 345 AGNs at low Galactic latitudes [49]. 98% of these AGNs are blazars (a sub-class of AGNs with jets that point towards the observers), with radio-loudness, variability, and polarization. Blazars have broad wavelength non-thermal continuum emission with short timescale variability, which are illustrated in the second catalog of flaring γ -ray sources (2FAV) from the *Fermi* all-sky variability analysis [31].

Most TeV AGNs can be described with a power-law of spectral index at GeV energies harder than 2.0. Detection of TeV blazars constrain EBL [15, 55, 5] and IGMF strength [64, 95]. Similarly to AGNs at GeV energies, most TeV AGNs are blazars. MWL observations of TeV blazars reveal two non-thermal components: one at lower energies peaking between the UV and the X-ray regime, and a second peaking in the γ -ray regime. The low-energy component is commonly interpreted as synchrotron radiation from relativistic electrons, while the high-energy component results from IC scattering of lower energy photons in the region of the jet, or from

hadronic processes, such as pion decay produced in interactions of relativistic protons or proton synchrotron.

1.4.2 Gamma-ray Supernova Remnants

Based on the spatial overlap of γ -ray sources with SNRs known from radio catalogs, the *Fermi*-LAT collaboration classified 30 GeV SNRs.

Fig. 1.6 shows the power-law index of the TeV detected sources at GeV and TeV energies [47]. The purpose for this figure is to illustrate how the index changes from GeV to TeV energies. The line, which represents the equal value for GeV and TeV index, reveals spectral curvature in the parent distribution of electrons and protons. 6 SNRs have softer TeV indices compared to their GeV indices at a confidence level beyond 1σ . Considering the systematic and statistical errors, 3 SNRs have GeV and TeV indices are consistent to each other at the 1σ level. 1 SNR has a somewhat harder TeV index compared to its GeV index, which would suggest that the radiative process on particle population changes between GeV and TeV energies if the difference is significant.

From Fig. 1.6 one also finds that the three non-thermal X-ray SNRs (blue circles) have lower photon indices than the seven SNRs interacting with MC (red circles). It is possibly explained by the evolution in index with SNR age.

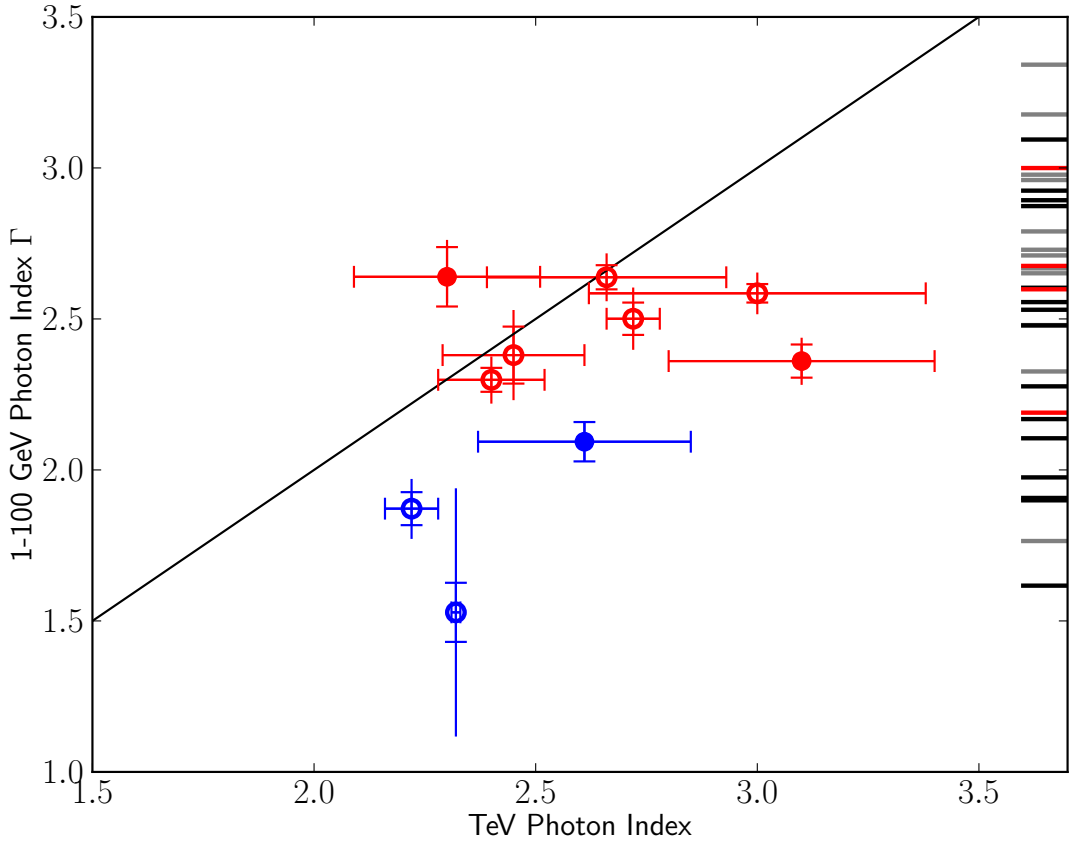


Figure 1.6: 1 – 100 GeV photon index compared to TeV photon index measurements. The line represents the equal value for GeV and TeV index. Open circles and filled circles are extended SNRs and point-like sources, respectively. Blue and red are non-thermal X-ray SNRs and SNRs interacting with MC, respectively. The ticks along right side represent the GeV candidates with indices in the range of those with a TeV counterpart but with no TeV measurements themselves, which demonstrate the limitations of the data set [47].

The HGPS constrains typical ambient density values around shell-type SNRs to $n \leq 7 \text{ cm}^{-3}$ [48]. Comparisons of VHE with radio data in non-interacting SNRs reveal activities that are in agreement with the theory of magnetic field amplification at shell-type SNRs [72].

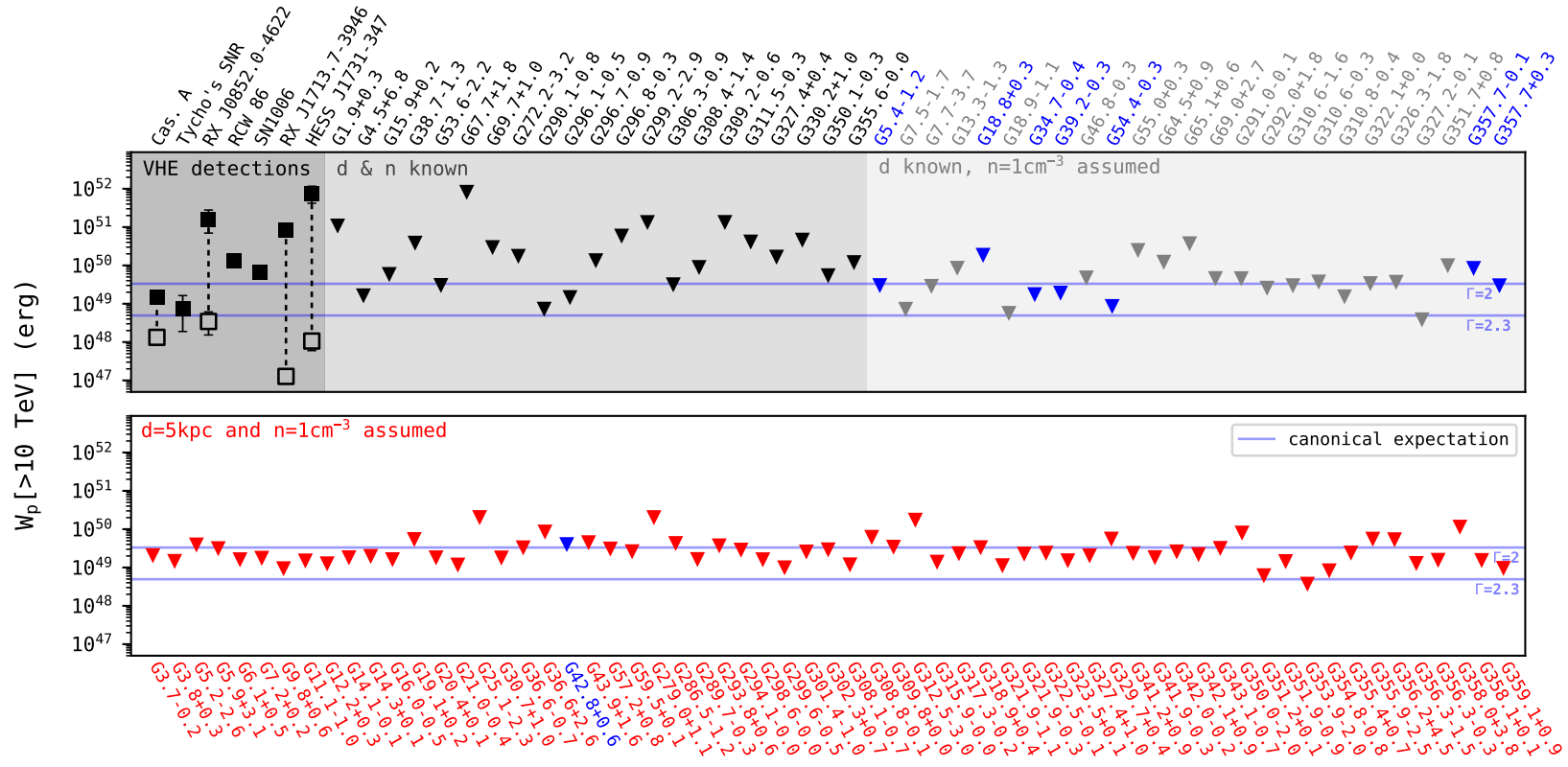


Figure 1.7: Upper limit of proton energy content above 10 TeV (triangles). Blue triangles indicate SNRs that are likely to interact with molecular clouds [72].

Fig. 1.7 shows the proton content of Galactic SNRs at VHE from HGPS. It gives upper limits (UL) on the total energy of protons above 10 TeV for all objects that have been investigated, assuming the ambient density of ISM as $n = 1 \text{ cm}^{-3}$ and a typical source distance of $d = 5 \text{ kpc}$, when this information is not available. From fig. 1.7, one can use it to get the power of proton acceleration.

1.4.3 Gamma-ray Pulsars

The second *Fermi*-LAT catalog of γ -ray pulsars identifies 117 pulsars above 1 GeV. Half of them are discovered by using *Fermi*-LAT data through periodicity searches in γ -ray and radio data [3]. They can be mainly divided into three groups: 40 millisecond pulsars (MSPs), 42 young radio-loud pulsars, and 35 young radio-quiet pulsars.

The high-energy emission of pulsars are produced by IC or by curvature radiation. Such radiation originates from electron and positron in pulsar magnetosphere. The outer gap model is one of the promising explanations for pulsar γ -ray emission which suggests particles are accelerated in outer magnetosphere, although other acceleration region have been proposed, such as polar cap and slot gap [29].

1.4.4 Diffuse Gamma-ray Emissions

The γ -ray sky is full of Galactic and extragalactic diffuse emission.

The GeV γ -ray sky is dominated by the Galactic diffuse emissions from interaction of CRs with ISM and Galactic photon fields. Such diffuse emissions are the main difficulties in identifying point sources from 10 GeV to 100 GeV. The γ -ray flux above 1 TeV from the Galactic Plane is detected by H.E.S.S. [39]. It can be explained as diffuse Galactic γ -ray emissions and contribution from unresolved sources. Such emissions are comprised of γ -rays from both pion decay and IC. As energies be higher and higher (above 1 TeV), the γ -ray flux from resolved sources dominates the observed γ -ray radiation.

The extragalactic γ -ray background (EGB) mainly originates from AGNs and star-forming galaxies [30]. The intensity of EGB can help us to constrain several physical problems (e.g. dark matter annihilation [89]). The main challenges for EGB measurement is the modelling of diffuse Galactic emission (DGE) since DGE has considerable intensity compared to EGB above 1 GeV.

1.5 CTA Science

Cherenkov Telescope Array, as the next-generation ground-based γ -ray observatory covering the energy range from 20 GeV to 300 TeV, aims to answer three fundamental questions [51]:

- Understanding the origin and role of relativistic cosmic particles;

- What are the sites of high-energy particle acceleration in the universe?
- What are the mechanisms for cosmic particle acceleration?
- What role do accelerated particles play in feedback on star formation and galaxy evolution?
- Probing extreme environments;
 - What physical processes are at work close to neutron stars and black holes?
 - What are the characteristics of relativistic jets, winds and explosions?
 - How intense are radiation fields and magnetic fields in cosmic voids, and how do these evolve over cosmic time?
- Exploring frontiers in physics.
 - What is the nature of dark matter? How is it distributed?
 - Are there quantum gravitational effects on photon propagation?
 - Do axion-like particles exist?

Compared to current IACTs, with a huger energy range, wider field of view (FoV) and better sensitivity (see next chapter), CTA can find much more sources. The angular resolution can enable the detailed imaging of γ -ray sources.⁷ The big collection area makes it possible to detect more photons. All these performances help to answer the scientific questions above. Based on the aims, the CTA Consortium proposed Key Science Projects (KSPs) for future operation. There are nine KSPs for CTA [51]:

- Galactic Centre;
- Galactic Plane Survey;
- LMC Survey;
- Extragalactic Survey;
- Transients;
- Cosmic-ray PeVatrons;
- Star Forming Systems;
- Active Galactic Nuclei;
- Clusters of Galaxies.

⁷The comparison between CTA and current IACTs on sensitivity and angular resolution is shown in next chapter.

This thesis work mainly involves the Galactic Plane Survey and Cosmic-ray PeVatron KSP. Therefore, we introduce these two topics in the following.

The Galactic Plane Survey (GPS) program of CTA will significantly increase the number of VHE γ -ray sources. The combination of the FoV of CTA with sensitivity makes it possible to get one to two orders of magnitude improvements of the coverage with expect to current IACTs (see next chapter). Such a survey will help us to understand the Galactic source populations and the Galactic diffuse emission. It consists of a deep survey (~ 2 mCrab)⁸ of the inner Galaxy and the Cygnus region, providing access to distances up to ~ 20 kpc. In addition, the short-timescale capabilities of CTA allow the identification of variable objects (e.g. γ -ray binaries). Thanks for real-time alerts from CTA, GPS observations can result in a considerable number of short time transients.

PeVatron candidates are key targets of GPS, with SNRs the most promising candidates. If SNRs are sources of CRs, they should also show secondary VHE γ -ray emission. With magnetic field amplification, SNR shocks can accelerate CR protons to a few PeV. As PeV protons produce 100 TeV photons, CTA will be a powerful facility to detect PeVatrons. Since CTA has tremendous sensitivity up to hundreds of TeV, it will have a prominent place to identify PeVatrons. Although current Extensive Air Shower (EAS) detector (e.g. HAWC [38]) have a good sensitivity at around 100 TeV, they have worse energy and angular resolution [37].

1.6 A Brief Summary

The origin of the CR knee at around PeV is still an open question. Based on the theoretical prediction of particle acceleration in SNRs as well as to their global energy budget, they are presented as the probable sources of Galactic CRs [98]. Therefore, searching PeVatron candidates among SNRs helps us to understand the nature of the CR knee. CRs can produce high-energy γ -rays via pion production and component decay to two photons. By detecting these γ -rays, we can learn about the physical processes of photon productions (introduced in chapter 4). The corresponding radiative models will be introduced on Chapter 4. Since SNRs are one of the major population of Galactic sources at TeV energies, they are also good candidates to study Galactic CR by doing MWL analysis. The future CTA with its capabilities (sensitivity, FoV), is expected to detect new SNRs. Both individual study and population synthesis based on future CTA results are helpful to constrain their physical parameters of SNRs. The CTA KSP includes various scientific programs for the study of SNRs (GPS, CR PeVatron). With the sensitivity of CTA, the GPS provides a deep survey which can uncover a huge amount of Galactic sources. Therefore, CTA will offer great opportunities to search for PeVatrons.

⁸1 Crab is defined as the intensity of the Crab Nebula at the corresponding γ -rays energy.

Chapter 2

Extensive Air Showers and Experimental Technique

When a γ -ray goes through the Earth atmosphere, it interacts with the medium and generates extensive air showers (EAS) and Cherenkov light. Such mechanism makes it possible to observe high-energy and very-high-energy γ -rays on the ground by detecting their secondary products. In this chapter, we will give the basic concept of EAS and Cherenkov light emission, the technique of Imaging Atmospheric Cherenkov Telescopes (IACT), and discuss the performances of current IACT instruments and CTA.

2.1 Gamma-ray Detectors

2.1.1 Space-based Gamma-ray Detectors

The cross section is a key indicator for deciding which kind of interaction should be used in X-ray and γ -ray detection. Compton scattering has a larger cross section than pair production between 300 keV and 30 MeV. Therefore, γ -ray telescopes with detection energy in this range (e.g. INTEGRAL [114]) are based on Compton scattering. For photons with energy above a few MeV, pair production is the dominant process as a result of a larger cross section. Since $m_e = 0.511 \text{ MeV}/c^2$, the minimum energy required for pair production to occur is around 1 MeV. Therefore, space-based detectors (e.g. *Fermi*-LAT, AGILE [20]) above 30 MeV operate on the principle of pair-creation in the detector.

The *Fermi*-LAT consists of a tracker to measure the tracks of the electron-positron pairs, an electromagnetic calorimeter to determine the energy of this electron-positron pair, and an anti-coincidence detector to veto the charged particle background. The small effective area (the area times the detection efficiency) of space-based detectors results in the limitation of sensitivity. The good rejection ability to CRs of space-based detectors results in a low rate of background events. Although pair-production space-based telescopes dominate the observations

at low energies, it is difficult for them to detect many γ -rays above 100 GeV due to rapidly decreasing flux of γ -rays with the increase of energy. They would need larger effective areas, which increase the costs of the telescope.

2.1.2 Ground-based Gamma-ray Detectors

Thanks to the Earth's atmosphere, we have another way to observe this electromagnetic radiation window. GeV to TeV γ -rays interacting with the Earth's atmosphere initiate electromagnetic cascades yielding Cherenkov light and also a large number of particles (e^- , e^+ , etc). Compared to space-based detectors, ground-based detectors have a huge effective area (see table 2.1), so their sensitivity is high. Results from both γ -rays and charged particles, air showers are extensive cascades including electrons, positrons, protons, muons, etc. At the same time, Cherenkov photons are produced from the propagation of these secondary particles in the atmosphere.

2.1.2.1 Electromagnetic Cascades

Heitler proposed a simple model of EM cascades, modeling the effects of pair production and bremsstrahlung in the EM field of atoms and nuclei [73]:

- A parent particle splits into two particles in each interaction. Each particle gets half of the energy.
- The cascade consists of $N(X) = 2^{X/\lambda}$ particles, where X is the shower depth, and λ is the interaction length.
- Each particle has an energy $E(X) = E_0/N$, where E_0 is the energy of the primary particle.
- Below 0.1 GeV, ionization is the dominant process. As a result, particle production stops when $E(X) < 0.1$ GeV.

Fig. 2.1 illustrates the schematic views of EM and proton cascades based on Heitler model [93]. The left panel illustrates the processes of electron-positron pairs production and bremsstrahlung created by electrons and positrons. This process will stop when ionization dominates. The right panel shows the hadronic shower induced by interaction between protons and atmosphere. This interaction yields that π^\pm and π^0 emerge from the collision. The produced π^0 decay to γ -ray immediately. For γ -ray detection, hadronic showers are important background, which must be separated from the photon showers.

2.1.2.2 Cherenkov Radiation

The relativistic particles in air showers have faster speed than light in air, which produce Cherenkov radiation. The angle θ between the particle track and the Cherenkov emission

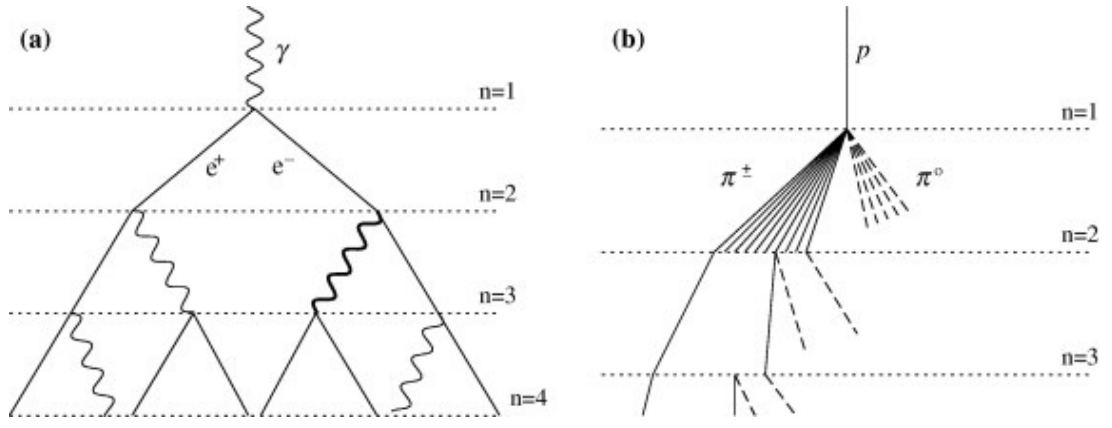


Figure 2.1: (a): schematic view of an EM cascade. (b): schematic view of a hadronic shower. Dotted lines indicate the steps of interaction. Wavy lines indicate photons produced from bremsstrahlung [93].

direction is given by:

$$\cos \theta = \frac{c'}{v} = \frac{1}{\beta n}, \quad (2.1)$$

where the velocity of light $c' = c/n$, velocity of the particle $v = \beta c$, and n is the refractive index. Only when $\beta \geq 1/n$ can the Cherenkov emission take place. The corresponding minimal energy of the particles is:

$$E_{\min} = \frac{mc^2}{\sqrt{1 - \beta^2}}. \quad (2.2)$$

The density of the Earth atmosphere is not a constant, which results in the refractive index depending on the atmospheric altitude h (that is $n = n(h)$).

Fig. 2.2 shows longitudinal views of simulated EAS initiated by a photon (left) and a proton (right).¹ Comparing the photon and proton components, the photon shower image is more compressed while the proton shower image is more sparse. This can help us to separate the photon and proton components.

Fig. 2.3 shows the simulated Cherenkov light on the ground for showers from 300 GeV photons and 1 TeV protons.² The different lateral structures induced from photons and protons (see fig. 2.2) result in different images on the camera of IACTs.

There are two main classes of ground based VHE γ -ray detectors: the EAS arrays and the Cherenkov telescopes. Fig. 2.4 illustrates the technique of two ground-based γ -rays detectors [91]. The left figure shows sampling of EAS detected by ground-based arrays while the right shows the detection of Cherenkov light. Ground-based IACTs are used for detecting γ -rays around 1 TeV and EAS detectors are used for detecting γ -rays around 100 TeV.

¹<https://www.ikp.kit.edu/corsika/>

²The EAS initiated by 300 GeV photons and 1 TeV protons have similar amount of Cherenkov radiation. Therefore, we used different energy for them.

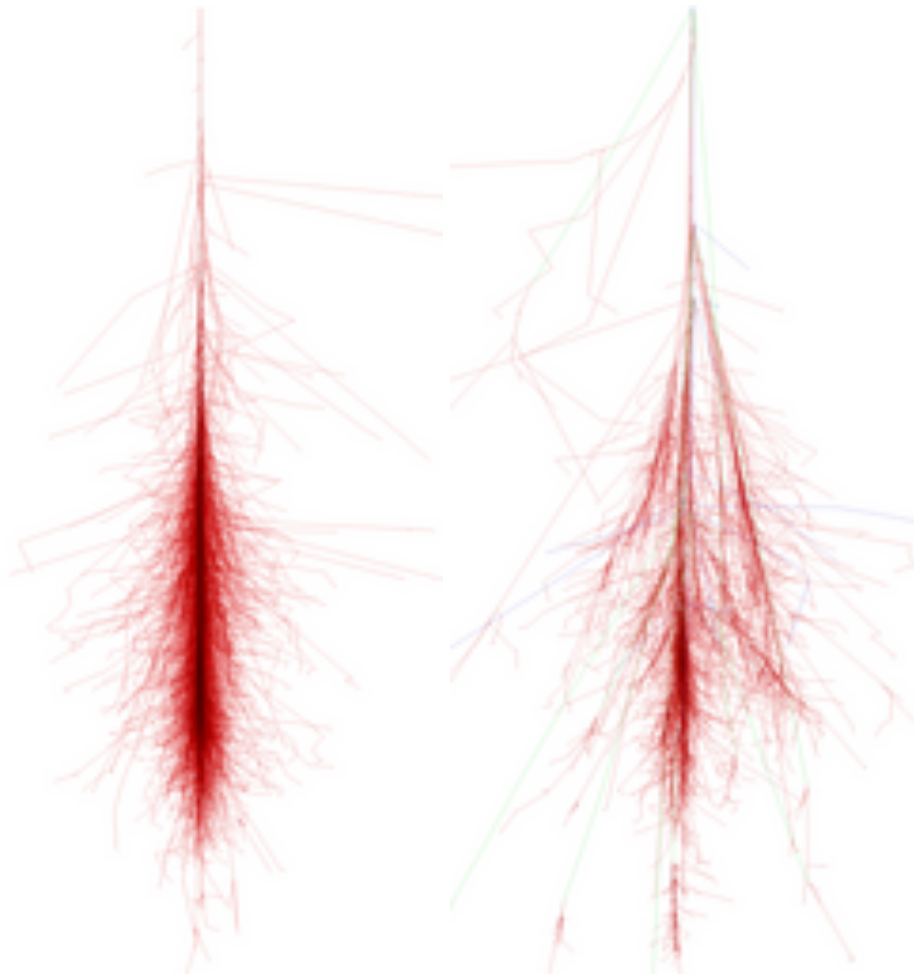


Figure 2.2: Air shower of different component. Left: photon shower. Right: proton shower. They are compiled by Fabian Schmidt from University of Leeds.

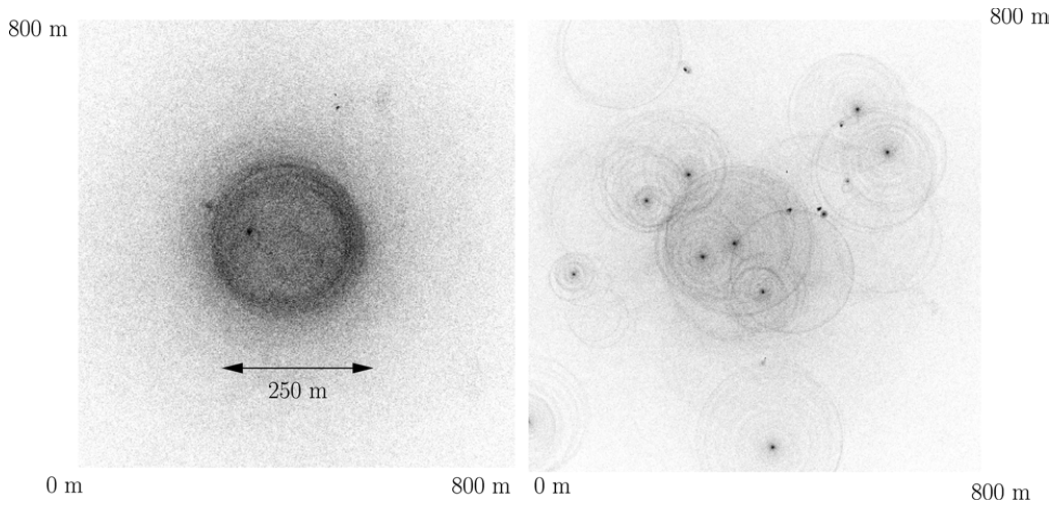


Figure 2.3: The Monte Carlo simulation results of photon and proton shower. Left: 300 GeV γ -ray showers. Right: 1 TeV proton showers [56].

The EAS detectors (e.g. MILAGRO [2], HAWC), also mentioned as Water Cherenkov detectors, are large arrays of detectors sensitive to charged secondary particles generated in EASs. They have a high duty cycle ($> 90\%$) and a large field-of-view (FoV) ($4\pi/6$), but a relatively low sensitivity (0.5 Crab at 5 TeV) (see the values on table 2.1). Different kinds of detectors: arrays of scintillator detectors, Resistive-Plate Chambers (RPC), or water Cherenkov pools can achieve the detection. The energy threshold of EAS detectors is at best of 1 TeV. At such energies, fluxes are smaller and larger surfaces of order of 10^4 m^2 are required.

The IACTs (e.g. H.E.S.S., MAGIC, VERITAS) image the Cherenkov light produced by the cascade of relativistic charged particles in short time scales ($3 \sim 5 \text{ ns}$). Each telescope comprises a segmented mirror which reflects the Cherenkov light onto an array of photomultiplier tubes (PMT).

The EAS detectors and the IACTs have complementary capabilities that allow for a deeper study of the γ -ray sky at TeV energies. Due to a combination of higher energy threshold and larger angular resolution, the EAS detectors are typically less sensitive to point sources than IACTs. However, they can continuously monitor the entire sky above the detector.

It is necessary to compare the performance of different kinds of instruments to establish the observation strategy for different science cases. Table 2.1 gives the different performances of a space-based telescope (*Fermi-LAT*), IACTs and EAS arrays. We can see that IACTs have three main advantages: the huge detection area of showers, the separation of γ -rays and hadrons and the accuracy of reconstruction of shower. However, *Fermi-LAT* has a larger FoV and EAS arrays have a higher duty cycle. This thesis involves CTA, so we introduce more details for IACTs in the following section.

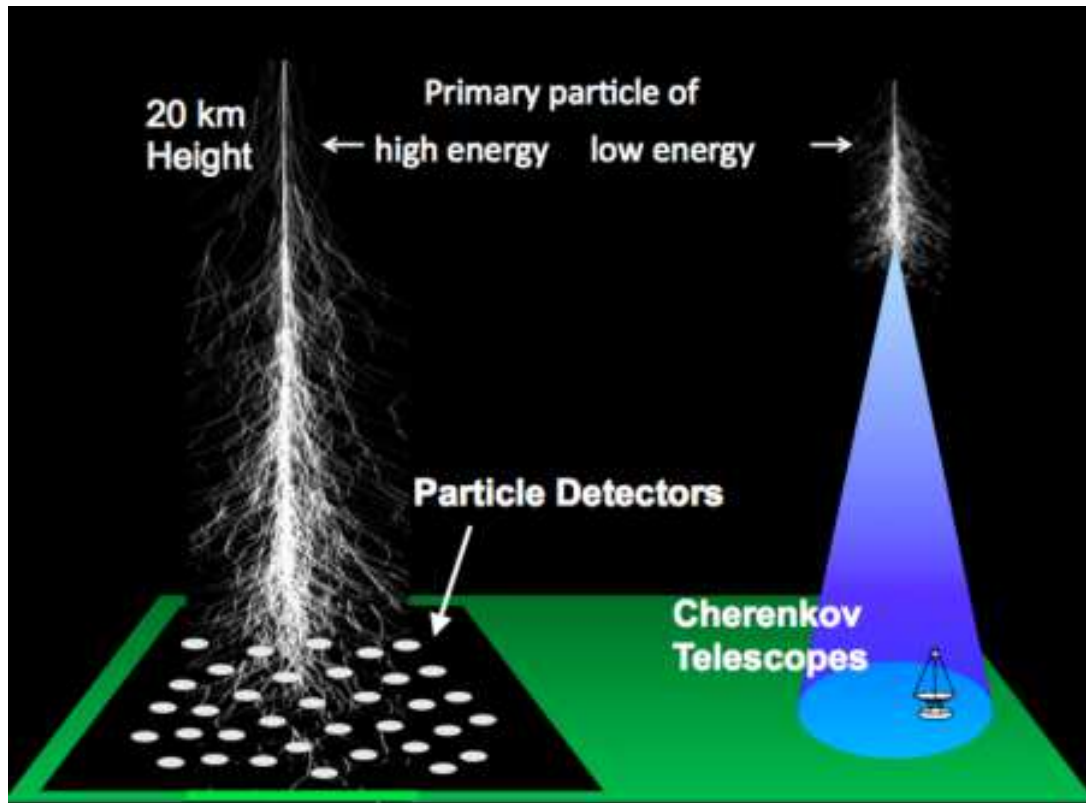


Figure 2.4: Detection of Cherenkov telescopes and EAS detectors [91]

2.1.3 Reconstruction of the Parameters of the Showers for IACTs

The ‘stereo imaging’ technique is based on the simultaneous detection of EAS in different projections by different telescopes. Such a technique provides an accurate reconstruction of shower parameters, in particular the direction of the primary γ -ray, and suppression of background events. Since the Cherenkov images of the same air shower in different projections are only partially correlated, the stereoscopic imaging technique increases the rejection of background hadronic showers, which improves the flux sensitivity.

In order to reconstruct the real photon information (direction, energy) from observed information, Hillas developed the ‘Hillas parameters’ [77]. They include:

- Length of the ellipse;
- Width of the ellipse;
- Distance: the angular distance between the center of the camera and the image center of gravity;
- α : the orientation angle between the major axis of the ellipse and the axis defined by M and C.
- φ : the azimuthal angle of the image main axis.

Quantity	<i>Fermi</i> -LAT	IACTs	EAS
Energy range	20 MeV–200 GeV	100 GeV–50 TeV	400 GeV–100 TeV
Energy res.	5-10%	15-20%	~ 50%
Duty Cycle	80%	15%	> 90%
FoV	$4\pi/5$	$5^\circ \times 5^\circ$	$4\pi/6$
Point Spread Function (PSF)	0.1°	0.07°	0.5°
Sensitivity	1% Crab (1 GeV)	1% Crab (0.5 TeV)	0.5 Crab (5 TeV)

Table 2.1: A comparison of the characteristics of *Fermi*-LAT, the IACTs and of the EAS particle detector arrays. Sensitivity computed over one year for *Fermi*-LAT and the EAS arrays, and over 50 hours for IACTs. Table from Ref. [53]. Explanation can be found in next section.

Fig. 2.5 gives the definition of Hillas parameters, and the scheme of the elliptical image produced by EAS on an IACT. The reconstruction of the γ -ray direction is based on the intersection of the shower image main axes of the ellipse in the camera. The reconstruction of the energy is based on the estimation of a weighted average of the charge deposit in each telescope. The Hillas parameters not only allow to reconstruct the shower parameters, but also can discriminate between γ -rays and CRs. It means that photon-induced showers and hadron-induced showers should have different distributions in these parameters.

The comparison between the real width and length, and their mean value and variance, σ^2 , can be used for background rejection. The normalized parameters Scaled Width (SW) and Scaled Length (SL) are:

$$SW = \frac{w(q, \rho) - \langle w(q, \rho) \rangle}{\sigma_w(q, \rho)}, \quad SL = \frac{l(q, \rho) - \langle l(q, \rho) \rangle}{\sigma_l(q, \rho)} \quad (2.3)$$

where q is the image charge, and ρ is the reconstructed impact distance.

These parameters can be combined in stereoscopic observations in Mean Scaled Width (MSW) and Mean Scaled Length (MSL):

$$MSW = \frac{\sum_{tels} SW}{\sqrt{ntels}}, \quad MSL = \frac{\sum_{tels} SL}{\sqrt{ntels}} \quad (2.4)$$

where $ntels$ is the number of telescopes. Further discussions can be seen in ref. [77]. Hillas parameterization method is used as a tool for reconstruction and background rejection but it is not the only technique (e.g. Model3D technique [88] for background rejection).

2.1.4 Performance of IACTs

Several factors can indicate the performance of IACTs:

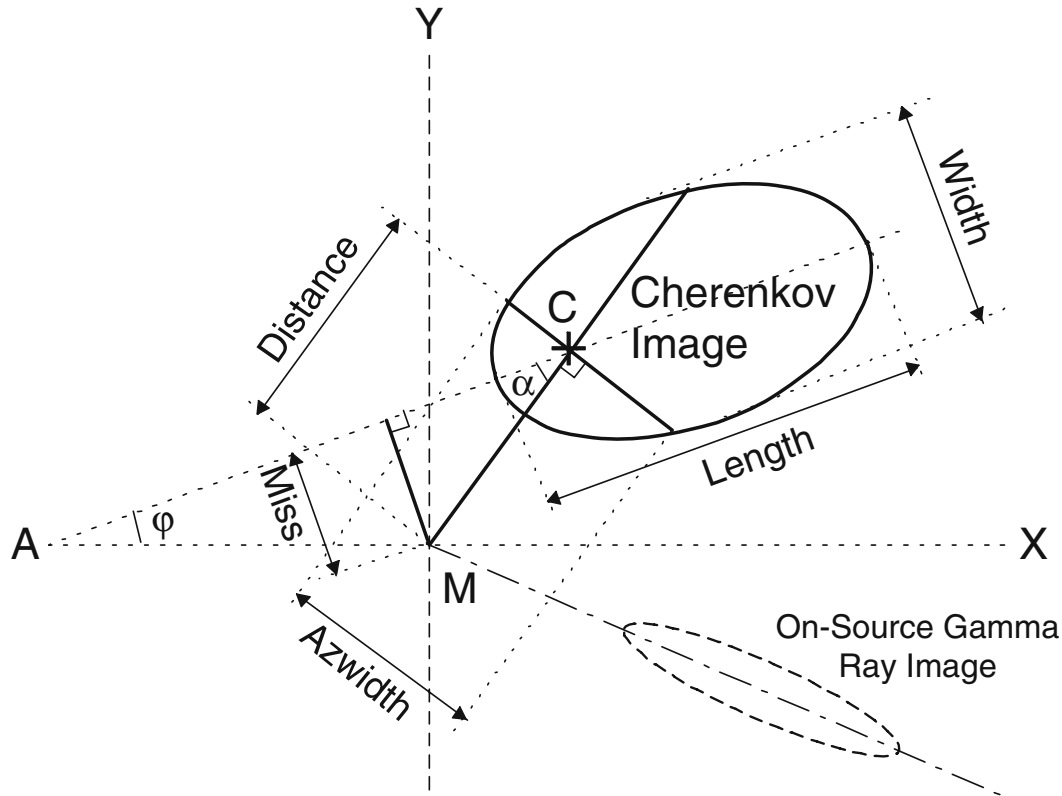


Figure 2.5: Definition of Hillas parameters on the camera [56]. C is the image centre. M is the centre of camera. α is the orientation angle between the major axis of the eclipse and the axis defined by M and C. φ is the angle M and C. (see the text)

- Angular resolution: it represents how ‘small’ the spatial structure of an astrophysical objects we can distinguish, which is important to reduce background and avoid source confusion.
- Energy resolution: it represents the capability for actually reconstructing the spectrum, which is important for spectral features like emission lines.
- Collection area: area over which γ -ray events are obtained
- Background rate: it represents the number of hadronic showers mis-identified as γ -ray like events
- Sensitivity: the capability of an instrument to detect a source with a certain energy flux. This quality depends on the previous factors.

The Instrument Response Functions (IRFs) $R(\vec{d} | \vec{p}, a)$ provide a mathematical description that links the measured quantities, \vec{d} , of an event to the physical properties, \vec{p} , of the incident

photon:

$$e(\vec{d}) = \int d\vec{p} R(\vec{d} | \vec{p}, a) \times I(\vec{p}), \quad (2.5)$$

where $I(\vec{p})$ is the γ -ray intensity arriving at Earth as a function of photon properties \vec{p} (which usually are true photon energy, true photon incident direction, and true photon arrival time), while $e(\vec{d})$ is the expected event rate as function of event properties \vec{d} (which usually are the measured photon energy, measured or reconstructed photon incident direction, and measured photon arrival time). The expected event rate is obtained by integrating the product of the IRFs $R(\vec{d} | \vec{p}, a)$ and the emitted intensity $I(\vec{p})$ over the photon properties \vec{p} .

The IRFs are factorized into the effective area $A_{\text{eff}}(p, E, t)$ (units cm^2), the point spread function $PSF(p' | p, E, t)$, and the energy dispersion $E_{\text{disp}}(E' | p, E, t)$ following:

$$R(p', E', t' | p, E, t) = A_{\text{eff}}(p, E, t) \times PSF(p' | p, E, t) \times E_{\text{disp}}(E' | p, E, t). \quad (2.6)$$

$PSF(p' | p, E, t)$ is the probability distribution function, a 4-dimensional cube spanned by true position, true photon energy, and offset angle between true and reconstructed arrival direction of a photon.

$$PSF(\delta | p, E) = \frac{\sum_i PSF_i(p' | p, E) \times A_{\text{eff},i}(p, E) \times \tau_i}{\sum_i A_{\text{eff},i}(p, E) \times \tau_i}, \quad (2.7)$$

where τ_i is the livetime of observation i .

$E_{\text{disp}}(E' | p, E, t)$ is a 4-dimensional cube spanned by true Right Ascension or Galactic longitude, true Declination or Galactic latitude, true photon energy, and migration which is the ratio between reconstructed and true photon energy.

$$E_{\text{disp}}(E' | p, E) = \frac{\sum_i E_{\text{disp},i}(E' | p, E) \times A_{\text{eff},i}(p, E) \times \tau_i}{\sum_i A_{\text{eff},i}(p, E) \times \tau_i}. \quad (2.8)$$

The background cube is a 3-dimensional cube depending on the reconstructed position and photon energy. It has:

$$B(p', E') = \frac{\sum_i B_i(p', E') \times \tau_i}{\sum_i \tau_i}. \quad (2.9)$$

The exposure cube is a 3-dimensional cube also depending on the reconstructed position and photon energy. It is computed as:

$$X(p, E) = \sum_i A_{\text{eff},i}(p, E) \times \tau_i. \quad (2.10)$$

All equations come from <http://cta.irap.omp.eu/ctools/users/glossary.html>.

2.2 Cherenkov Telescope Array

CTA is the next generation γ -ray observatory, with unrivaled sensitivity from 20 GeV to 300 TeV. Located in both the northern (La Palma, Spain) and southern hemispheres (Paranal, Chile), CTA can run a larger sky coverage survey on both southern and northern hemispheres. It is expected to discover hundreds of TeV γ -ray sources.

2.2.1 Telescopes

Three classes of telescope will be distributed in the northern and southern hemispheres based on their sensitivity: the 4 m Small-Sized Telescope (SST) covered the energy of 5 TeV to 300 TeV, 12 m Medium-Sized Telescope (MST) covered the energy of 150 GeV to 5 TeV, and 23 m Large-Sized Telescope (LST) covered the energy of 20 GeV to 150 GeV. The large mirrors and high-speed cameras of CTA will detect flashes of Cherenkov light and image the cascades generated by γ -rays from cosmic sources. These cascades are rare. Therefore, CTA will be using more than 100 telescopes in the northern and southern hemispheres to improve the detection capabilities.

While the northern array will be more limited in size and will focus on the range from 20 GeV to 20 TeV, the southern array will span the entire energy range of CTA, covering γ -ray energies from 20 GeV to 300 TeV. Since the SST sub-array are tuned to be the most sensitive to detect high-energy γ -rays, they are more suitable for the southern site where a huge fraction of observations will be dedicated to Galactic sources. Because γ -rays with high energies are rare, a large number of telescopes is required to capture the images. The MSTs and LSTs will be installed on both sites. The MSTs cover the core energy range of 150 GeV to 5 TeV. The LSTs cover the lowest energies, and can achieve rapid follow-up observation of transients with telescopes at other wavelengths. Fig. 2.6 shows the prototype LST located on CTAs northern hemisphere site.

Fig. 2.7 compares the angular resolution of CTA southern array and other γ -ray detectors. Above 200 GeV, CTA has the best angular resolution. *Fermi*-LAT has a better angular resolution than CTA below this value.

2.2.2 CTA Performance

Fig. 2.8 compares the differential sensitivity of CTA North and South and other γ -ray detectors. CTA has better detection ability than H.E.S.S., MAGIC and VERITAS by a factor of 5-20 depending on energy.

The IRFs have been turned to maximize the performance in terms of flux sensitivity. The optimal cuts depend on the duration of the observation, therefore the IRFs are provided for three different observation times. Both northern and southern arrays IRFs were simulated with



Figure 2.6: The prototype LST in La Palma (Spain). Credit: Antonio Gonzlez

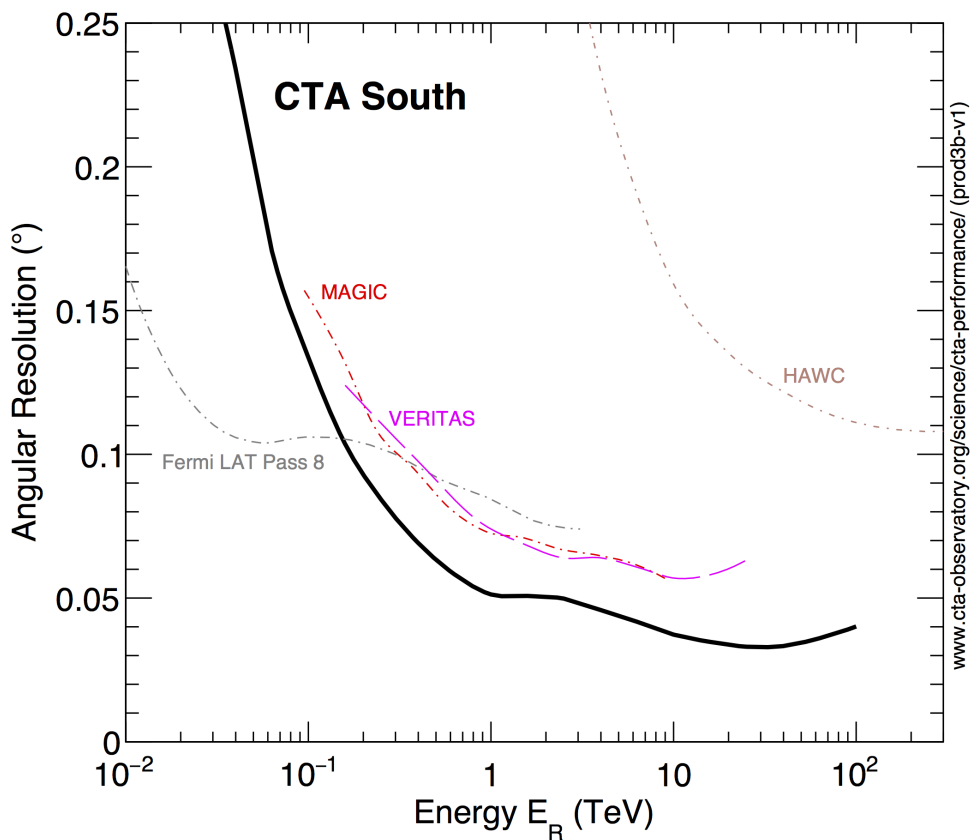


Figure 2.7: The angular resolution as a function of reconstructed energy. It shows the angle within which 68% of reconstructed γ -rays fall.

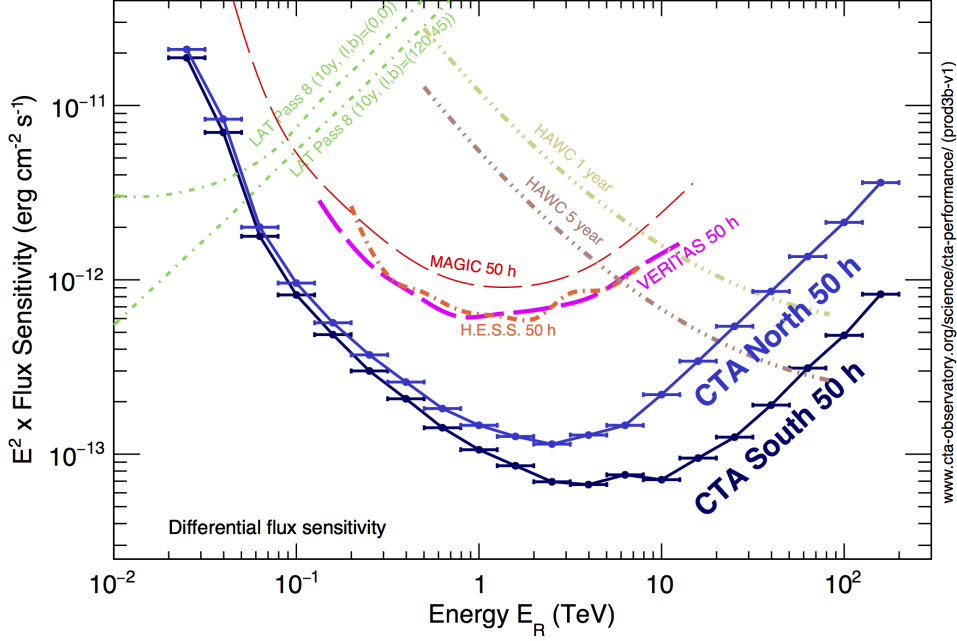


Figure 2.8: The differential sensitivity of CTA North and South and other instruments. The sensitivity curve is defined as the minimum flux needed by CTA to obtain a 5σ detection of a point-like source.

different exposure times of 0.5 hours, 5 hours and 50 hours. In total, the following IRFs are available: *North_0.5h*, *North_5h*, *North_50h*, *South_0.5h*, *South_5h* and *South_50h*. A power-law γ -ray spectrum with photon index of 2.62 following that of the Crab Nebula was assumed in the calculations, although none of the IRFs depends on the assumed spectral shape of the γ -ray source. It is needed for the estimation of $e(\vec{d})$. The presented research has made use of the CTA IRFs provided by the CTA Consortium and Observatory, see <http://www.cta-observatory.org/science/cta-performance/> (version prod3b-v1) for more details.

2.3 A Brief Summary

Above a certain energy, γ -rays can only be detected by ground-based detectors. These ground-based detectors are using the EAS produced in the atmosphere to characterize γ -rays, either detecting the particles or the produced Cherenkov light. IACT technique provides the direction and energy of γ -ray showers imaged in stereoscopic view. As the next-generation telescope, CTA has unprecedented sensitivity that is one order of magnitude better than current IACTs. It has wider energy range (20 GeV to 300 TeV), larger FoV (8 degrees for NectarCAM camera of MST), and better PSF. These make CTA a powerful instrument for future observations.

Chapter 3

Data Analysis

As discussed before, the CTA telescopes are still under construction, no real data has been produced yet. Therefore, the Data Challenge One (DC-1) data simulated by the CTA Consortium are used for preparing CTA science. In this chapter, we describe the analysis chain of DC-1 data, the reduction of PeVatron candidates, and the obtained SED for these candidates.

3.1 Analysis Chain

There are two high-level analysis packages for γ -ray astronomy data analysis developed by the CTA Consortium: `Gammapy` and `ctools`. Both `gammapy` and `ctools` are analysing reconstructed IACT events with energy and arrival directions that are classified according to their types (e.g. γ -like, CR-like).

`Gammapy`¹ is a prototype for the CTA Science Tools based on basic Python package, such as `Astropy`,² `Sherpa`,³ and other packages for modeling and fitting [57]. The `ctools` package⁴ provides a set of software tools for analysis of Imaging Atmospheric Cherenkov Telescope (IACT) data [84]. It supports the analysis of data from the future CTA, as well as data from existing IACTs such as H.E.S.S., VERITAS, and MAGIC. A single tool can be used as a compiled executable written in C++ or as a Python script. The former is called a *ctool* and the latter is called a *cscript*.

We use `ctools` for our analysis process in this work, following the analysis flow presented in Fig. 3.1. The three parts of our analysis are: data selection and imaging, binned analysis, and Maximum Likelihood (ML) fitting. The following sub-sections have been adapted from the `ctool` documentation.

¹<https://gammapy.org/>

²<http://www.astropy.org/>

³<http://cxc.cfa.harvard.edu/contrib/sherpa/>

⁴<http://cta.irap.omp.eu/ctools/index.html>

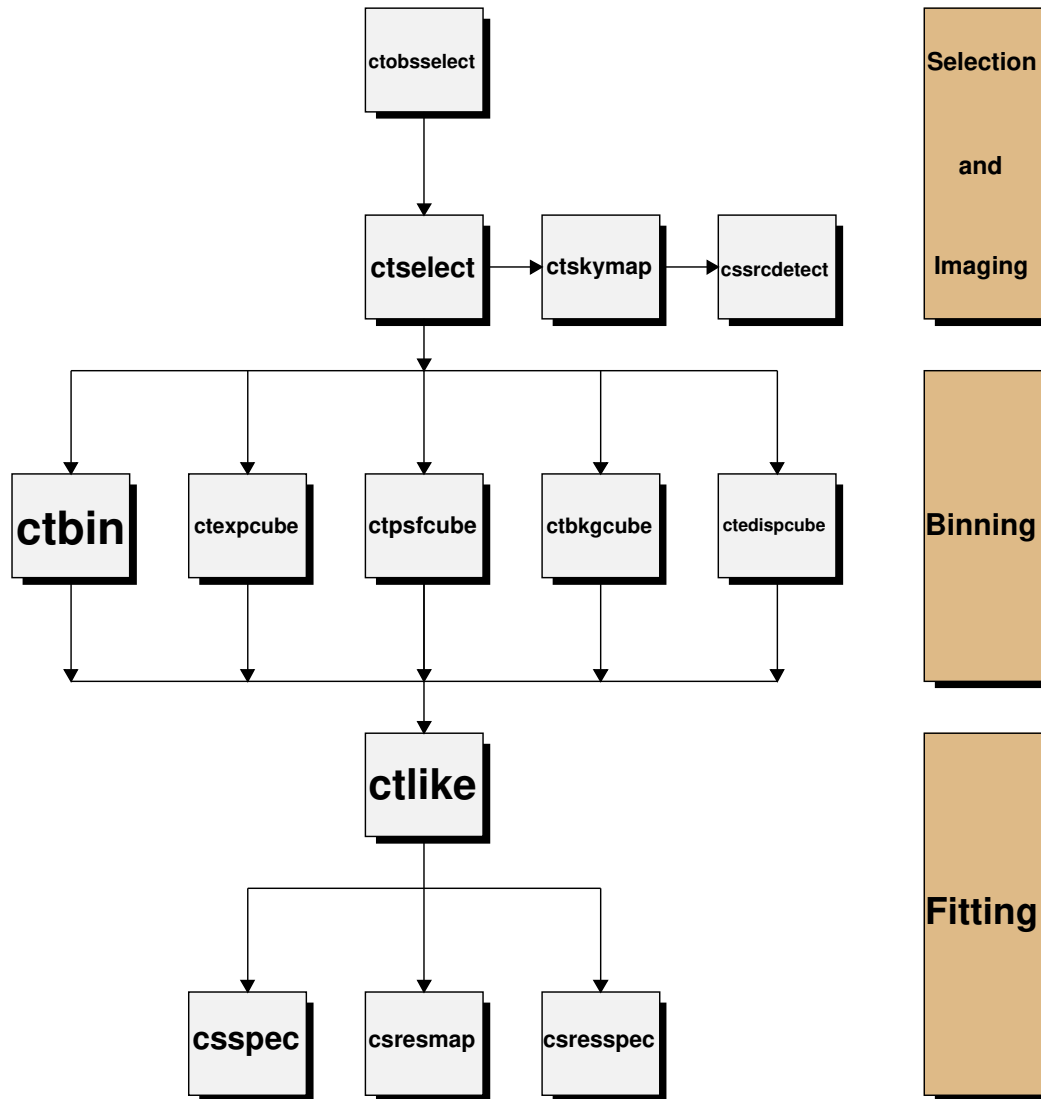


Figure 3.1: The cttools analysis process used in this thesis. It is divided into three blocks according to different aims.

3.1.1 Selection of observations and model building

The aim of this part is to select data for our analysis from the observation file, which corresponds to the first block in Fig. 3.1.

Firstly, we select data by using *ctobsselect*. Either a circle or a box can be used as the shape of pointing region. A selection circle with 3° radius is used. For the start and stop time for observation selection, there are four options: *INDEF*, *NONE*, *UNDEF*, and *UNDEFINED*. Since we should take into account the total time range simulated in DC-1, *INDEF* is chosen for the start and stop time, *tmin* and *tmax*, which means no time selection is performed.

After that, *ctselect* is used for sub-selection of events. An energy range between 100 GeV and 100 TeV is used, which is inside the energy range of DC-1. The declination of acceptance cone, coordinates, start time and stop time are chosen consistently with the values in *ctobsselect*.

After this, we use *ctskymap* to generate a sky map from the selected data. The tool produces a file *skymap.fits* which contains a sky map of the events in FITS format. The sizes of this map along the Galactic longitude and Galactic latitude axes is 200 pixels for each. There are three background subtraction methods: *NONE*, *IRF*, and *RING*. The *IRF* method uses templates contained in IRFs, which describe the spatial and spectral distributions of the background, to subtract the background contribution from the sky map. The *RING* method is specified for the ring-background subtraction method [13]. This is an alternative method that can be used when the *IRF* method has less precision, due to the fact that a reliable model of the instrumental background is not available. The number of background counts is estimated from a ring for each position in the map, scaled according to the background model in the IRFs. In our analysis, we use *NONE* background subtraction method.⁵ This means the background is not subtracted to display the skymap (following the simulation steps in [84]).

We use *cssrctest* to detect the candidate sources in a specific region. This tool generates a model definition file that contains point source model components for all sources that were selected in the sky map. All model components have a simple power law as spectral component, which is a reasonable starting condition for a subsequent model fitting using the *ctlike* tool. To detect the sources, *cssrctest* employs a peak finding algorithm that finds all peaks in the sky map above a given threshold. The detection threshold is set here to 5.0 which means that only the peaks that are ten standard deviations above the mean value of the sky map pixels are considered. For the background model type, there are four different types in *cssrctest*:

- *NONE*, no background model is added to the model definition XML file;
- *IRF*, a background model based on a template information in the Instrument Response Function is added;
- *AEFF*, a background model based on only the shape of the effective area is added;

⁵An isotropic diffuse background, *NONE*, is considered here. The different background subtraction methods would impact the view of skymap. It does not affect the binning and fitting processes.

- *CUBE*, a background model for stacked analysis is added.

We use *IRF* here for the background model type, following the instruction on *ctools* website.

3.1.2 Generation of data and instrument model cube

The aim of this part is to generate different count cubes from the data for preparing the binned analysis, corresponding to the second block of Fig. 3.1.

Here we stack the observations by using *ctbin*, *ctexpcube*, *ctpsfcube*, *ctedispcube* and *ctbkgcube*. The events are stacked into a count cube by using *ctbin*, which creates a 3-dimensional count cube as a function of coordinates and with 23 logarithmically spaced energy bins between 100 GeV and 100 TeV, which matches the energy resolution of CTA. Since the *ctbin* tool combines observations that may have different IRFs and exposure times into a single count cube, we compute the effective IRFs for this count cube before analyzing the data. For each component of the IRFs, there is a specific tool to perform such computation. The events from the FITS file of selected events are binned into a count cube stored into the file *cntcube.fits*. The *cntcube.fits* file produced by *ctbin* contains four extensions:

- a 3-dimensional image extension providing the number of events per count cube bin;
- a 3-dimensional image extension, *WEIGHT*, where each bin gives the fractional overlap between a count cube bin and the Region of Interest (ROI)⁶;
- a table extension, *EBOUNDS*, providing the energy boundaries of the count cube;
- a table extension, *GTI*,⁷ of the count cube, indicating the good time intervals to be used in the analysis.

The *ctexpcube* tool computes the exposure of the stacked count cube which is the effective area multiplied by the livetime for each observation. It needs as inputs the selected data and the *cnt.fits* file produced by *ctbin*. This tool produces the FITS file *expcube.fits* that contains the exposure information as a function of sky position and energy. The binning of the exposure cube from the count cube is extracted. However, the binning of the exposure cube does not need to correspond to that of the count cube. Exposure values are determined by interpolation from the values stored in the exposure cube file, which are the same as the point spread function and background cubes described below. *ctexpcube* produces an exposure cube FITS file that contains the exposure as a function of sky position and energy.

The *ctpsfcube* tool computes the weighted Point Spread Function (PSF) of the stacked count cube. We use the same energy range and energy bins as with *ctbin*. It produces a PSF cube FITS

⁶ROI is defined as a given radial acceptance region, within which the events are selected. Bins outside ROI will be masked.

⁷A Good Time Interval is a time range in which the data can be considered valid.

file that contains the weighted PSF as a function of sky position and energy. The PSF varies mildly over the field of view (FoV) of the camera, and consequently it is sufficient to sample this variation on a spatial scale of typically 1° .

The *ctbkgcube* tool computes a background cube that predicts the number of background events in the count cube. It needs as inputs the selected data and the *cnt.fits* file produced by *ctbin*. It produces a background cube FITS file that contains the predicted background rate as a function of the sky position and the energy according to the definition file of input data.

The *ctediscube* tool generates an energy dispersion cube for a stacked analysis from selected data. Although the fitting process including energy dispersion is more time consuming, it is important to consider the energy dispersion when we analyze the data down to low energy. An energy dispersion cube is a 4-dimensional cube spanned in Galactic longitude (or Right Ascension, R.A.) and Galactic latitude (or Declination, Dec), energy, and migration which is the ratio between reconstructed and true photon energy.

3.1.3 Source model

Since we need to know how the photon events are distributed as a function of sky position and energy range, it is necessary to presume some spatial models and spectral models. These models are needed for the reconstruction. Here we list different spatial and spectral models used in DC-1 simulation.

The spatial models of differential flux that are used in DC-1 are:

- Radial Gaussian

$$M_S(\theta) = \frac{1}{2\pi\sigma^2} \exp\left(-\frac{1}{2} \frac{\theta^2}{\sigma^2}\right), \quad (3.1)$$

- Radial Shell

$$M_S(\theta) = n_0 \begin{cases} \sqrt{\theta_{\text{out}}^2 - \theta^2} - \sqrt{\theta_{\text{in}}^2 - \theta^2} & \text{if } \theta \leq \theta_{\text{in}}, \\ \sqrt{\theta_{\text{out}}^2 - \theta^2} & \text{if } \theta_{\text{in}} < \theta \leq \theta_{\text{out}}, \\ 0 & \text{if } \theta > \theta_{\text{out}}, \end{cases} \quad (3.2)$$

where θ is the angular separation from the centre of the distribution, and σ is the Gaussian width of the distribution, $\theta_{\text{in}} = R$ and $\theta_{\text{out}} = R + W$ are the apparent inner and outer shell radii on the

sky, respectively. R is the inner radius and W is the shell width. In addition,

$$n_0 = \frac{1}{2\pi} \left(\frac{\sqrt{1 - \cos 2\theta_{\text{out}}} - \sqrt{1 - \cos 2\theta_{\text{in}}}}{2\sqrt{2}} + \frac{1 + \cos 2\theta_{\text{out}}}{4} \ln \left(\frac{\sqrt{2} \cos \theta_{\text{out}}}{\sqrt{2} + \sqrt{1 - \cos 2\theta_{\text{out}}}} \right) - \frac{1 + \cos 2\theta_{\text{in}}}{4} \ln \left(\frac{\sqrt{2} \cos \theta_{\text{in}}}{\sqrt{2} + \sqrt{1 - \cos 2\theta_{\text{in}}}} \right) \right)^{-1} \quad (3.3)$$

is a normalization constant.

The spectral models of differential flux that are used in DC-1 are:

- Power law 1: $M_E(E|t) = k_0 \left(\frac{E}{E_0} \right)^{-\gamma}$, with differential flux (or prefactor) k_0 in unit of $\text{ph cm}^{-2} \text{s}^{-1} \text{MeV}^{-1}$, index γ , pivot energy $E_0(\text{MeV})$
- Power law 2: $M_E(E|t) = \frac{N(\gamma+1)E^{-\gamma}}{E_{\text{max}}^{\gamma+1} - E_{\text{min}}^{\gamma+1}}$, with integral flux $N(\text{ph cm}^{-2} \text{s}^{-1})$, index γ , minimum energy $E_{\text{min}}(\text{MeV})$, maximum energy $E_{\text{max}}(\text{MeV})$
- Exponentially cut-off power law: $M_E(E|t) = k_0 \left(\frac{E}{E_0} \right)^{-\gamma} \exp\left(-\frac{E}{E_{\text{cut}}}\right)$, with prefactor k_0 ($\text{ph cm}^{-2} \text{s}^{-1} \text{MeV}^{-1}$), index γ , pivot energy $E_0(\text{MeV})$, cutoff energy $E_{\text{cut}}(\text{MeV})$,

3.1.4 Reconstruction of a source best-fit model

The aim of this part is to reconstruct the best-fit models and compare these to the simulated DC-1 data, corresponding to the third block of Fig. 3.1.

Since we have already prepared the model definition file and observations definition file, we run *ctlike* for ML fitting. There are two different analysis methods: binned mode and unbinned mode. The binned mode means that the events have been binned into a 3D count cube and the fit computes the log-likelihood function by summing over all the bins of the count cube. The unbinned mode means that the events are not binned into a count cube and the log-likelihood is computed directly by summing over all events, which makes it slower than the binned mode when the number of events is larger than the number of bins. At high energies, the count cubes generated by *ctbin* may be sparse with many empty pixels resulting from rare γ -ray events. It would be worth to analyze the events with an unbinned ML analysis in that case. An unbinned analysis is generally preferred over a binned analysis for short observation times (i.e. less than a few tens of hours). Since we analyze the candidates with thousands of hours of observation time, a binned mode analysis is adopted. The model definition file includes the spectrum type and spatial model type of the target source, the Galactic diffuse emission, the total background, and other sources in the FoV. The target sources in this thesis are considered following the model definition file of Galactic Plane Survey (GPS). The spectrum of the background is modelled as a

power law. The *ctlike* tool has the ability to estimate the detection significance for sources in the XML model. This is done by computing the Test Statistic (TS) value. The square root of the TS value is a rough estimation of the source detection significance in σ of Gaussian distribution, while the exact conversion depends on the formulation of the special statistics and the number of degrees of freedom (dof) associated with the source.

We check the residual maps and residual spectrum by using *csresmap* and *csrespec*, to decide whether we should improve the input spatial and spectral models. After doing the model fit we investigate the residuals to verify that the model components properly describe the observed event spatial distribution with *csresmap* and their spectral distribution with *csrespec*. The *csresmap* tool implements different algorithms for the computation of the residuals. These are:

- SUB: $n_{\text{data}} - n_{\text{model}}$;
- SUBDIV: $\frac{n_{\text{data}} - n_{\text{model}}}{n_{\text{model}}}$;
- SUBDIVSQRT: $\frac{n_{\text{data}} - n_{\text{model}}}{\sqrt{n_{\text{model}}}}$;
- SIGNIFICANCE: $(n_{\text{data}} - n_{\text{model}}) \times \sqrt{2 \times (n_{\text{data}} \times \ln(\frac{n_{\text{data}}}{n_{\text{model}}}) + n_{\text{model}} - n_{\text{data}})}$;

where n_{data} and n_{model} are the count numbers of data and model, respectively.

The *SIGNIFICANCE* algorithm is used for both *csresmap* and *csrespec*. With this representation, the residuals are expected to be distributed according to a normal distribution centered on zero and of rms equal to one. Notice that the computing time is related to the spatial extent of the source and to the spatial shape.⁸

After we are sure that the spectral model and the spatial model are fine, we run *csspec* to compute the source spectrum by fitting a model in a given set of spectral bins. It can compute the source flux and its uncertainty in each spectral bin, as well as the significance of the source detection. In addition, it can compute an upper limit (UL) on the flux, which is particularly useful in the case that the source is not significantly detected within a spectral bin. By default a confidence level (CL) of 95 % is used. There are three methods that could be run in *csspec*. For CTA-only observations, *method=SLICE* will be used. The energy interval is divided into several bins and an independent ML fit is performed in each bin. If data from other facilities should be fitted, *method=NODES* could be used. This method makes the spectral model be replaced by a node function.

As indicated in Fig. 3.1, *csresmap* is the key step to check whether the correct spectral and spatial model are chosen before the final reconstruction of SED.

⁸with a Gaussian disk model taking considerably more computing time than a radial disk model due to the tails of the Gaussian function

3.2 Supernova remnants simulated in the DC-1 of CTA

3.2.1 The Galactic Plane Survey of DC-1

The CTA Science has already been introduced in chapter 1. The GPS of CTA should achieve several goals, including identification of Galactic PeVatron candidates.

As explained previously, we use the GPS data of DC-1 to judge which sources would be the most promising one for CTA PeVatron observation. The DC-1 are high-level data in a form of event lists and IRF. Zenith angles of 20° and 40° with 50 hours of observation time were simulated. This range of zenith angles corresponds to optimal observing conditions. The Galactic Plane survey contains 3270 observations, with 30 minutes for each observation. The data were simulated for an energy range from 30 GeV to 160 TeV and a time range of 2021-01-01 to 2021-04-18 with 5° as maximum off-axis angle.⁹

Each event file contains the events for an observation and comprises an event list and a Good Time Intervals (GTI) binary table extension. The header of the EVENTS table contains information about the observation such as the start and stop date and time, the duration and livetime of the observation, and the pointing direction in Right Ascension and Declination.

3.2.2 Candidate PeVatrons in DC-1

As PeVatrons can accelerate particles at least to PeV energies, yielding γ -rays at TeV energies, we choose several SNRs from TeVcat. There are three types of SNRs in TeVcat: Shell, SNR-MC, and Composite SNR. The shell-type SNRs emitting very-high-energy (VHE) γ -rays from shell structure, are mostly young objects ($t < 5$ kyr) [6]. In case of shell-type SNRs with larger angular size, their VHE γ -rays are spatially resolved with a shell-type morphology [45]. The system of a SNR interacting with a Molecular Cloud (MC) (SNR-MC) emitting VHE γ -rays are older objects ($t > 10$ kyr) compared to shell-type SNRs [86]. A soft spectrum at GeV-TeV energies is one of the typical characteristics of SNR-MC systems. A composite SNR consists of a pulsar wind nebula (PWN) and a pulsar inside the SNR. The γ -ray emission from such systems could originate from the pulsar, the PWN, and the SNR itself.

Sources with low Galactic latitude (between -1° and 1°) are chosen so that we can extract data from the GPS.¹⁰ We run *cssrcdetect* from *ctools* (with a 10σ selection threshold) to check whether the sources are considered in DC-1. We choose Supernova Remnants (SNRs) from TeVcat as a first step. The coordinates, the type and the distance of the sources are shown in Table 3.1. The method for measuring the distance will be introduced in next section. In total, 18 SNRs are considered, as shown in Table 3.1.

There are 102 SNRs candidates in the First *Fermi* Supernova Remnant Catalog, 30 of which

⁹It is not representative of the real time span of the KSP.

¹⁰Cassiopeia A, Tycho, RCW 86 from Fig. 1.7 are not included since they are out of this Galactic latitude region.

SNR name	Galactic Longitude [deg]	Galactic Latitude [deg]	Type	Distance [kpc]
HESS J1534–571	323.65	-0.92	Shell	no
HESS J1614+516	331.52	-0.58	Shell	no
RX J1713.7–3946	347.34	-0.47	Shell	1 ^(a)
CTB 37B	348.65	0.38	Shell	13.2 ^(b)
HESS J1731–347	347.34	-0.47	Shell	3.2 ^(c)
HESS J1912+101	44.39	-0.07	Shell	4.1 ^(d)
0FGL J1954.4+2838	65.30	0.38	Shell	9.2 ^(e)
SNR G318.2+00.1	318.36	-0.43	SNR/Molec. Cloud	no
CTB 37A	348.39	0.11	SNR/Molec. Cloud	7.9 ^(f)
SNR G349.7+00.2	349.72	0.17	SNR/Molec. Cloud	11.5 ^(g)
HESS J1745–303	358.71	-0.64	SNR/Molec. Cloud	no
HESS J1800–240C	5.71	-0.06	SNR/Molec. Cloud	2 ^(h)
HESS J1800–240B	5.90	-0.37	SNR/Molec. Cloud	2 ⁽ⁱ⁾
W 28	6.66	-0.27	SNR/Molec. Cloud	2 ^(j)
HESS J1800–240A	6.14	-0.63	SNR/Molec. Cloud	2 ^(k)
W 49B	43.32	-0.16	SNR/Molec. Cloud	11.3 ^(l)
W 51C	49.12	-0.36	SNR/Molec. Cloud	5.4 ^(m)
SNR G015.4+00.1	15.41	0.16	Composite SNR	4.8 ⁽ⁿ⁾

Reference of distance: ^(a)[41]; ^(b)[108]; ^(c)[94]; ^(d)[102]; ^(e)[107]; ^(f)[108]; ^(g)[36]; ^(h)[32]; ⁽ⁱ⁾[32]; ^(j)[111]; ^(k)[32]; ^(l)[101]; ^(m)[101]; ⁽ⁿ⁾[28];

Table 3.1: Information on source candidates. From left to right: the name of the sources, the Galactic Longitude, the Galactic Latitude, the source type following TeVCat, and the distance whenever measured.

are classified as the GeV counterparts of radio SNRs [47]. Both faint SNRs and bright SNRs have been simulated in DC-1 GPS data. The faint group includes 996 SNRs with NodeFunction spectrum type¹¹ and RadialShell spatial type. The bright group includes the brightest SNRs detected by *Fermi*-LAT and IACTs.

Some of the TeVCat SNRs that we selected, are not included in DC-1. Finally, we are left with 9 sources shown in Table 3.2.

3.2.3 Distance Measurement

The purpose for table 3.1 to list the distances of the sources is that we need to model the SEDs by using these values. Several methods have been proposed to measure the distance of SNRs:

- a combination of the HI 21 cm and CO lines [101];
- the relation between surface brightness and physical diameter of shell-type radio SNRs [27];
- the extinction - distance relation of SNRs;

¹¹NodeFunction means the arbitrary number of energy-intensity nodes. All the energy and intensity values are given for special values.

- possible association with other sources (e.g. pulsar).

The measurement method for the candidates in our analysis are:¹²

RX J1713.7–3946: The velocity from CO distribution reveals a distance of 0.5 to 1.6 kpc kinematically [66].

HESS J1731–347: Observation with the Mopra radio telescope, targeting CO(1-0), ¹³CO(1-0) and CS(1-0) emission, give a kinematic distance around 3.2 kpc for HESS J1731–347 [94].

HESS J1912+101: The distance to the SNR is estimated to be ~ 4.1 kpc based on the HI self-absorption method [103].

W 28: Its distance is estimated between 1.6 kpc and 4 kpc, based on kinematic determinations and H observations [92].

HESS J1800–240A: Same as for W 28.

W 49B: The kinetic distance of this SNR is 11.3 kpc based on absorption features of H I 21 cm line and ¹³CO line observations [101].

W 51C: The kinetic distance of W 51C is 5.4 kpc based on absorption features of H I 21 cm line and ¹³CO line observations [101], following the same measurement method as for W 49B.

The distances of W 28 and HESS J1800–240A are measured by using the relation between surface brightness and physical diameter. While for other sources, CO and HI emission lines are used.

3.3 Supernova remnants reconstructed from DC-1

3.3.1 Analysis of a typical source: HESS J1614+516

We take HESS J1614–518 as an example to illustrate the analysis chain. An energy range between 100 GeV and 100 TeV with a 3°-radius selection circle are chosen. For the moment, all detected sources are added as point sources with power law spectral shapes to the model definition XML file.

Table 3.2 lists the source type, spectrum type and spatial model type of all considered candidates. HESS J1614–518 was simulated with a power law spectrum type $M_E(E|t) = \frac{N(\gamma+1)E^\gamma}{E_{\max}^{\gamma+1} - E_{\min}^{\gamma+1}}$ and a radial Gaussian spatial model $M_S(\vec{p}|E, t) = \frac{1}{2\pi\sigma^2} \exp\left(-\frac{1}{2} \frac{\theta^2}{\sigma^2}\right)$. HESS J1616–508 (not our target) is close to HESS J1614–518 in the FoV of CTA, and was also simulated with a

¹²No distance measurements for HESS J1614+516 and HESS J1745–303.

power law spectrum type and a radial Gaussian spatial model. We freeze the coordinates of both sources. We also freeze the photon index and extent of HESS J1616–508 to the simulated values. The interstellar emission model and BackgroundModel were simulated with ConstantValue and power law respectively. For the ML analysis *clike* of HESS J1614–518, the prefactor and index of the power law spectrum, and the extent of radial Gaussian spatial model are free parameters. Since HESS J1616–508 is a bright source, its prefactor is set as free parameter. In addition, the Interstellar Emission Model (IEM) values, the prefactor, and index of BackgroundModel are free parameters.

SNR name	source type	spectrum type	spatial model type
RX J1713.7–3946	Diffuse Source	Exp. Cut-off Power Law	Diffuse Map
HESS J1614+516	Extended Source	Power Law	Radial Gaussian
HESS J1731–347	Extended Source	Power Law	Radial Shell
HESS J1912+101	Extended Source	Power Law	Radial Gaussian
HESS J1745–303	Extended Source	Power Law	Radial Gaussian
W 28	Extended Source	Power Law	Radial Gaussian
HESS J1800–240A	Diffuse Source	Power Law	Diffuse Map
W 49B	Point Source	Power Law	Point Source
W 51C	Extended Source	Power Law	Radial Gaussian

Table 3.2: All simulated spectral and spatial models of the sources from DC-1. From left to right: name of the source, the source type following DC-1, the spectral model, and the spatial model.

Our aim for *ctools* analysis is to produce the spectral energy distribution (SED) of the sources. We need to extract the residual maps and the residual spectrum to make sure the ML analysis process is fine.

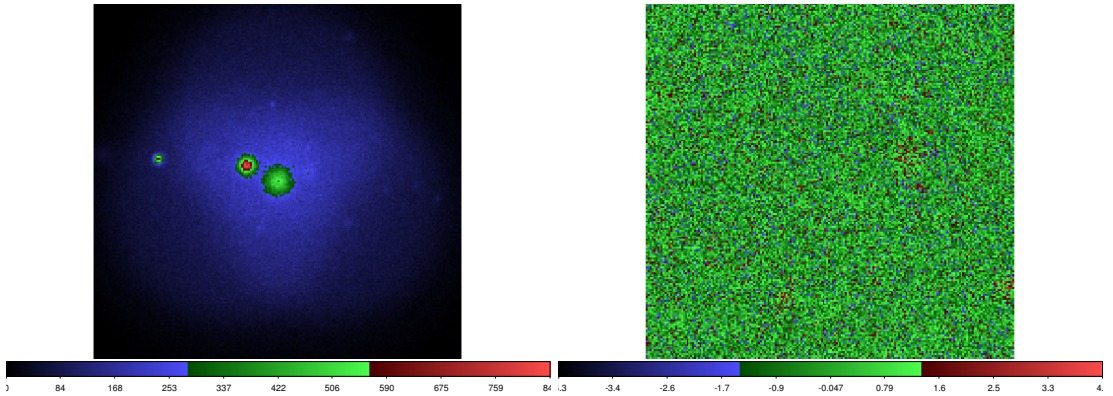


Figure 3.2: Left: The sky map of HESS J1614–518 covering an area of $10^\circ \times 10^\circ$. Right: The residual map of HESS J1614–518 obtained by subtracting the model map from the count map covering an area of $4^\circ \times 4^\circ$.

The left panel of Fig. 3.2 shows the sky map of HESS J1614–518, which includes HESS J1614–518 (central point), HESS J1616–508 and an unknown faint source in the FoV. The sky map is centred on the location of the HESS J1614–518 and consists of 200×200 spatial pixels of

0.05×0.05 degrees in size covering an area of $10^\circ \times 10^\circ$. It is displayed using SAOImage DS9¹³ in linear color scale. The right panel of Fig. 3.2 shows the residual map of HESS J1614–518 and consists of 200×200 spatial pixels of 0.02×0.02 degrees in size covering an area of $4^\circ \times 4^\circ$. Since we focus on the area around the target source to check the residual map, we make a smaller size for it compared to the sky map. Fig. 3.2 uses Galactic Longitude as X axis and Galactic Latitude as Y axis. The right panel uses SIGNIFICANCE algorithm as color bar. Since the parameters of the spectral model and the spatial model match the simulated observations, the residual map is smooth with little fluctuations. There are no significant residual, which indicates that the model fit is also satisfactory as a function of arrival direction.

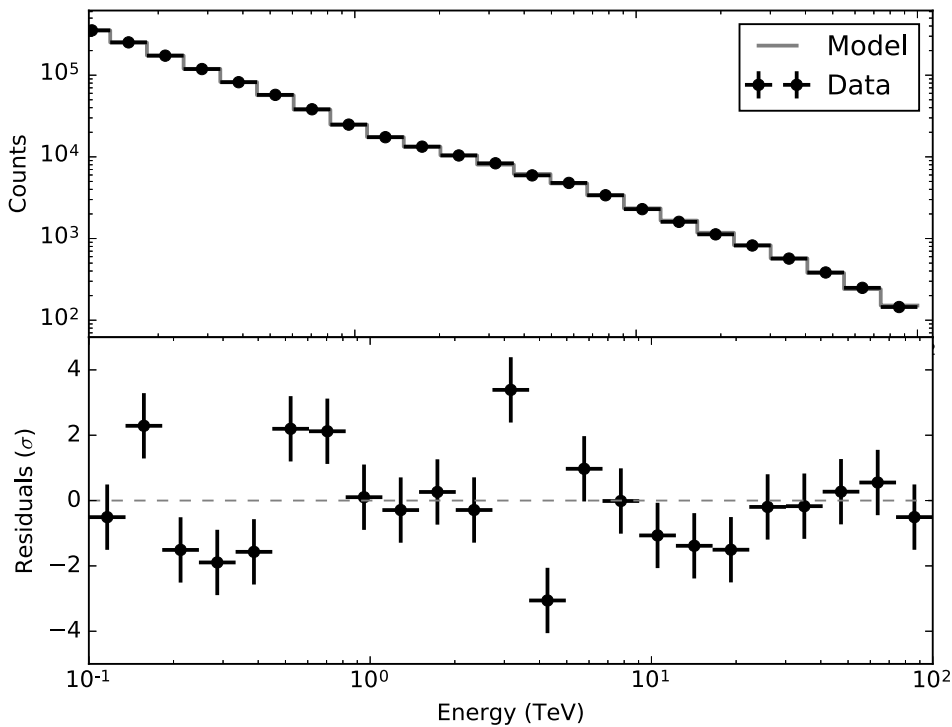


Figure 3.3: The residual spectrum of HESS J1614–518. The upper panel shows the data points and model together. The lower panel shows the residual values for each bin.

The upper panel of Fig. 3.3 shows the data points and the model of HESS J1614–518 as a function of energy. The lower panel of Fig. 3.3 shows the residual values for each bin. All the residual values are smaller than 4σ . The residual values are around zero, which means that models and data points are similar to each other in the upper panel. Thus the model fit is also satisfactory for the whole energy range.

Once the best-fit values for both spatial and spectral models are obtained, we can obtain the SED. Fig. 3.4 shows the SED of HESS J1614–518 between 100 GeV and 100 TeV with 23 bins.

¹³SAOImage DS9 is an astronomical imaging and data visualization application.

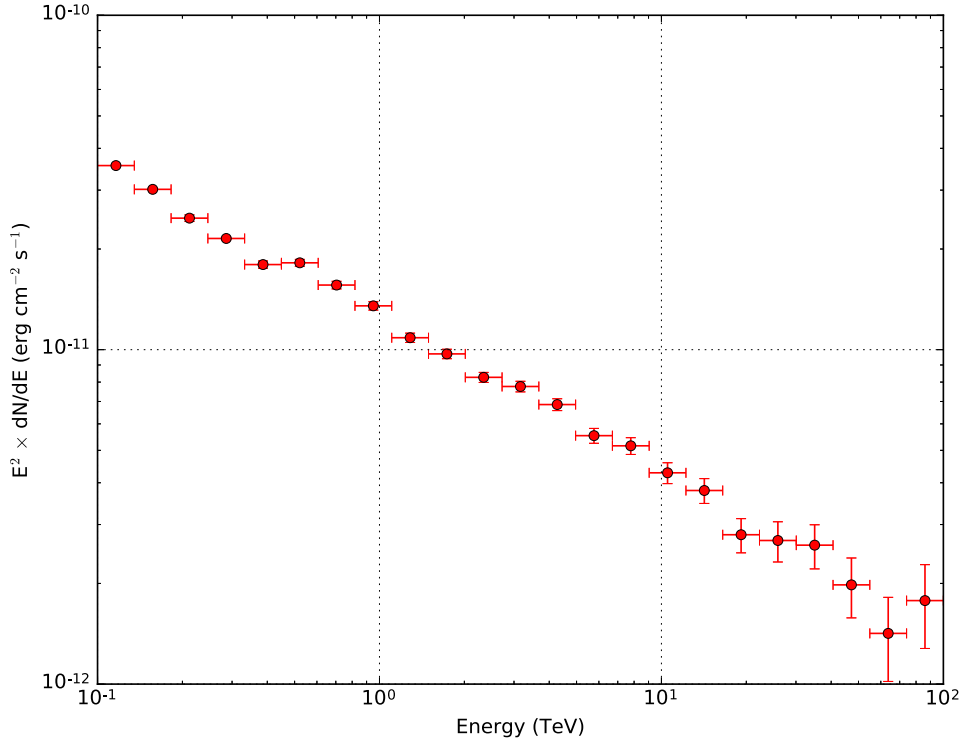


Figure 3.4: SED of HESS J1614–518. $E^2 \times \frac{dN}{dE}$ with uncertainty are shown as a function of energy from 100 GeV to 100 TeV.

Each energy bin is consistent with the corresponding energy bin in Fig. 3.3. For higher energies, lower γ -ray statistics results in large $E^2 \times \frac{dN}{dE}$ uncertainty.

The simulated parameters in DC-1 and reconstructed parameters of HESS J1614–518 are shown in table 3.3. These parameters are similar to each other, which means that the reconstruction of the spectral and spatial models in our analysis aligns with DC-1 simulated data.

There are some problems when we try to reconstruct the spectra down to 30 GeV. In order to avoid this, we use 100 GeV as the energy threshold. Such problems may be related to either the Galactic diffuse γ -ray emission or the simulation method in DC-1.

SNR name	$k_{0, \text{in}}$	$k_{0, \text{out}}$	γ_{in}	γ_{out}	σ_{in}	σ_{out}	$E_{\text{cut, in}}$	$E_{\text{cut, out}}$
RX J1713.7–3946	2300	2260 ± 10	2.06	2.06 ± 0.01			12.9	12.87 ± 0.34
HESS J1614+516	5780	5684.00 ± 52.00	2.46	2.46 ± 0.01	0.23	0.227 ± 0.001		
HESS J1731–347	467	455.00 ± 6.00	2.32	2.32 ± 0.01	0.22	0.219 ± 0.004		
					0.05	0.051 ± 0.008		
HESS J1800–240A	76.5	76.6 ± 2.00	2.5	2.56 ± 0.02				
W 49B	31.5	32.79 ± 1.32	3.14	3.07 ± 0.04				
HESS J1912+101	350	333.47 ± 6.05	2.7	2.67 ± 0.01	0.26	0.244 ± 0.003		
HESS J1745–303	284	279.32 ± 6.28	2.71	2.72 ± 0.01	0.20	0.204 ± 0.003		
W 28	75	122.59 ± 3.26	2.66	2.71 ± 0.02	0.17	0.108 ± 0.002		
W 51C	97	96.60 ± 3.20	2.58	2.56 ± 0.03	0.12	0.119 ± 0.003		

Table 3.3: Simulated and reconstructed parameters of the sources. From left to right: source name, simulated prefactor (in unit of $10^{-14} \text{ ph cm}^{-2} \text{ s}^{-1} \text{ TeV}^{-1}$), reconstructed Prefactor, simulated power law index, reconstructed power law index, simulated spatial extension (in unit of deg), and reconstructed spatial extension. Pivot energy $E_0 = 1 \text{ TeV}$.

3.3.2 Analysis of DC-1 PeVatron candidates

We follow the same analysis chain as that explained for HESS J1614–518 to get the results for the other sources. The background model of *CTA_{IRF}Background* is considered for each source as a power-law spectrum. The neighbouring sources of each candidate in the FoV are shown. There are some problems at low energies (100 GeV to 200 GeV) for HESS J1912+101, W 49B and W 51C, so we set 200 GeV as a lower energy bound for these sources. As the same reason we mentioned on previous section, such problems may be related to either the Galactic diffuse γ -ray emission or the simulation method in DC-1. For the other sources, we use 100 GeV as a lower energy bound. We can see in the following that all the sources show a good agreement between model and data, which means that the reconstructed parameters are similar to the simulated parameters for each source. A pivot energy of $E_0 = 1$ TeV is adopted for all sources. For the sky maps and residual maps, we use $10^\circ \times 10^\circ$ and $4^\circ \times 4^\circ$ for area, respectively. The simulated parameters in DC-1 and reconstructed parameters of all our targets are shown in table 3.3.

3.3.3 DC-1 spectra and visibility of PeVatron candidates

The differential sensitivity is defined as the minimum flux needed for CTA to obtain a 5σ detection of a source in the considered energy bin. It is created by the *cssens* tool and calculated for 5 bins per decade in logarithmic spanning. In addition, at least 10 detected γ -rays per bin and a 1/20 signal to background ratio are required. The differential sensitivity curves are calculated between 30 GeV and 150 TeV with 40° zenith angle and 50 h integration time. The sensitivity curve flux value decreases until the the energy is around few TeV, and then increases. This means that the detectability first increases and then decreases. At low energies, large amounts of background γ -ray like events result in low detectability of target sources. At high energies, low γ -ray statistics results in a low detectability of target sources. Fig. 3.13 shows the SED of all candidates in comparison with the sensitivity curves for CTA northern and southern sites. All SEDs lie above sensitivity curves (Fig. 3.13).

As seen in Fig. 3.13, the shell-type SNRs RX J1713.7–3946 and HESS J1614–518 are the brightest sources having hard SED spectra in the sample. Although RX J1713.7–3946 is the brightest one from 100 GeV to 20 TeV, it drops very steeply above 20 TeV, where its flux is below that of HESS J1614–518. HESS J1731–347 is the third promising candidate, even if its flux is lower than that of HESS J1745–303 and HESS J1912+101 below 1 TeV.

Besides the flux, visibility is another important factor to be considered for this work. Therefore, to verify whether the candidates can be seen by CTA or not, the visibility obtained from TeVCat over one year are investigated. 55° is used for the threshold Elevation Angle value.

We take HESS J1614–518 as an example. Fig. 3.14 illustrates the visibility for both southern and northern sites of CTA obtained from TeVCat. The color bar shows the Elevation Angle. The text in each plot gives the observable hours at different Elevation Angles. HESS J1614–518 can not be observed from the CTA northern site. While for the CTA southern site, HESS J1614–518 can be observed when its Elevation Angle is larger than 55° . The observation time above this value is 1409.8 h (from TeVCat). The visibility time over a one year period are simulated in Table 3.4. As a conclusion, HESS J1912+101, W 49B and W51C are visible in the CTA northern site. All candidates expect W 51C are visible in the CTA southern site.

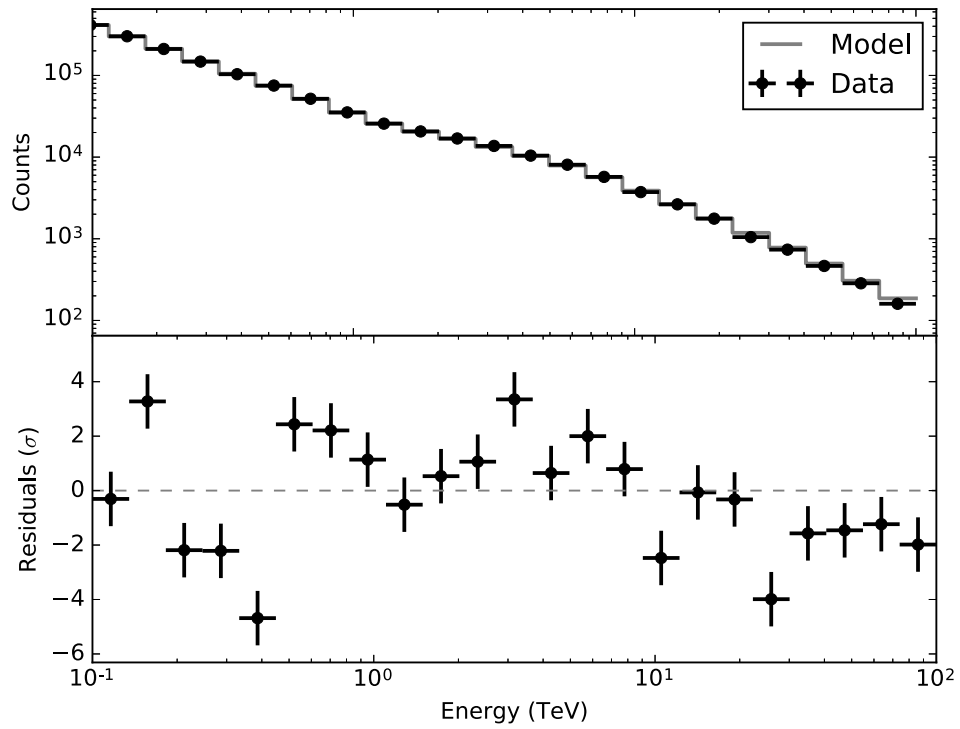
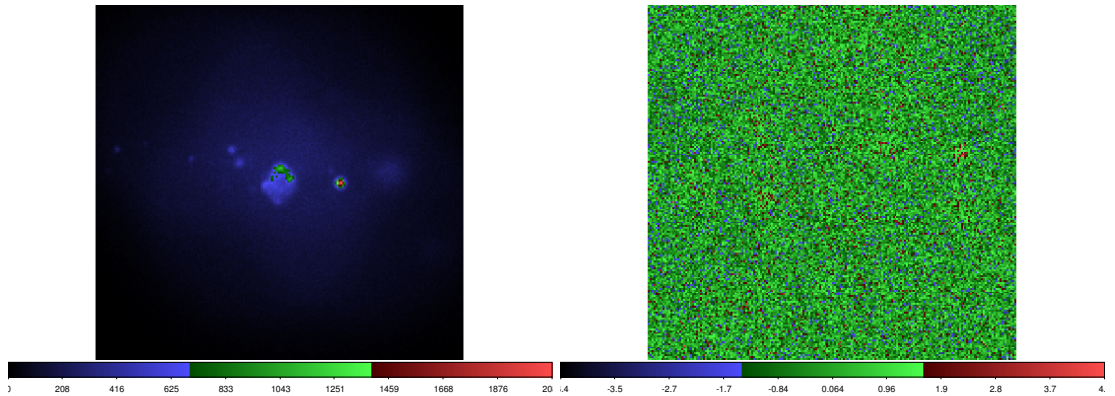


Figure 3.5: The upper part shows the sky map (left) and the residual map (right) of **RX J1713.7–3946**, obtained by subtracting the model map from the count map. These maps include CTB 37A and CTB 37B in the FoV. Both CTB 37A and CTB 37B are simulated with a power-law spectrum (with simulated index of 2.3 and 2.7) and radial Gaussian extension. The parameters of these two neighbour sources are frozen, which is the same as what we discuss for HESS J1614–518. The lower panel shows the residual spectrum of RX J1713.7–3946. The residual values locate between -5σ and 4σ

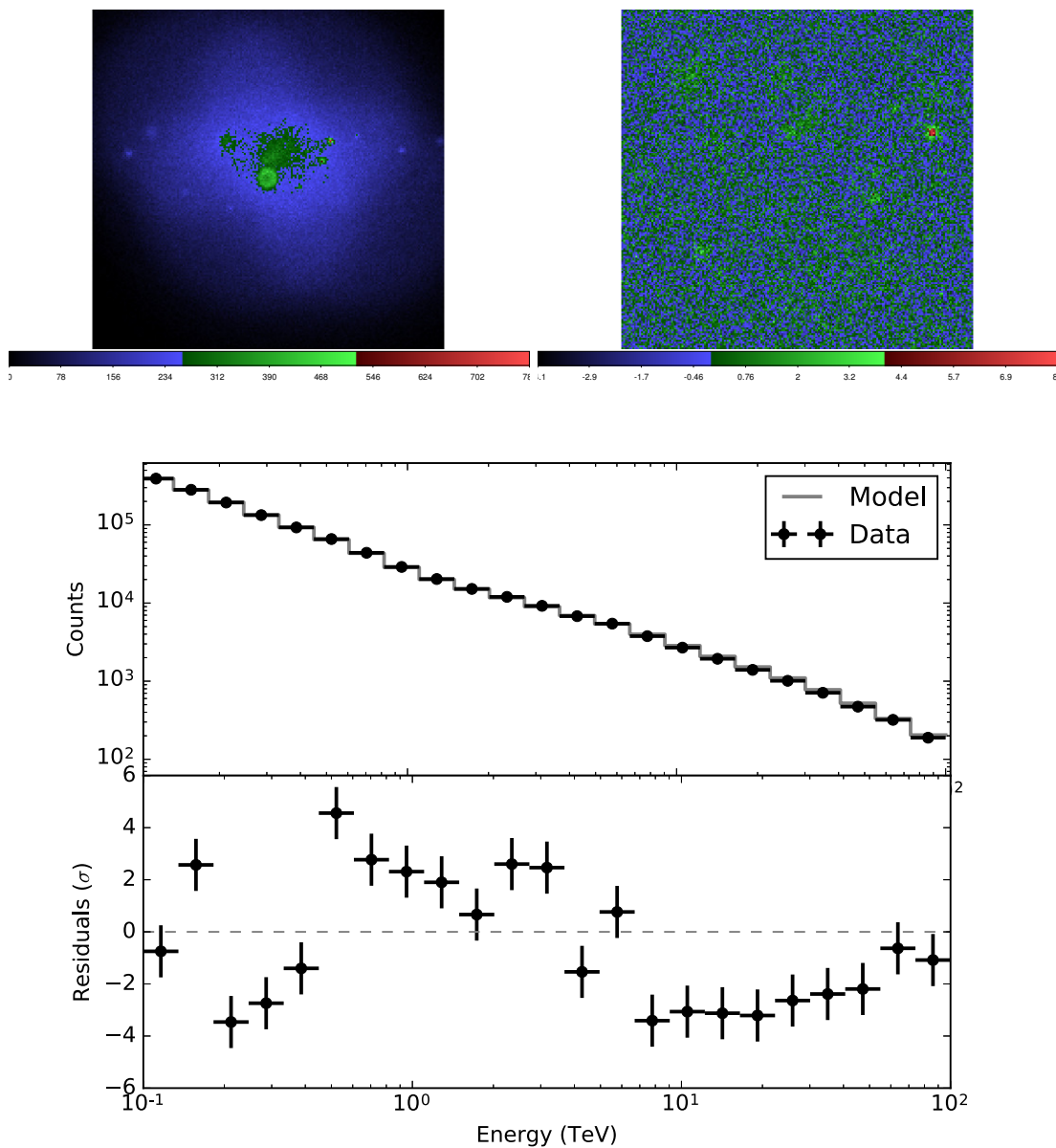


Figure 3.6: The upper part shows the sky map (left) and the residual map (right) of **HESS J1731–347**, obtained by subtracting the model map from the count map. The lower panel shows the residual spectrum of HESS J1731–347. The residual values locate between -4σ and 5σ .

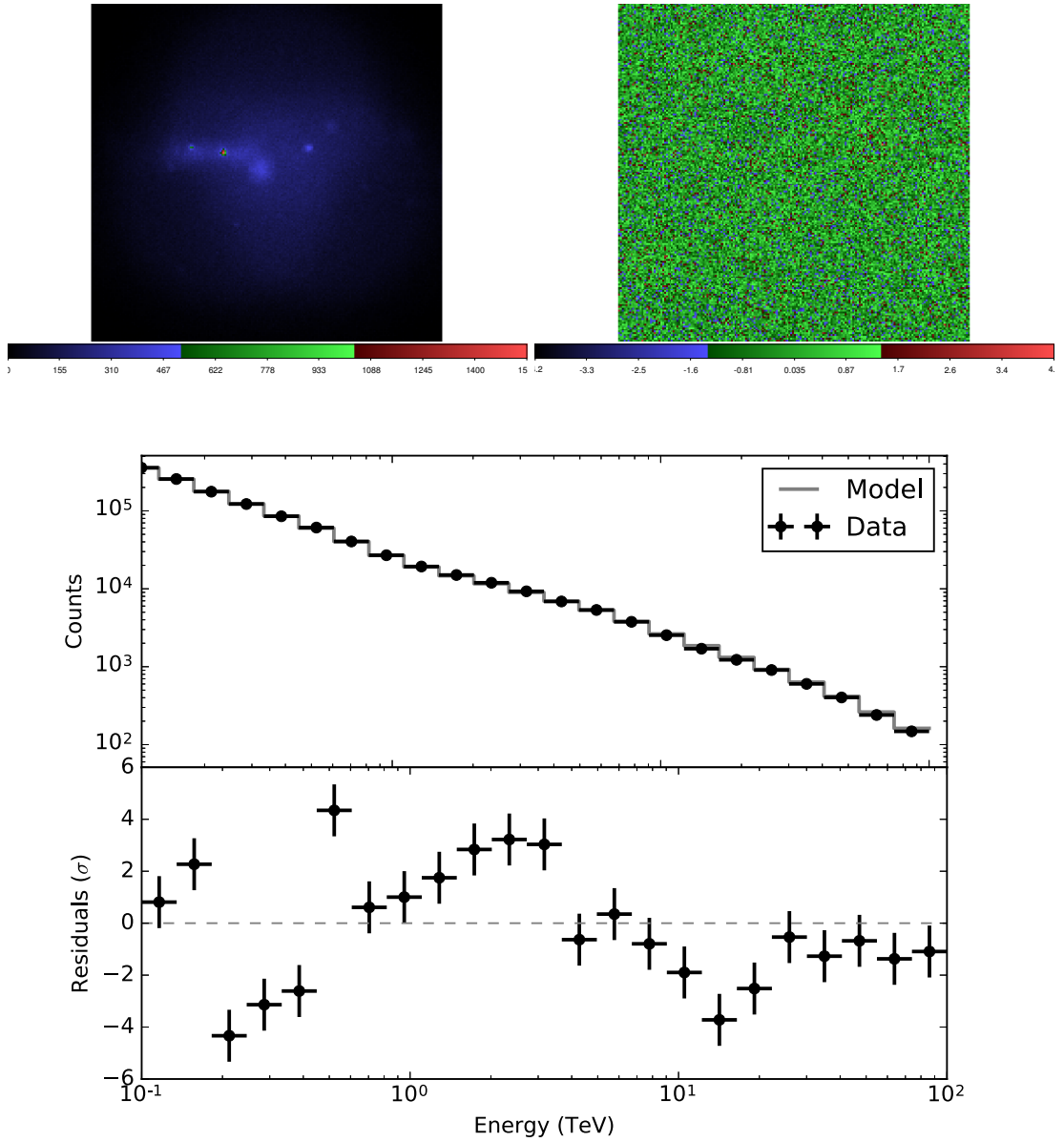


Figure 3.7: The upper part shows the sky map (left) and the residual map (right) of **HESS J1745–303**, obtained by subtracting the model map from the count map. The Galactic Centre also include in the FoV, is simulated with an exponential cutoff power-law (ECPL) spectrum and a point source extension. The lower panel shows the residual spectrum of HESS J1745–303. The residual values locate between -5σ and 5σ .

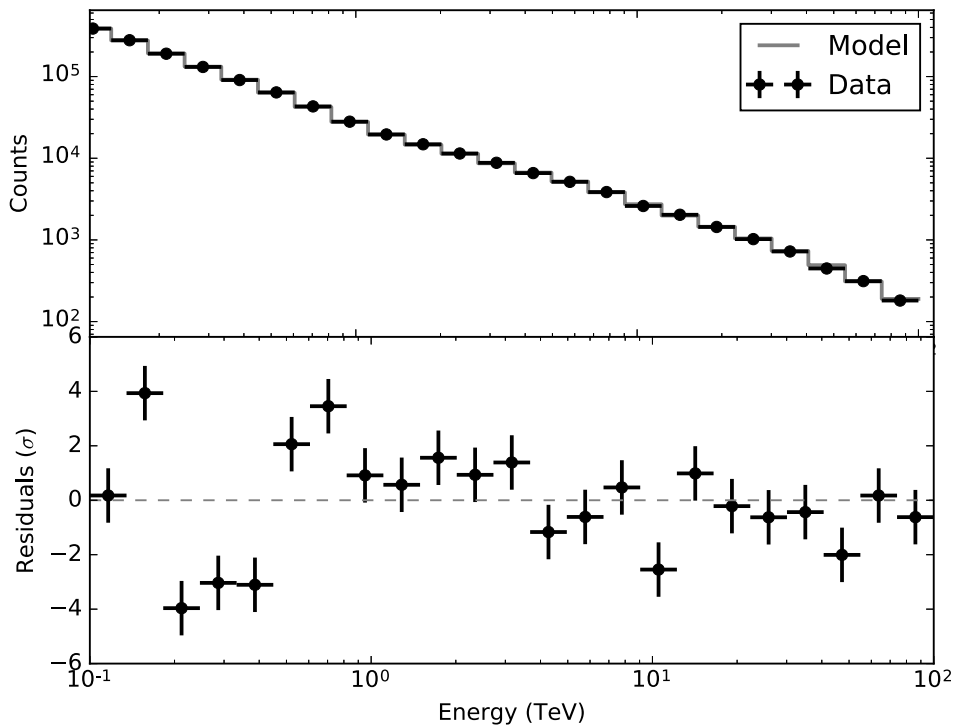
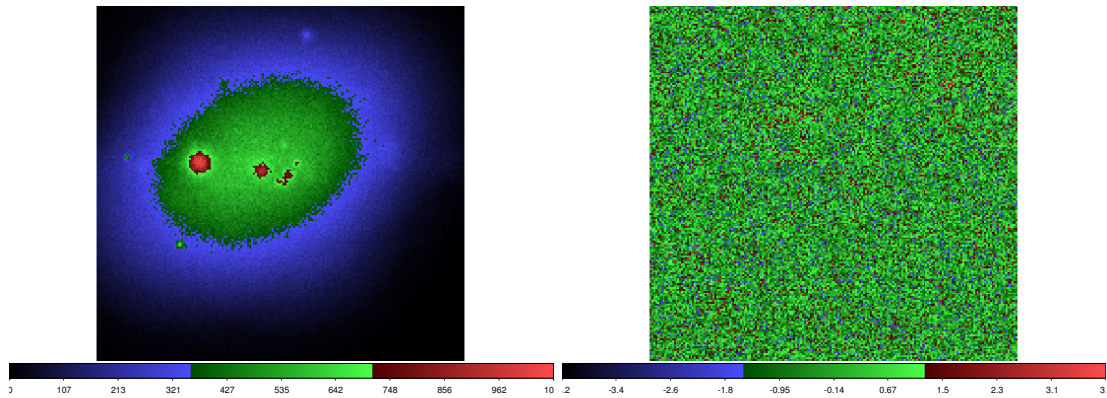


Figure 3.8: The upper part shows the sky map (left) and the residual map (right) of **HESS J1800–240A**, obtained by subtracting the model map from the count map. These maps include HESS J1800–240B, HESS J1800–240C and W 28 also in the FoV. All three sources are simulated as power-law spectra. HESS J1800–240B and HESS J1800–240C are simulated as a DiffuseMap extension while W 28 is simulated as a radial Gaussian. The lower panel shows the residual spectrum of HESS J1800–240A. The residual values locate between -4σ and 4σ .

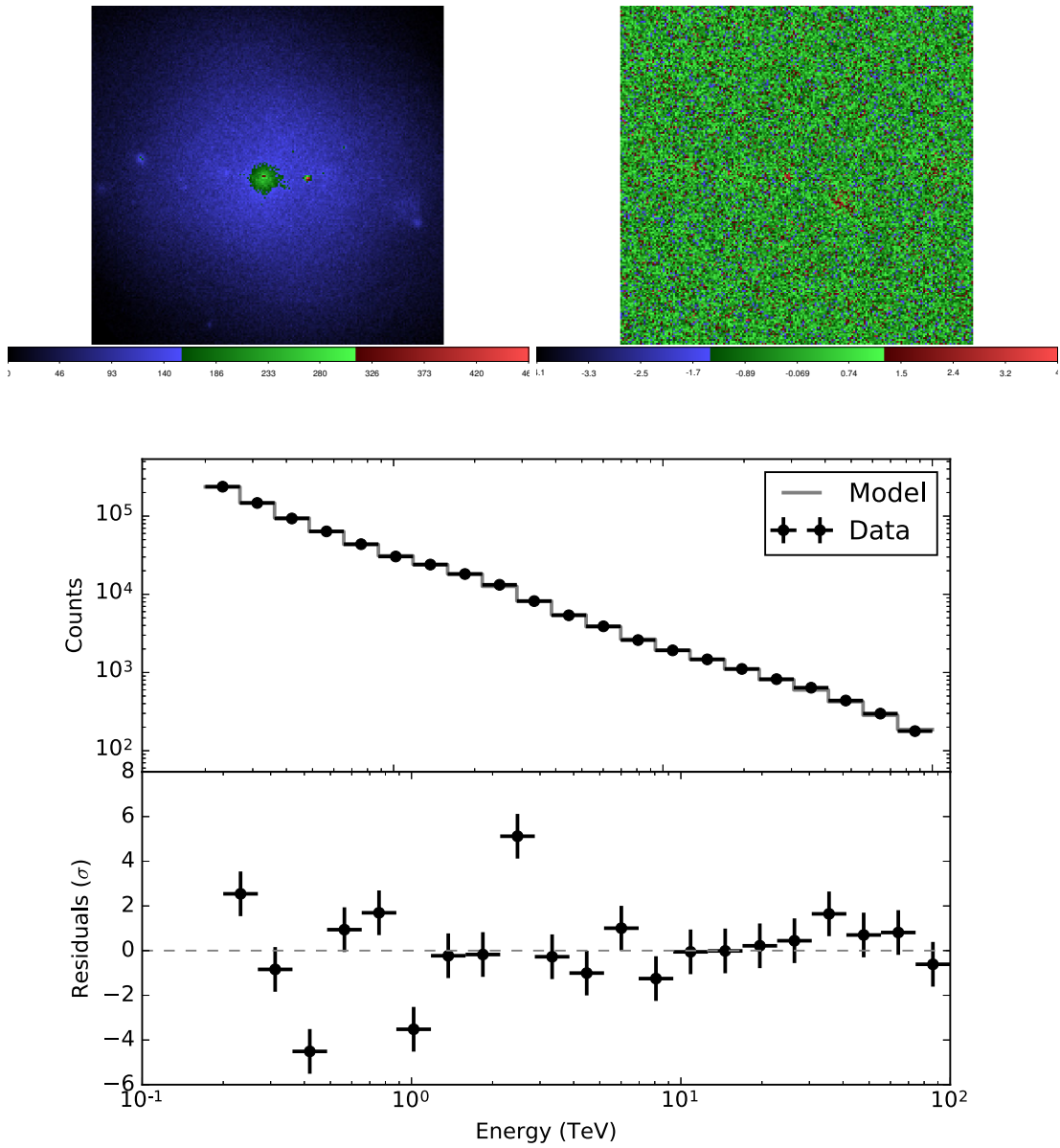


Figure 3.9: The upper part shows the sky map (left) and residual map (right) of **HESS J1912+101**, obtained by subtracting the model map from the count map. These maps include W 49B also in the FoV. The lower panel shows the residual spectrum of HESS J1912+101. Since there are some huge amplitude fluctuations between 100 GeV and 200 GeV, we use 200 GeV as the minimum energy value.

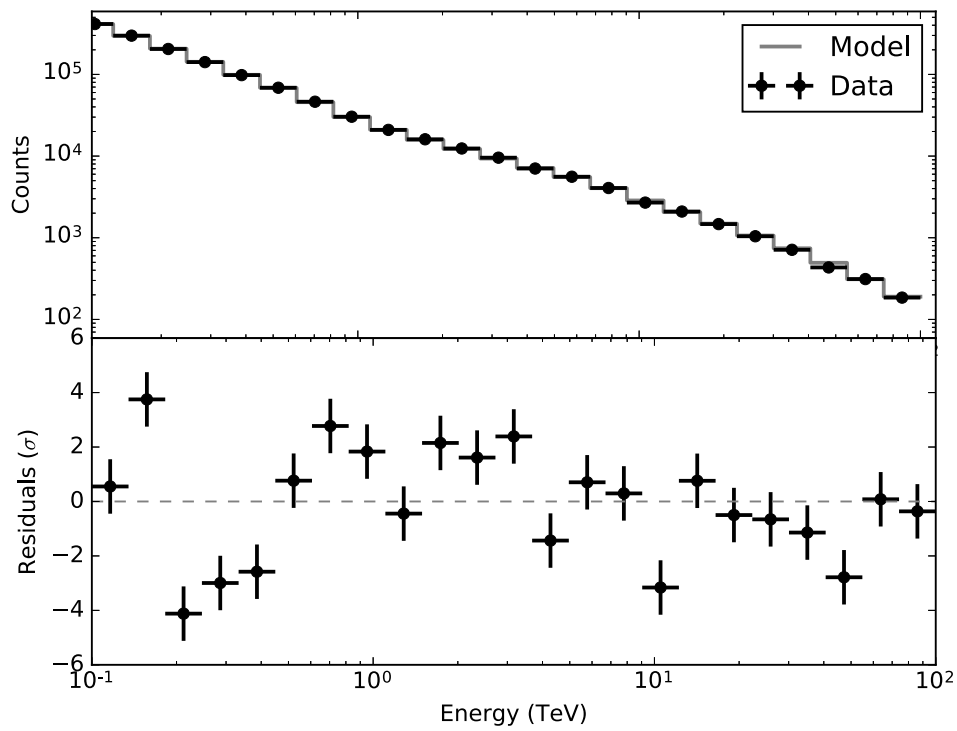
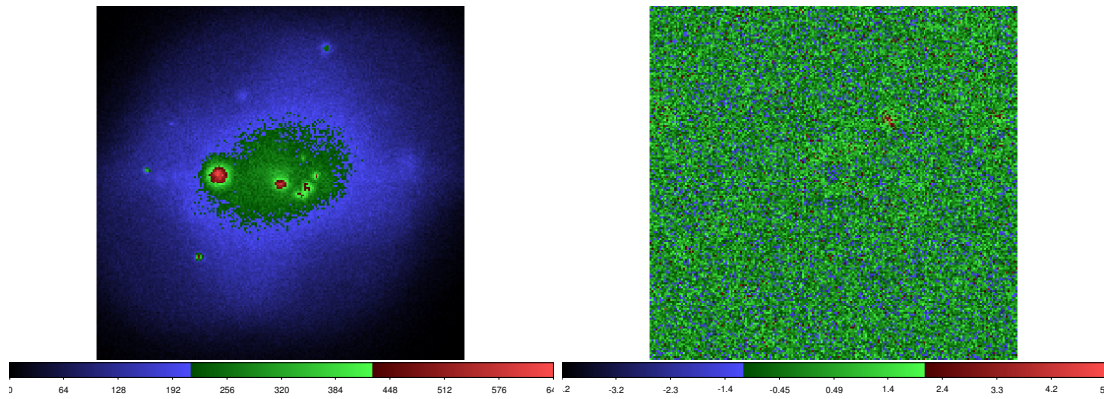


Figure 3.10: The upper part shows the sky map (left) and residual map (right) of **W28**, obtained by subtracting the model map from the count map. These maps include HESS J1800–240A, HESS J1800–240B and HESS J1800–240C also in the FoV. The lower panel shows the residual spectrum of W28. The residual values locate between -4σ and 4σ . There is a significant difference between the simulated prefactor and the reconstructed prefactor of W 28, as seen in Table 3.3.

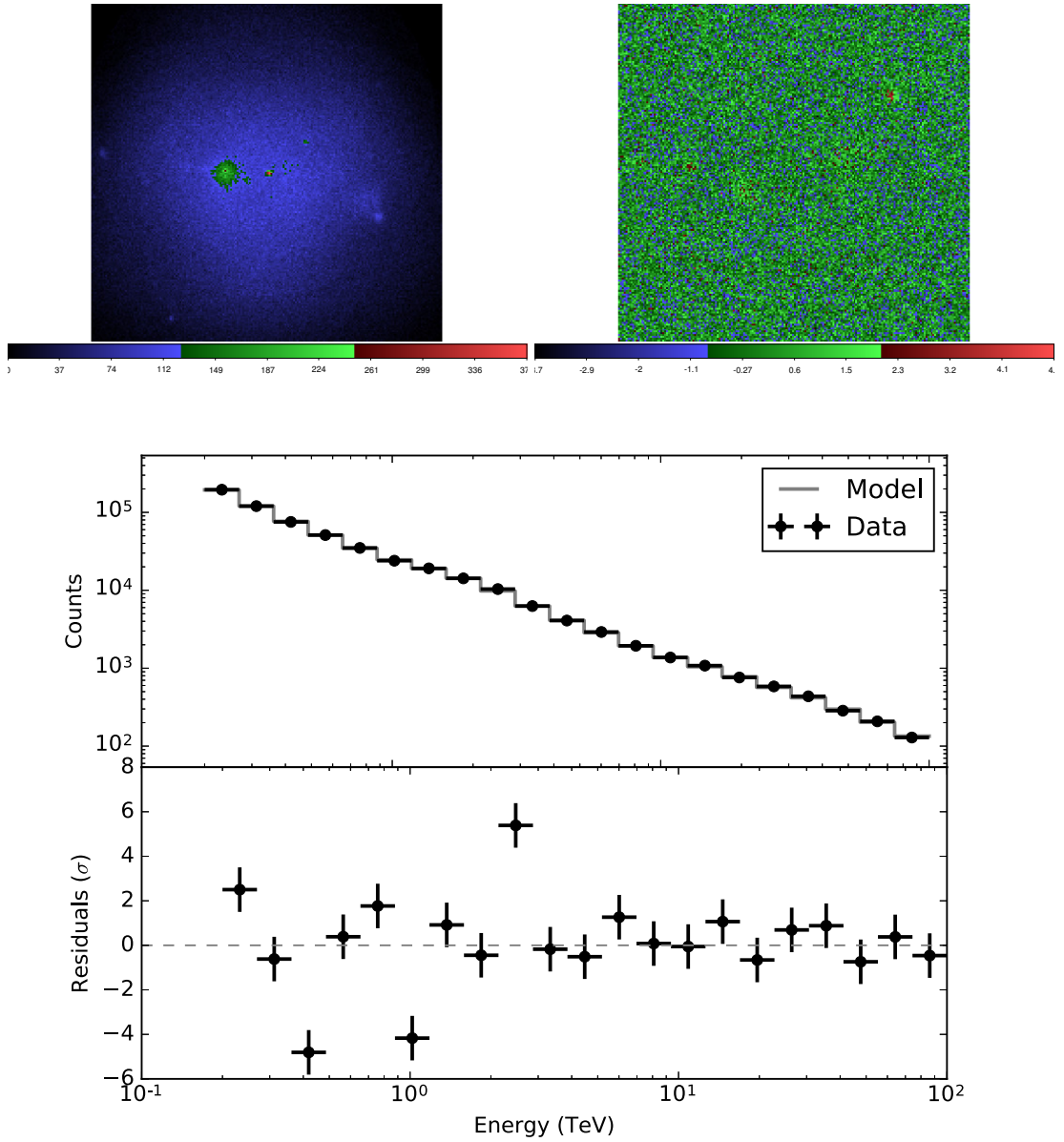


Figure 3.11: The upper part shows the sky map (left) and residual map (right) of **W49B**, obtained by subtracting the model map from the count map. These maps include HESS J1912+101 also in the FoV. The lower panel shows the residual spectrum of W49B. The residual values locate between -4σ and 4σ . Since there are some reconstruction problems between 100 GeV and 200 GeV, we use 200 GeV as the minimum energy value.

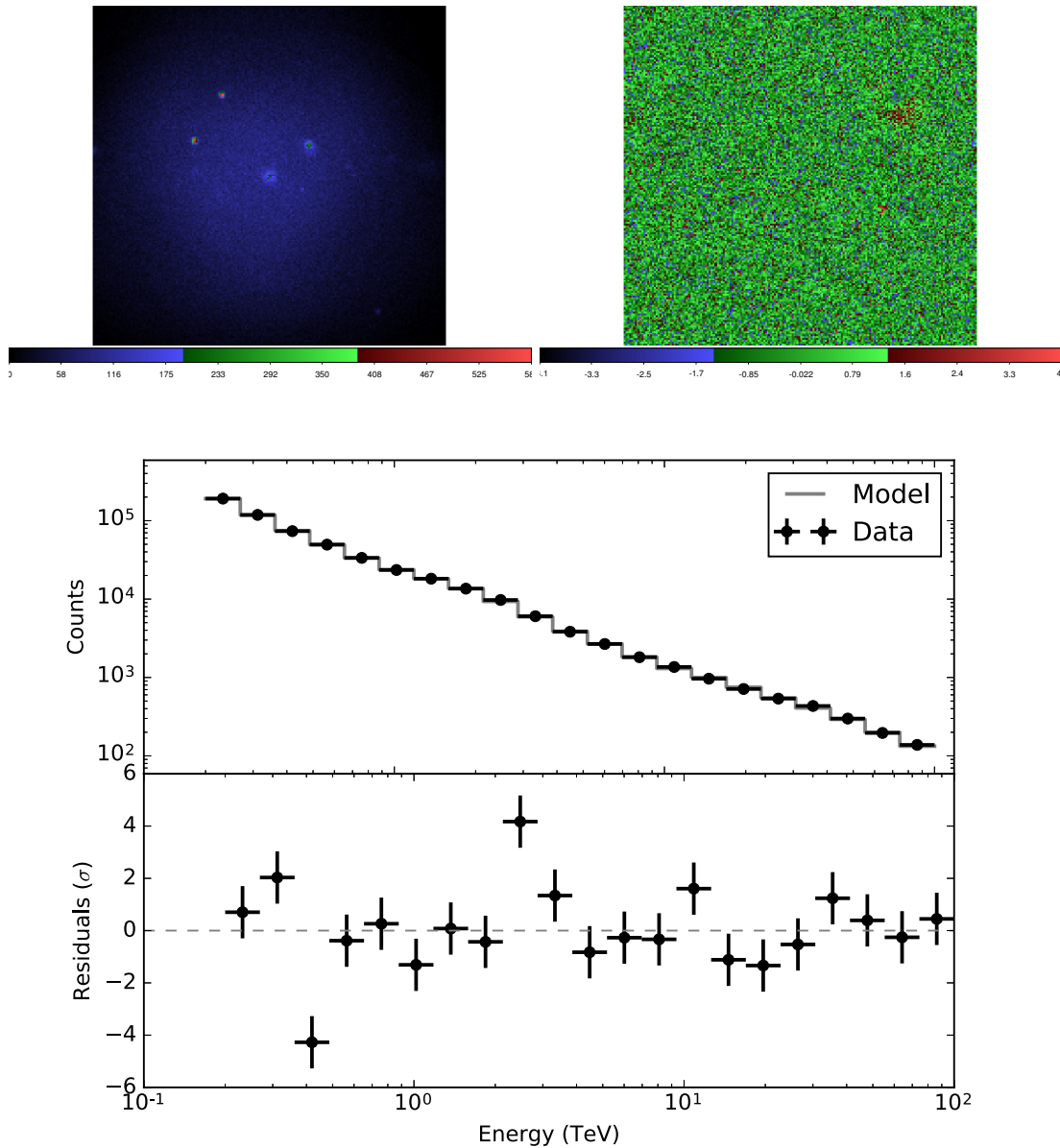


Figure 3.12: The upper part shows the sky map (left) and residual map (right) of **W51C**, obtained by subtracting the model map from the count map. The lower panel shows the residual spectrum of **W51C**. The lower panel shows the model, the data and the residual values of **W51C**. Its residual values locate between -5σ and 5σ . Since there are some reconstruction problems between 100 GeV and 200 GeV, we use 200 GeV as the minimum energy value.

source	north [h]	south [h]
HESS J1614–518	0	1409.8
RX J1713.7–3946	0	1836.5
HESS J1731–347	0	1891.0
HESS J1745–303	0	1903.0
HESS J1800–240A	0	1874.8
HESS J1912+101	1542.0	196.2
W 28	0	1869.0
W 49B	1504.3	455.7
W 51C	1674.5	0

Table 3.4: Visibility for northern and southern CTA sites of selected candidates over a one year period.

3.4 Conclusion

To study Galactic SNRs, we have analyzed simulated DC-1 data. We have selected shell-type SNRs, SNR-MC and composite SNRs from TeVCat. 9 potential candidates were simulated in the DC-1 GPS data. The SEDs of these sources were reconstructed by using *ctools* for data analysis. We have discussed the main steps involved in a *ctools* analysis and shown the results obtained for each FoV. The reconstructed parameters are overall in good agreement with parameters used in DC-1 simulation. It should be noted nonetheless that significant residuals are sometimes found, particularly in the reconstructed spectrum at low energies. Although the origin of these residuals was not identified, one could infer that the simple approach (spatial model and spectral model) used in the modeling of the FoV could be at fault. Low intensity sources can sometimes be suspected in the residual map of FoV, which, if soft enough, could play a role at low energies. Given that we are mostly interested in the high-energy tail of the spectra, the approach used in this work is deemed sufficient to explore the capabilities of CTA and the performance and simulation of DC-1.

SNR's SED and CTA Sensitivity

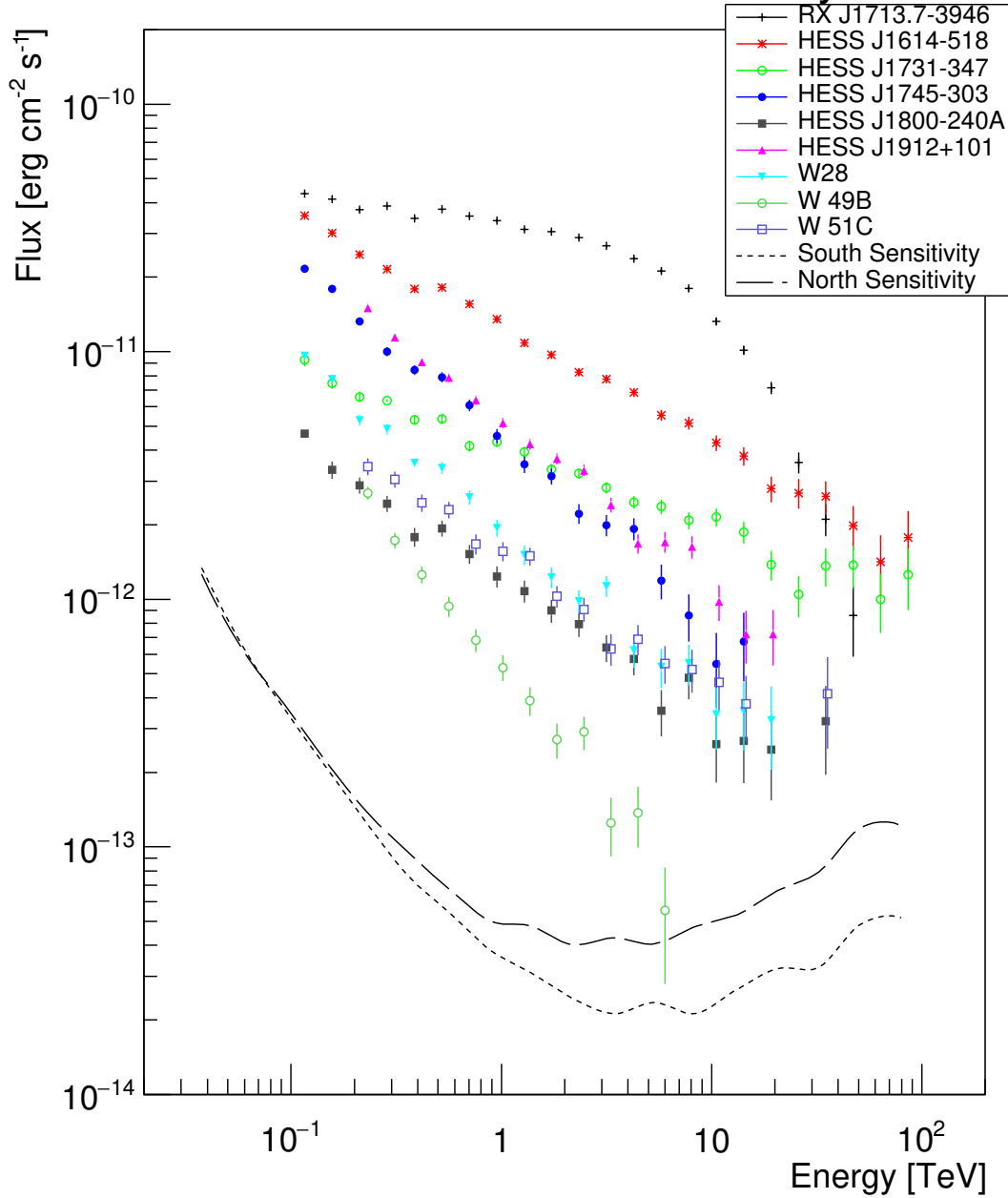


Figure 3.13: SED of SNRs and the sensitivity of CTA. The X axis is the energy which covers the CTA energy range. The Y axis is the differential flux. The differential sensitivity curve are obtained with the *cssens* tool. The spectra are obtained from the analysis described in Sec. 3.3.2

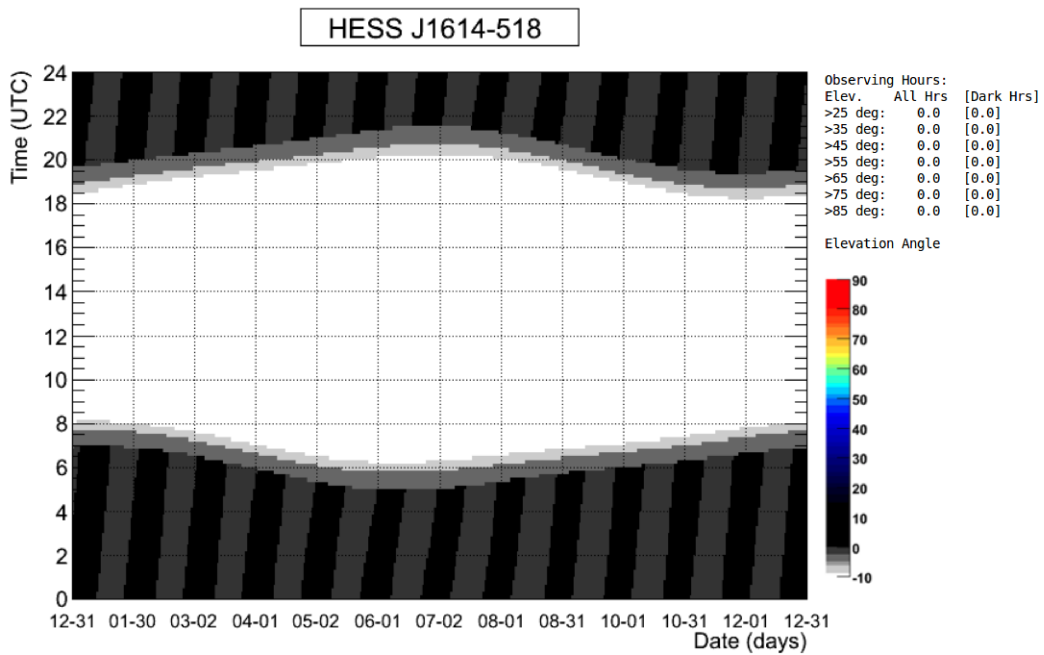
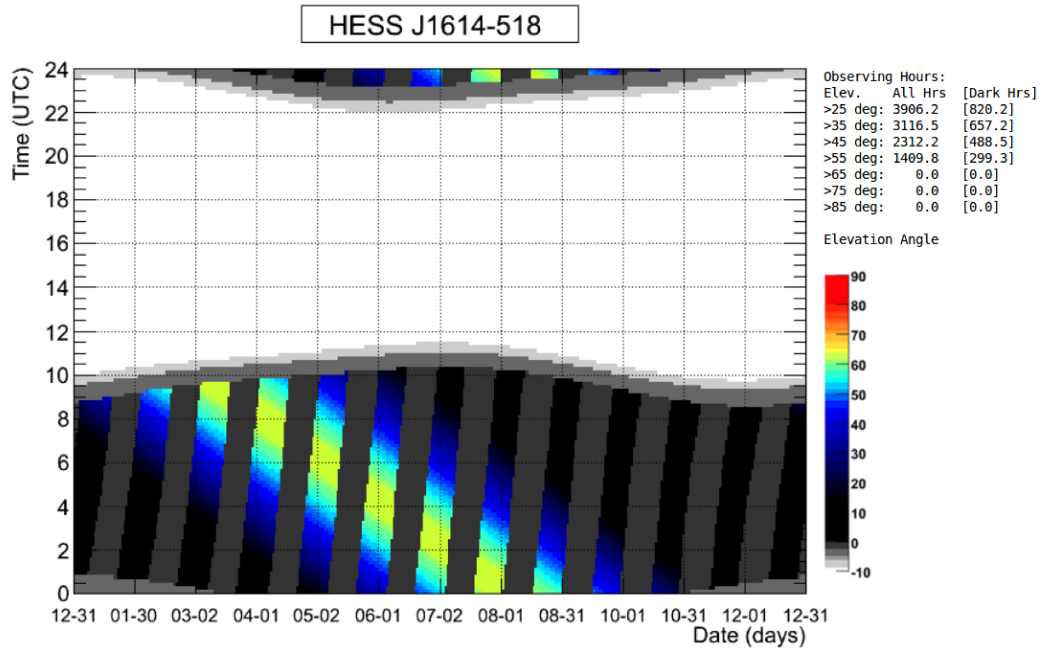


Figure 3.14: CTA south (upper panel) and north (lower panel) site's visibility of HESS J1614–518. The corresponding time covers the year 2019. The X axis shows the days of the year, and the Y axis corresponds to 24 h for each day. The color bar scale corresponds to different elevation angles.

Chapter 4

Comparison to Radiative Models

After having analyzed the simulated DC-1 data, we use multi-wavelength data to construct the broad-band SED of selected Galactic PeVatron candidates. After this, we fit lepto-hadronic model, pure leptonic model, and pure hadronic models to MWL data. By comparing different radiative models, we determine whether leptonic or hadronic processes dominate the emission of the selected Galactic SNRs. For the model calculation and fit to SEDs, the *Naima* package is used. The proton cutoff energy is the key parameter to judge whether a SNR is a promising PeVatron candidate (i.e. when proton cutoff energy of a source is above 1 PeV, it means protons can be accelerated up to PeV energies by this source, which shows this source is a PeVatron candidate.). In this chapter, we describe different radiative models, the fitting algorithm and the *Naima* code [117]. We show the MWL results for the sources and discuss the results obtained, and illustrate how to use DC-1 data, combined with data from other wavelengths, to constrain such radiative models.

4.1 Radiative Models

Three potential radiative mechanisms are proposed for GeV to TeV γ -ray emission for SNRs: high-energy electron scattering on photons which is called Inverse Compton (IC) scattering [83]; bremsstrahlung from the interaction between relativistic electrons and ions [10]; proton-proton (PP) collisions which result in pion production and consequent γ -ray decay [79]. Furthermore, synchrotron radiation [9] can be used to fit the photon spectrum at lower energies (radio and X-ray) to constrain the magnetic field and electron spectrum. The observations and simulations of X-ray data for SNRs support that there is a potential thermal component, both a continuous and emission lines [59, 63, 81, 109]. However, we do not consider thermal component in the model fitting.

The different radiative models illustrate the interaction between particles and the environment (magnetic field, photon fields, particles). The particle radiates non-thermal emission, which means that the continuum radiation generated from the particle distribution is a non-Maxwellian

energy spectrum. The following description of radiative processes are mainly from Ref. [7, 90]. We focus the discussion on the energy loss, the cross-section, and the cooling time.

4.1.1 Bremsstrahlung

The interaction between relativistic charged particles and the electrostatic field of free nuclei induces non-thermal bremsstrahlung radiation. Such radiation from electron-ion system become important above 10 MeV. Electron distributions with power-law spectra produce bremsstrahlung power-law spectra with the same spectral index.

The total energy loss of thermal bremsstrahlung radiation is:

$$-\left(\frac{dE}{dt}\right)_{\text{bre}} \propto Z^2 T^{1/2} \bar{g} N N_e, \quad (4.1)$$

where Z is the atomic number of the matter, T is the temperature, \bar{g} is the average value of the Gaunt factor¹, N is the space density of nuclei in the source frame, N_e is the electron density.

The lifetime of electrons due to the bremsstrahlung losses is:

$$t_{\text{br}} = \frac{E}{(-dE/dt)_{\text{bre}}} \simeq 4 \times 10^7 (N/1 \text{ cm}^{-3})^{-1} \text{ yr}. \quad (4.2)$$

4.1.2 Compton and Inverse Compton Scattering

Thomson scattering describes interactions between low-energy photons and stationary electrons, with $\hbar\omega \ll m_e c^2$. The cross-section of Thomson scattering is:

$$\sigma_{\text{T}} = \frac{e^4}{6\pi\epsilon_0^2 m_e^2 c^4} = 6.653 \times 10^{-29} \text{ m}^2, \quad (4.3)$$

where e is the charge of electron.

The optical depth of the medium for Thomson scattering is:

$$\tau_{\text{T}} = \int \sigma_{\text{T}} N_e \text{ dx}. \quad (4.4)$$

Therefore, we get the mean free path $\lambda_{\text{T}} = (\sigma_{\text{T}} N_e)^{-1}$.

When high-energy photons collide with electrons, some of the energy and momentum from photons transfers to the electrons. This process is called Compton scattering. The main difference between Compton scattering and Thomson scattering is that a frequency change of the radiation matters for Compton scattering.

The cross-section for Compton scattering associated with the collision between electrons and

¹The Gaunt factor is a multiplicative correction to the continuous absorption or emission which describes the deviation from the classical theory [68].

photons is given by the Klein-Nishina formula. In the ultra-relativistic limit ($x \gg 1$), it is:

$$\sigma_{\text{K-N}} = \pi r_e^2 \frac{1}{x} \left(\ln 2x + \frac{1}{2} \right), \quad (4.5)$$

where r_e is the classical electron radius, and $x = \hbar\omega/m_e c^2$. For low-energy photons ($x \ll 1$), we have $\sigma_{\text{K-N}} = \sigma_{\text{T}}$, which means the Klein-Nishina cross-section reduces to the classical Thomson scattering cross-section.

Inverse-Compton scattering is the ‘inverse’ process of Compton scattering, which means that low-energy photons gain energy from relativistic electrons [18, 8, 83]. It proceeds with high efficiency for GeV-TeV γ -rays. The CMB and ISM radiation fields in visible light and infrared band are the most important target fields.

For a power-law distribution of electrons, $dN_e/d\epsilon_e \propto \epsilon_e^{-\Gamma}$, the resulting γ -ray spectrum in the non-relativistic regime has a power-law form with photon index $\alpha = (\Gamma + 1)/2$. In the ultra-relativistic regime it has $\alpha = (\Gamma + 1)$.

The total energy loss rate is:

$$-\left(\frac{dE}{dt}\right)_{\text{IC}} = \frac{4}{3} \sigma_{\text{T}} c U_{\text{rad}} \left(\frac{v}{c}\right)^2 \gamma^2, \quad (4.6)$$

where the radiation energy density U_{rad} is expressed in units of eV cm^{-3} , and γ is the Lorentz factor of the electron.

The cooling time of electrons is:

$$t_{\text{IC}} \approx 3 \times 10^8 \times (U_{\text{rad}}/1 \text{ eV cm}^{-3})^{-1} (E/1 \text{ GeV})^{-1} \text{ yr}, \quad (4.7)$$

where E is the electron energy.

4.1.3 Synchrotron Radiation

Accelerated high-energy electrons in magnetic fields can produce synchrotron radiation. The total synchrotron loss rate is:

$$-\left(\frac{dE}{dt}\right)_{\text{sync}} = 2\sigma_{\text{T}} c U_{\text{mag}} \left(\frac{v}{c}\right)^2 \gamma^2 \sin^2\theta, \quad (4.8)$$

where $U_{\text{mag}} = B^2/2\mu_0$ is the energy density of the magnetic field, μ_0 is the permeability of free space. Therefore, the stronger the magnetic field, the stronger the emitted radiation.

In the synchrotron self-Compton (SSC) case, the relativistic electrons which are the source of low-energy photons are also responsible for scattering these photons up to X-ray and γ -ray energies. The ratio η of the rates of energy loss of an ultra-relativistic electron by synchrotron

and inverse-Compton radiation is given by:

$$\eta = \frac{(dE/dt)_{\text{IC}}}{(dE/dt)_{\text{sync}}} = \frac{U_{\text{rad}}}{B^2/2\mu_0}. \quad (4.9)$$

Whether the photon spectrum is dominated by synchrotron and inverse Compton or bremsstrahlung depends on the ratio of energy of the radiation and magnetic field to the number density of the ambient gas.

4.1.4 Pion-decay

The pion-decay (PI) process provides the hadronic component of γ -ray emission. Relativistic protons produce GeV to TeV γ -rays in inelastic collisions with ambient gas due to the production and decay of secondary pions [79, 80, 82]. These neutral pions produce high energy γ -rays from conversion of the kinetic energy of protons, that is $pp \rightarrow pp + \pi^0 \rightarrow pp + 2\gamma$. The kinetic energy of protons should exceed $E_{\text{th}} = 2m_{\pi}c^2(1 + m_{\pi}/4m_p) = 280 \text{ MeV}$, where $m_{\pi} = 134.97 \text{ MeV}$ is the mass of π^0 -meson. The γ -ray spectrum from pion-decay has a peak at $E_{\gamma} = m_{\pi}c^2/2 = 67.5 \text{ MeV}$ in the centre of mass. Such γ -ray spectra should follow the spectrum of the parent protons, which means these γ -rays carry information from the acceleration spectrum of protons. Detection of pion-decay from SNRs provide proof of the acceleration of protons by SNR shocks.

The cooling time of PI is:

$$t_{\text{PI}} \simeq 5.3 \times 10^7 (N/1 \text{ cm}^{-3})^{-1} \text{ yr}, \quad (4.10)$$

where N is the proton density.

4.2 Maximum Likelihood, Monte Carlo Markov Chain and Naima

4.2.1 Model Fitting with Naima

We fit MWL data with synchrotron radiation [9], IC scattering [83] and PI process [79]. For this, we use the Naima python package [117], which is developed for the analysis of non-thermal radiation from relativistic particle populations. Naima² is a package for Markov Chain Monte Carlo (MCMC) fitting of different particle distributions and radiative models.

The MCMC sampling of the likelihood distributions is used to derive the posterior distributions of spectral model parameters. A prior is used in Bayesian inference to constrain some

²<https://github.com/zblz/naima>

hypotheses (e.g. parameter values) before having observed any data. The likelihood is expressed as:

$$L = \prod_{i=1}^N \frac{1}{\sqrt{2\pi\sigma_i^2}} \exp\left(-\frac{(S(\vec{p}; E_i) - F_i)^2}{2\sigma_i^2}\right), \quad (4.11)$$

where E_i is the energy value for each bin, F_i and σ_i are the measured flux and uncertainty for each E_i . It is useful to define the objective function as the log-likelihood disregarding constant factors:

$$\ln L = -\sum_{i=1}^N \frac{(S(\vec{p}; E_i) - F_i)^2}{2\sigma_i^2}. \quad (4.12)$$

The $\ln L$ function in this assumption can be related to χ^2 as $\chi^2 = -2 \ln L$, so the maximization of the log-likelihood is equivalent to a minimization of χ^2 . In addition, a prior likelihood factor should be considered for all parameters. A normal distribution is used in the case where a given parameter is constrained by a previous measurement, while a uniform prior is used for constraining a parameter to be within a certain range. Here, we use uniform or log-uniform priors for all parameters.

A posterior is used in Bayesian inference to constrain some hypotheses after having accumulated for data. In Bayes theory, the relationship between a prior and a posterior is:

$$p(\mu|D) \propto p(D|\mu) \cdot p(\mu) \quad (4.13)$$

where μ indicates a (set of) parameter(s) of interest and D indicates the data; $p(\mu|D)$ indicates the posterior or the probability of μ given the data; $p(D|\mu)$ indicates the likelihood or the probability of the data given μ ; $p(\mu)$ indicates the prior probability of μ .

4.2.2 Radiative Model Parameters

We use the Exponential Cutoff Power Law (ECPL) function for electron and proton distributions:

$$f(E) = A(E/E_0)^{-\alpha} \exp(-E/E_{\text{cut}}), \quad (4.14)$$

where E_0 is the reference energy (default value as 1 TeV). We assume an ECPL for both electron and proton distributions.³

The ratio of the electron amplitude to the proton amplitude is introduced as $K_{\text{ep}} = A_{\text{e}}/A_{\text{p}}$. This parameter indicates the importance of leptonic and hadronic components. Therefore, the electron distribution can be re-written as:

$$f(E) = K_{\text{ep}} A_{\text{p}} (E/E_0)^{-\alpha_{\text{e}}} \exp(-E/E_{\text{cut,e}}). \quad (4.15)$$

³e.g. The X-ray observation of RX J1713.7–3946 clearly reveals a spectral cutoff which is linked to the maximum energy of parent electrons [105]

IC and PI are the two dominant processes for high-energy γ -rays emitted by SNRs. Therefore, two important parameters are introduced: B is the magnetic field, which impacts synchrotron radiation and IC; N_H is the number density of target protons, which impacts pion-decay. In total, we have eight parameters in the fit:

- A_p , the amplitude of the proton distribution,
- α_e , the power law index of the electron distribution,
- α_p , the power law index of the proton distribution,
- $E_{\text{cut},e}$, the cutoff energy of the electron distribution,
- $E_{\text{cut},p}$, the cutoff energy of the proton distribution,
- B , the magnetic field,
- K_{ep} , the ratio of the electron and proton amplitude,
- N_H , the number density of the target protons.

In the analysis, we divide the sources into three groups:

1. sources with X-ray, *Fermi*-LAT and DC-1 data, including RX J1713.7–3946, HESS J1731–347 and W 49B, for which both the synchrotron and high-energy components of the model are constrained;
2. sources with *Fermi*-LAT data and DC-1 data, including HESS J1745–303, W 28, W 51C and HESS J1800–240A, for which only the high-energy component is constrained;
3. sources with DC-1 data, including HESS J1614–518 and HESS J1912+101.

For each group, we have different approach to performance the fit:

- For group (1), we fit the data with hybrid lepto-hadronic model (IC and PI), with eight free parameters.
- For group (2), we follow the same approach as what we do for group (1), except that we freeze the parameters related to leptonic processes and fit the other parameters.
- For group (3), we fit with a purely leptonic model and a purely hadronic model separately.

SNR name	X-ray	GeV	TeV
RX J1713.7–3946	(a)	(d)	(k)
HESS J1614–518			
HESS J1731–347	(b)	(e)	(l)
HESS J1912+101			(m)
HESS J1745–303		(f)	(n)
HESS J1800–240A		(g)	(o)
W 28		(h)	(p)
W 49B	(c)	(i)	(q)
W 51C		(j)	

Table 4.1: References for multi-wavelength data.(a): [105], (b): [58], (c): [106], (d): [61], (e): [50], (f): [78], (g): [52], (h): [43], (i): [44], (j): [60], (k), (l): [35], (m): [34], (n): [33], (o): [32], (p): [32], (q): [75]

4.3 Multi-wavelength Analysis Results

We list all the references of multi-wavelength spectra of the studied PeVatron candidates in Table 4.1. Real data from H.E.S.S. are also shown for comparison with DC-1 in some cases. Eight free parameters are used to fit the data. We use 50 steps for *walkers*, 50 steps for *burn* and 50 steps for *run*. *walkers* are the number of ensemble points, i.e. the number of independent chains in the MCMC analysis. It must be at least twice the number of fitting parameters (larger than 16). The walkers start in small distributions around the maximum likelihood values and then they quickly wander and start exploring the full posterior distribution. *burn* is the number of iterations that are walked away from the starting points of each chain (‘burn-in’). It is intended to give the Markov Chain time to reach its equilibrium distribution. If it has started from an unreasonable point, it may over-sample regions that are actually of very low probability. *run* is the number of steps to take to sample the posterior distribution for each chain. The initial values and range of prior are listed in table. 4.2. We use uniform or log-uniform priors for the parameters, consistent with approaches followed the examples for *Naima*.⁴

We use the PI model analysis for RX J1713.7–3946 with H.E.S.S. data as example.⁵ Some diagnostic plots of the sampler chains for checking whether the results are fine are generated, which include the chain plot and the corner plot.

Fig. 4.1, Fig. 4.2 and Fig. 4.3 are the chain plots for the parameters (proton amplitude, proton index, and proton cutoff energy) obtained from the fit of a lepto-hadronic model (leptonic parameters are freeze) to the SED of RX J1713.7–3946. For each of them, the top-left panel shows the relationship between the parameter values and step numbers (*run*). The number of lines in the plot is the number of *walkers*. The right handside plot shows the posterior distribution of this parameter. The dashed line is the median value, and the grey region is the uncertainty at

⁴<https://naima.readthedocs.io/en/latest/examples.html>

⁵Although RX J1713.7–3946 is in the group (1), leptonic parameters are frozen on this example.

parameter	units	initial value	prior range
$\log A_p$	TeV^{-1}	2.0	[-1, 5]
α_e		2.0	[0, 3]
α_p		2.0	[0, 3]
$\log E_{\text{cut},e}$	TeV	1.0	[-1, 4]
$\log E_{\text{cut},p}$	TeV	1.0	[-1, 4]
B	μG	20	[0, 100]
K_{ep}		0.02	[0.0001, 1]
N_{H}		0.01	[0.0001, 100]

Table 4.2: Table of the eight parameters used for the fitting. Initial values and prior range are also given.

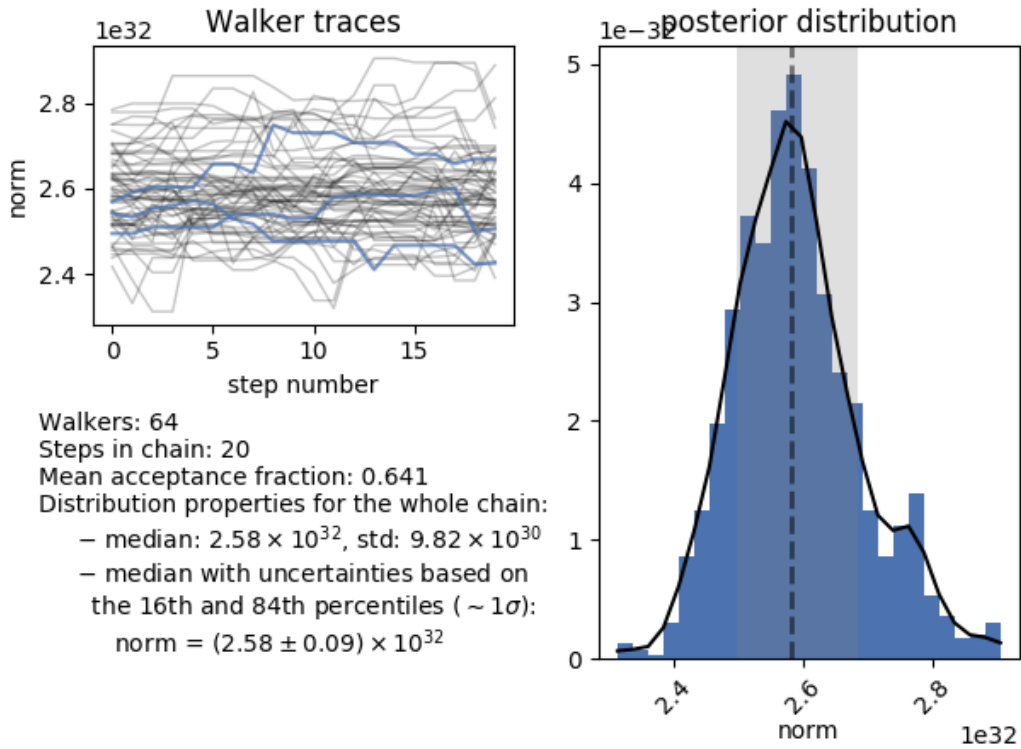


Figure 4.1: Diagnostic plot for the amplitude of the proton distribution of RX J1713.7–3946.

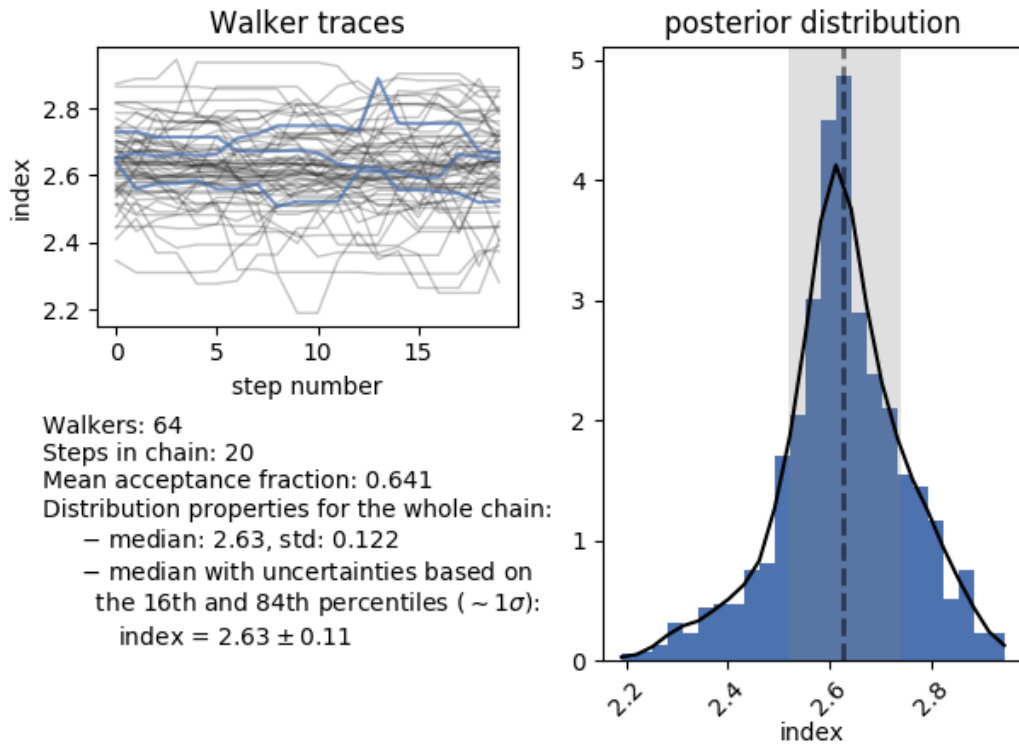


Figure 4.2: Diagnostic plot for the index of the proton distribution of RX J1713.7–3946.

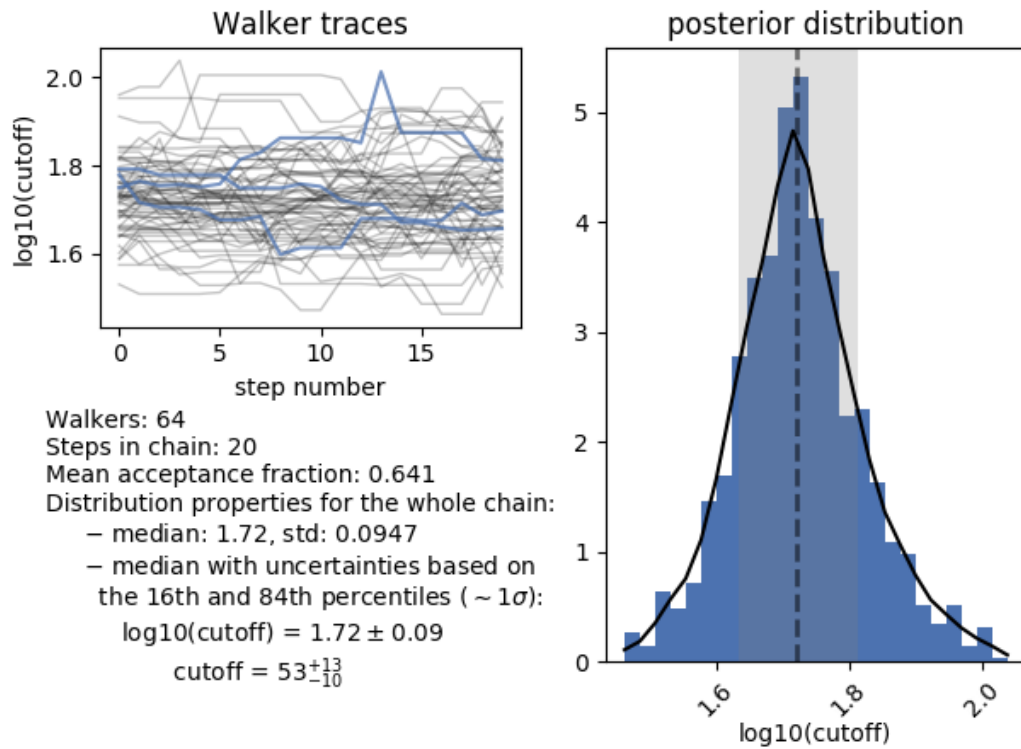


Figure 4.3: Diagnostic plot for the cutoff energy of the proton distribution of RX J1713.7–3946.

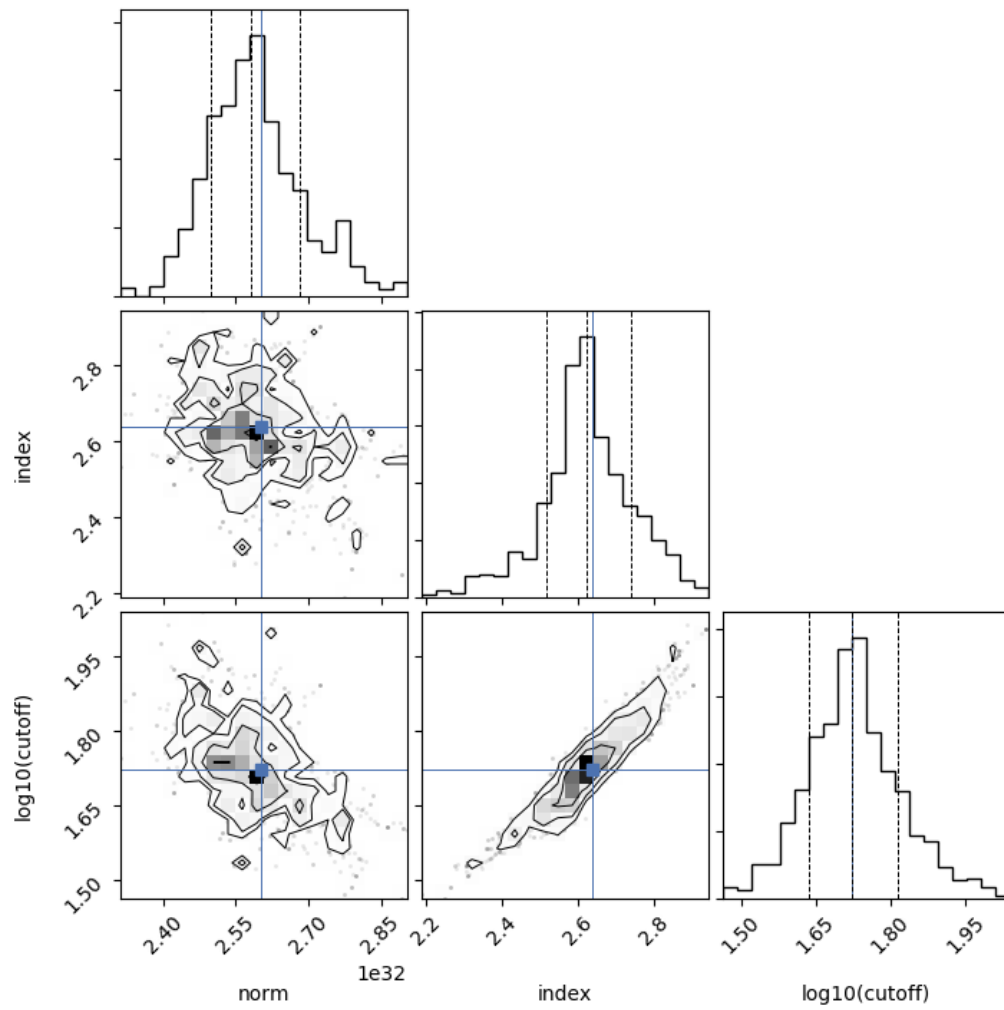


Figure 4.4: Corner plot for the amplitude, the power index, and the cutoff energy of the proton distribution of RX J1713.7–3946.

the 1σ CL. The bottom left text shows the number of *walkers*, *run*, the mean acceptance fraction, the median value and the uncertainty. The mean acceptance fraction of the ensemble is a good indicator of whether or not the sampling went well [65]. If the acceptance fraction is getting very low (lower than 0.25), the chain is not working in normal conditions.

From Fig. 4.1, Fig. 4.2, and Fig. 4.3 we can see that the walkers behave well since the lines in each left plot do not show a specific trend and are equally distributed around the median. The distribution of these three parameters in each right handside plot follows a roughly Gaussian distribution with a tail on the right side.

A corner plot shows the one and two dimensional projections of the posterior probability distributions of the free parameters. It quickly demonstrates all of the covariances between parameters. The corner plot shows the marginalized distribution independently for each parameter in the histograms along the diagonal and then the marginalized two dimensional distributions in the other panels.

Fig. 4.4 shows the corresponding corner plot for the parameters. The one dimensional distribution for each parameter is the same as the right handside plots in Fig. 4.1, Fig. 4.2, and Fig. 4.3. The crossing of the horizontal line and the vertical line in the $\log_{10}(norm) - p_\alpha$ plot gives the median value of these two parameters. The contours are the uncertainty at 1σ , 2σ and 3σ . The dashed lines in each one dimensional distribution plot show the 16%, 50%, and 84% quantiles. All the four plots illustrate the fit is good.

4.3.1 Group (1): With X-ray, *Fermi*-LAT and DC-1 Data

4.3.1.1 RX J1713.7-3946

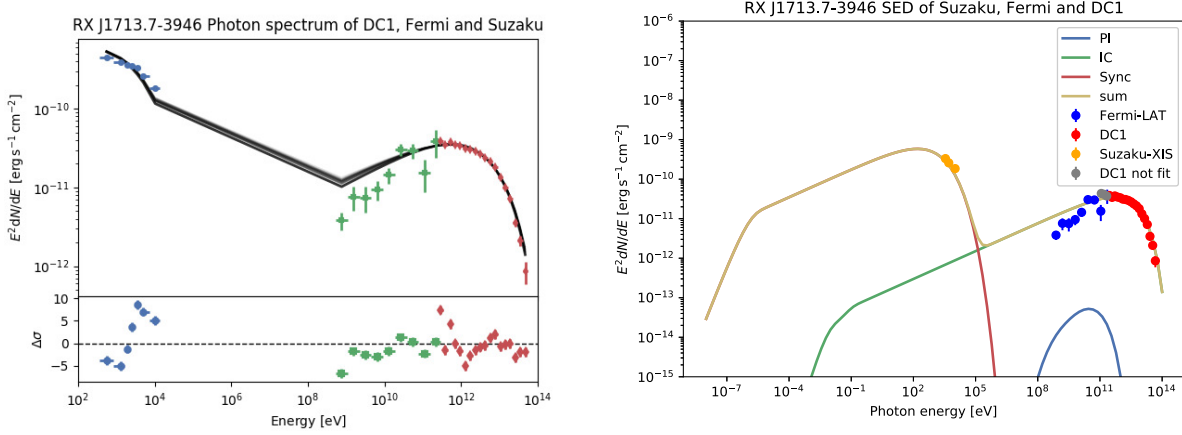


Figure 4.5: Multi-wavelength fitting results of RX J1713.7–3946 with eight free parameters. Left: the fitting results of MWL photon spectrum with residuals in the bottom. Right: Corresponding best-fit SED with radiative models. Red points, grey points, blue points and orange points are DC-1 data included in the fit, DC-1 data not included in the fit, *Fermi*-LAT data, and *Suzaku*-XIS data respectively. For showing the SED clearly, we reduce the number of X-ray data in the right plot. Same for other sources in group (1).

In this analysis, in addition to the DC-1 data, GeV data from *Fermi*-LAT [61] and X-ray data from *Suzaku*-XIS [105] are used together with DC-1 data. The X-ray data can be described by a power-law with photon index around 3. The left panel of Fig. 4.5 shows the fitting results of MWL data from RX J1713.7–3946. There is a small discrepancy in the lower energy part of *Fermi*-LAT data, which will be discussed in section 4.5. The right panel of Fig. 4.5 shows the SED from Naima fitting. Since the lower energy part of DC-1 data overlap with *Fermi*-LAT data, we do not fit this part. Inverse Compton dominates over proton-proton interaction. The proton cutoff energy $\log_{10} E_{\text{cut,p}} [\text{TeV}] = -0.21 \pm 0.05$. The K_{ep} is 0.056 ± 0.006 , which is close to a leptonic case (see table 4.3).

The CTA collaboration uses $K_{\text{ep}} = 0.01$ and $K_{\text{ep}} = 100$ to model RX J1713.7–3946 in Ref. [51] for leptonic and hadronic situations, respectively. The combined *Suzaku*-XIS and H.E.S.S. data can be hardly explained by a pure leptonic model [105]. It requires a weak magnetic field strength that is inconsistent with the short-term variability behavior and the X-ray filamentary. The leptonic models require magnetic fields to be $10 - 15 \mu\text{G}$. An alternative approach to explaining the TeV γ -ray spectrum within IC component can be realized by assuming the existence of an additional low-energy electron population in the shell of SNRs. Therefore, although RX J1713.7–3946 does not have thermal X-ray emissions, the pure hadronic scenario with strong magnetic fields ($100 - 200 \mu\text{G}$) is more reasonable.

4.3.1.2 HESS J1731-347

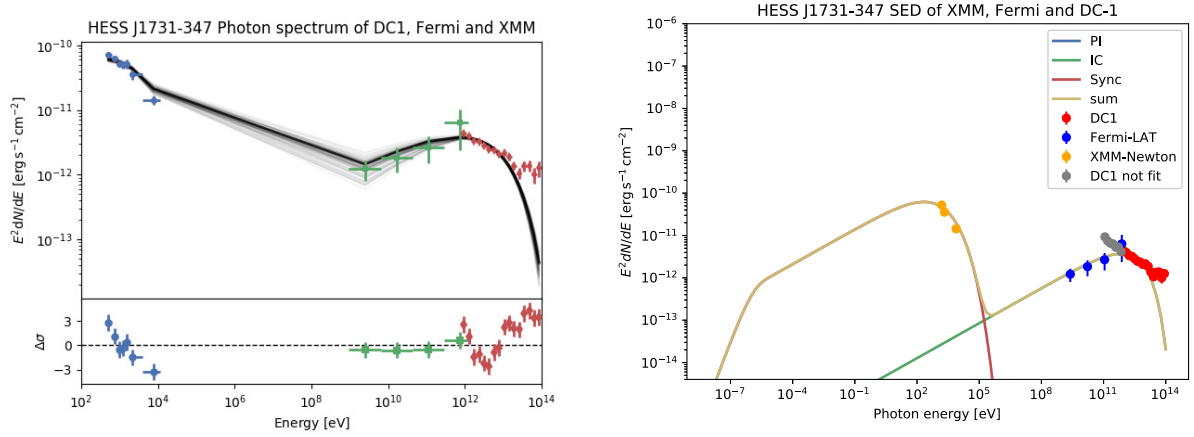


Figure 4.6: Multi-wavelength fitting results of HESS J1731–347 with eight free parameters. Left: the fitting results of MWL photon spectrum with residuals in the bottom. Right: Corresponding best-fit SED with radiative models. Red points, grey points, blue points and orange points are DC-1 data included in the fit, DC-1 data not included in the fit (see the text), *Fermi*-LAT data, and *XMM-Newton* data respectively.

GeV data from *Fermi*-LAT [50] and X-ray data from *XMM-Newton* [58] are used together with DC-1 data. The left panel of Fig. 4.6 shows the fitting results of multi-wavelength data from HESS J1731–347. There is a small discrepancy between the model and simulated data in the high energy part of DC-1 data. The right panel of Fig. 4.6 shows the SED from Naima fitting. Since the lower energy part of DC-1 data overlaps with *Fermi*-LAT data, we do not fit this part. Inverse Compton dominates proton-proton interaction. The proton cutoff energy $\log_{10} E_{\text{cut,p}} [\text{TeV}] = 0.12 \pm 0.08$.

Ref. [71] shows that either a hadro-leptonic or a pure leptonic model can fit the MWL SED of HESS J1731–347, in which the proton cutoff in hadro-leptonic model is 10 – 38 TeV. While in another research, by freezing the electron and proton index, and the particle number density, HESS J1731–347 gets a proton cutoff at 100 TeV in the pure hadronic model [35]. However, the high medium density required to reproduce the observed TeV flux is not consistent with the hydrodynamics of the SNR.

The SED in Ref. [58] is obtained by assuming X-ray flux integrated over the entire SNR, and an one zone synchrotron-self Compton (SSC) model. However, this is probably an oversimplification as X-ray emission shows variation of intensity and power-law slope. The results of electron index (1.85), electron cut-off (11.2 TeV), and magnetic field (23 μG) are similar to Ref. [115]. Notice that the eastern part is considerably brighter than the western part in the X-ray band. Ref. [50] reports that the index obtained from *Fermi*-LAT ($\Gamma \sim 1.66$) and the connection with the TeV data support the association between the TeV shell and the GeV source [50, 71]. Ref. [58] gives the shape and the size in X-ray from *XMM-Newton* that are compatible with H.E.S.S. data.

4.3.1.3 W 49B

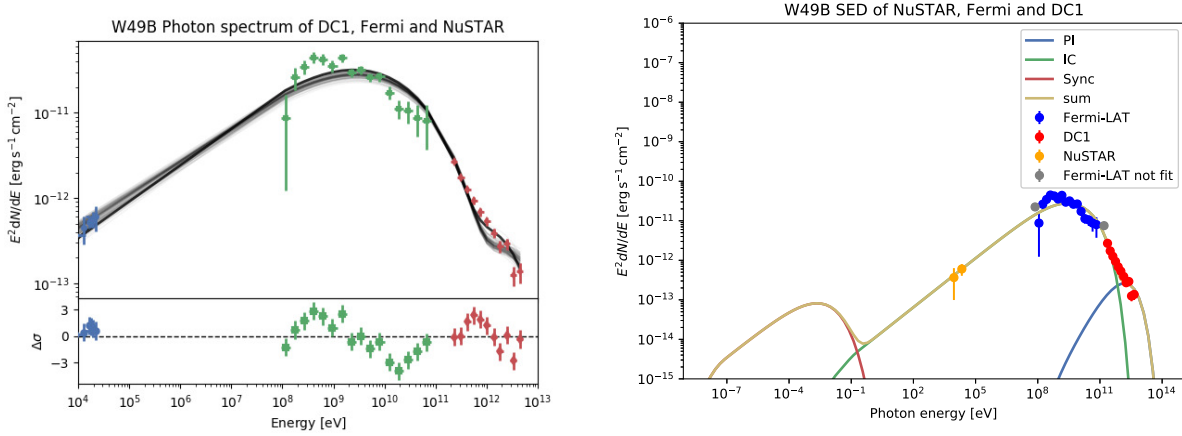


Figure 4.7: Multi-wavelength fitting results of W 49B with eight free parameters. Left: the fitting results of MWL photon spectrum with residuals in the bottom. Right: Corresponding best-fit SED with radiative models. Red points, grey points, blue points and orange points are DC-1 data fit in the program, DC-1 data not fit in the program, *Fermi*-LAT data, and *NuSTAR* data respectively.

GeV data from *Fermi*-LAT [75] and X-ray data from *NuSTAR* [106] are used for W 49B. The left panel of Fig. 4.7 shows the fitting results of multi-wavelength data from W 49B. Similarly to HESS J1731–347, there is a small discrepancy in the lower energy part of *Fermi*-LAT data. The right panel of Fig. 4.7 shows the SED from Naima fitting. Note that the upper limits are not included in the fit. Inverse Compton dominates at low energies while proton-proton interaction dominates at high energies. The proton cutoff energy $\log_{10} E_{\text{cut,p}} [\text{TeV}] = 1.02 \pm 0.09$.

Ref. [75] reports that the best-fit position of W 49B obtained with the *Fermi*-LAT is coincident with its radio shell. However, the fitted position in the TeV range is more compatible with its center. In addition, the size of the shell detected at radio wavelengths is comparable to the size at TeV energies (H.E.S.S.). The *Fermi*-LAT spectrum of W 49B can be explained either by the PI process or by electron bremsstrahlung [44]. Two spectral breaks are found in the γ -ray spectrum: one at 304 MeV and the other at 8.4 GeV. Below 300 MeV, the spectrum is rising steeply. The first break can be explained as PI process. The MWL SED fitting from H.E.S.S. Collaboration suggests that the γ -ray emissions of W 49B are probably dominated by PI component which is similar to several other SNR-MC systems [75].

4.3.1.4 Conclusions for group (1)

Based on the simulated CTA data and data from other wavelengths, RX J1713.7–3946, HESS J1731–347, and W 49B would not be promising PeVatron candidates according to the proton cutoff energy. W 49B is the only source with a significant hadronic component. As a caveat, we note that DC-1 data only include a simple power-law extrapolation of current observations.

4.3.2 Group (2): With *Fermi*-LAT and DC-1 Data

Since group (2) sources have DC-1 data and *Fermi*-LAT data only, we use two different methods to analyze them. On one hand, we perform the same analysis as for group (1), on the other hand, we freeze the parameters related to leptonic model to get the fitting results of hadronic model. In the latter case, five parameters related to IC are frozen:

- $\alpha_e = 2.5$
- $E_{\text{cut},e} = 10 \text{ TeV}$
- $B = 70 \mu\text{G}$
- $K_{\text{ep}} = 0.1$
- $N_{\text{H}} = 100 \text{ cm}^{-3}$

Based on the best-fit values obtained from group(1), we set α_e , $E_{\text{cut},e}$ and B . The local cosmic-rays (CRs) abundance shows $K_{\text{ep}} = 0.01$. However, we use $K_{\text{ep}} = 0.1$ to illustrate the situation for SNRs. The typical particle number density for shell-type SNRs is $0.01 - 0.1 \text{ cm}^{-3}$ while for SNR-MC systems is $1 - 100 \text{ cm}^{-3}$ [116]. Since all the sources in group (2) are SNR-MC systems, 100 cm^{-3} is adopted.

4.3.2.1 HESS J1745-303

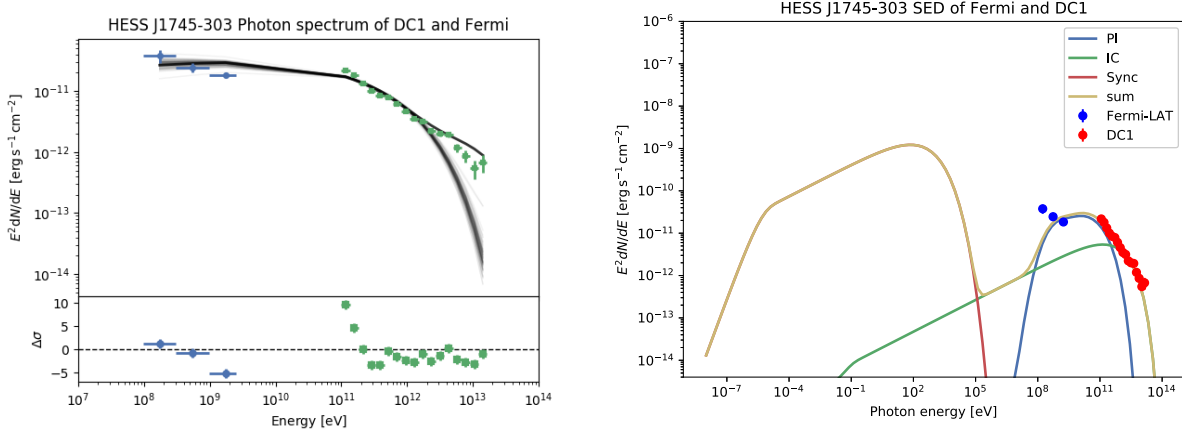


Figure 4.8: Multi-wavelength fitting results of HESS J1745–303. Left: the fitting results of MWL photon spectrum with eight free parameters with residuals. Right: Best-fit SED with radiative models for which the five parameters related to leptonic models are frozen. Red points and blue points are DC-1 data and *Fermi*-LAT data, respectively.

For this analysis, we collected GeV data from *Fermi*-LAT [78]. No evidence for spectral or flux variability are found from the *Fermi*-LAT data. The photon index inferred from the GeV data is similar to that inferred in TeV data (H.E.S.S.).

The left panel of Fig. 4.8 shows the fitting results of multi-wavelength data from HESS J1745–303. We can see that there are two different branches. These branches correspond to the different branches of the walkers. This is the result of large uncertainty of some parameters (B , K_{ep} , and p_{cut}), which can be seen from Table 4.3. This source has only DC-1 data and *Fermi*-LAT data, which results in little constraints on the model fitting. Therefore, we try to freeze some of the parameters related to the leptonic model for comparison. The corresponding SED is displayed in right plot of Fig. 4.8. The Inverse Compton dominates at high energies while proton-proton interaction dominates at low energies. The proton cutoff energy $\log_{10} E_{\text{cut,p}} [\text{TeV}] = 0.09 \pm 0.03$.

4.3.2.2 HESS J1800-240A

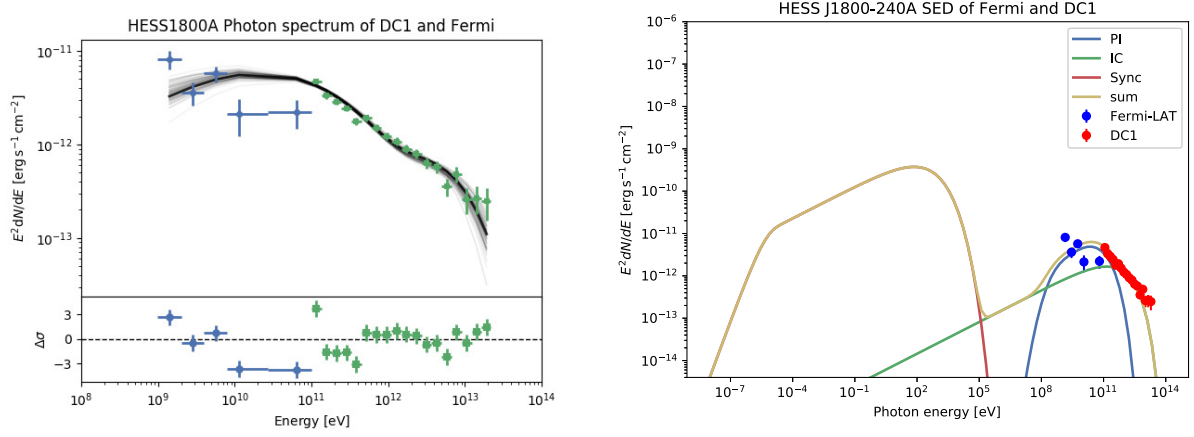


Figure 4.9: Multi-wavelength fitting results of HESS J1800–240A. Left: the fitting results of MWL photon spectrum with eight free parameters with residuals. Right: Best-fit SED with radiative models for which the five parameters related to leptonic models are frozen. Red points and blue points are DC-1 data and *Fermi*-LAT data, respectively.

GeV data from *Fermi*-LAT [52] are used. The left panel of Fig. 4.9 shows the fitting results of multi-wavelength data from HESS J1800–240A. The SED with frozen leptonic parameters is displayed in right panel of Fig. 4.9. The Inverse Compton dominates at high energies while proton-proton interaction dominates at low energies. The proton cutoff energy is at $\log_{10} E_{\text{cut,p}} \text{ TeV} = -0.09 \pm 0.03$.

4.3.2.3 W 28

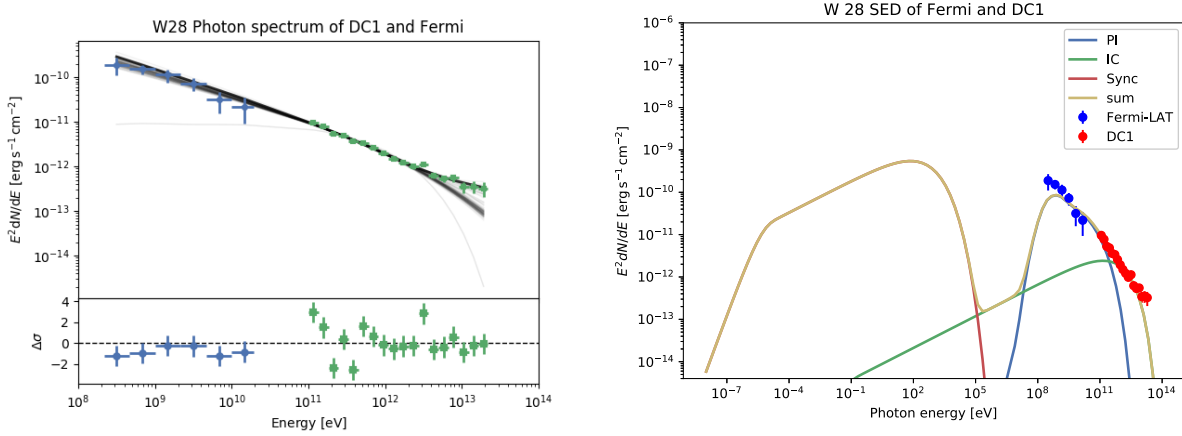


Figure 4.10: Multi-wavelength fitting results of W 28. Left: the fitting results of MWL photon spectrum with eight free parameters with residuals. Right: Best-fit SED with radiative models for which the five parameters related to leptonic models are frozen. Red points and blue points are DC-1 data and *Fermi*-LAT data, respectively.

For W 28, we collect GeV data from *Fermi*-LAT [43]. There are strong indications of variability in *Fermi*-LAT observations of W28, which is probably produced by pulsars in such region [96]. The *Fermi*-LAT spectrum has a break around 1 GeV and connects to the TeV spectrum smoothly, which indicate a physical relationship between these two energies. Based on the spatial correlation between GeV γ -rays and MCs, PI component with time evolution can explain northern part of W 28. The corresponding proton index and gas density are 2.7 and 1 cm^{-3} . By assuming electron-to-proton ratio as $K_{\text{ep}} = 0.01$, the magnetic field strength can be constrained as $B = 160 \mu\text{G}$.

The left panel of Fig. 4.10 shows the fitting results of multi-wavelength data from W 28. In the left part of the figure, we can see two branches. The reason for this is the same as for HESS J1745–303. As seen in Table 4.3, we do not get reasonable values for some of the parameters. For example, $N_{\text{H}} = 0.04 \pm 0.02 \text{ cm}^{-3}$ in this case. It means the contribution of PI is low, and we need more IC contribution to explain the data. However, N_{H} should be larger than 1 for SNR-MC system. The SED with frozen leptonic parameters is displayed in right panel of Fig. 4.10. The Inverse Compton dominates at high energy while proton-proton interaction dominates at low energy. The frozen parameters $\alpha_e = 2.5$ and $N_{\text{H}} = 100 \text{ cm}^{-3}$ seem to have more physical meaning. The corresponding proton cutoff energy is $\log_{10} E_{\text{cut,p}} \text{ TeV} = -0.03 \pm 0.03$.

4.3.2.4 W 51C

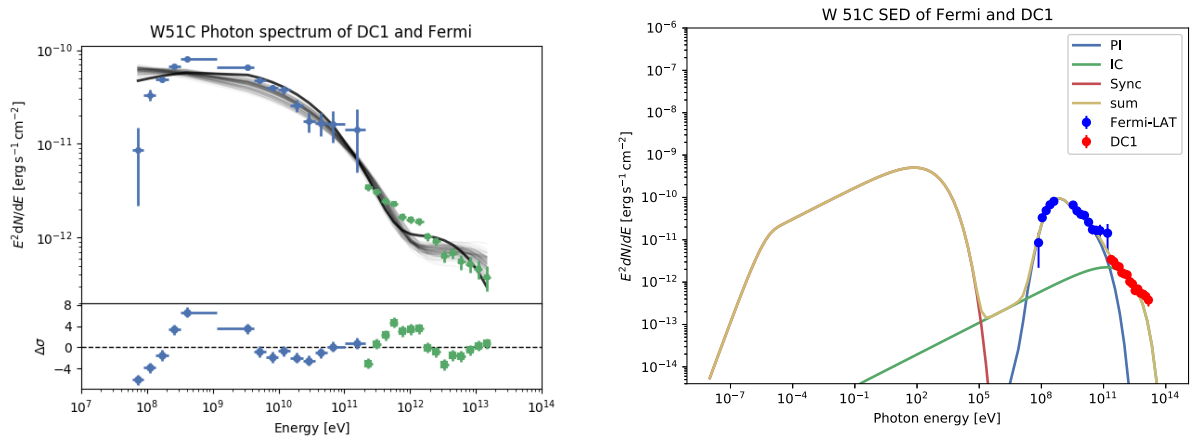


Figure 4.11: Multi-wavelength fitting results of W 51C. Left: the fitting results of MWL photon spectrum with eight free parameters with residuals. Right: Best-fit SED with radiative models for which the five parameters related to leptonic models are frozen. Red points and blue points are DC-1 data and *Fermi*-LAT data, respectively.

For W 51C, GeV data from *Fermi*-LAT [42, 60] are used. The IC-dominated model requires an unreasonable large energy content of electrons ($W_e > 1 \times 10^{51}$ erg) and a low magnetic field ($B = 2 \mu\text{G}$) [42]. Ref. [40] shows that the MWL SED can be explained with a hadronic model with proton acceleration above 100 TeV. The left panel of Fig. 4.11 shows the fitting results of multi-wavelength data from W 51C. There is a small discrepancy in the higher energy part of *Fermi*-LAT data. The SED with frozen leptonic parameters is displayed in right panel of Fig. 4.11. The Inverse Compton dominates at high energy while proton-proton interaction dominates at low energy. The corresponding proton cutoff energy is $\log_{10} E_{\text{cut,p}} \text{ TeV} = -0.16 \pm 0.05$.

4.3.2.5 Conclusions for group (2)

HESS J1745–303, HESS J1800–240A, W 28, and W 51C do not appear to be promising PeVatron candidates according to the DC-1 and *Fermi*-LAT data. They are dominated by Inverse Compton at high energies when the parameters related to leptonic model are frozen. However, in this case, a pronounced hadronic contribution can be seen at low energy corresponding to about 1 TeV protons.

4.3.3 Group (3): With DC-1 Data Only

The group (3) sources do not have data of other wavelengths. HESS J1614–518 is FL8Y J1615.3–5146e in the LAT 8-year Point Source List (FL8Y).⁶ However, we do not have access yet to the spectral points corresponding to the FL8Y analysis. HESS J1912+101 is not in

⁶<https://fermi.gsfc.nasa.gov/ssc/data/access/lat/fl8y/>

any *Fermi*-LAT catalog. In this case, we need to consider the hadronic and leptonic models separately. Each model has three free parameters: the amplitude of proton (electron), the index of proton (electron), and the cutoff energy of proton (electron). We use A_e rather than K_{ep} , since $A_e = K_{ep}A_p$. We use the same numbers of *walkers*, *burn* and *run* as what we set for Group (1) and (2). The results are shown in table 4.4

4.3.3.1 HESS J1614-518

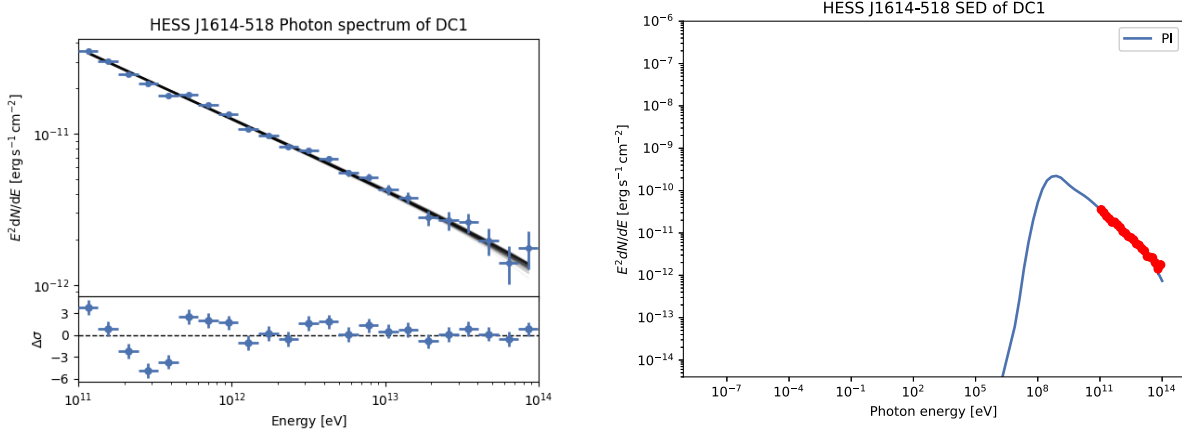


Figure 4.12: Multi-wavelength fitting results of HESS J1614–518 with three free parameters in **hadronic** case. Left: the fitting results of MWL photon spectrum. Right: Corresponding best-fit SED with PI model.

For the hadronic case, PI process is adopted. For the leptonic case, IC process is adopted. Fig. 4.12 and fig. 4.14 give the MWL fitting results in hadronic and leptonic case. The corresponding proton cutoff energy is $\log_{10} E_{\text{cut,p}} [\text{TeV}] = 3.85 \pm 0.11$. Fig. 4.13 and fig. 4.15 show the corresponding corner plots in hadronic and leptonic case. $\log_{10} A_p$ and α_p have good Gaussian distribution while $\log_{10} E_{\text{cut,p}}$ has a non-Gaussian distribution. The maximum possible cutoff energy is favored.

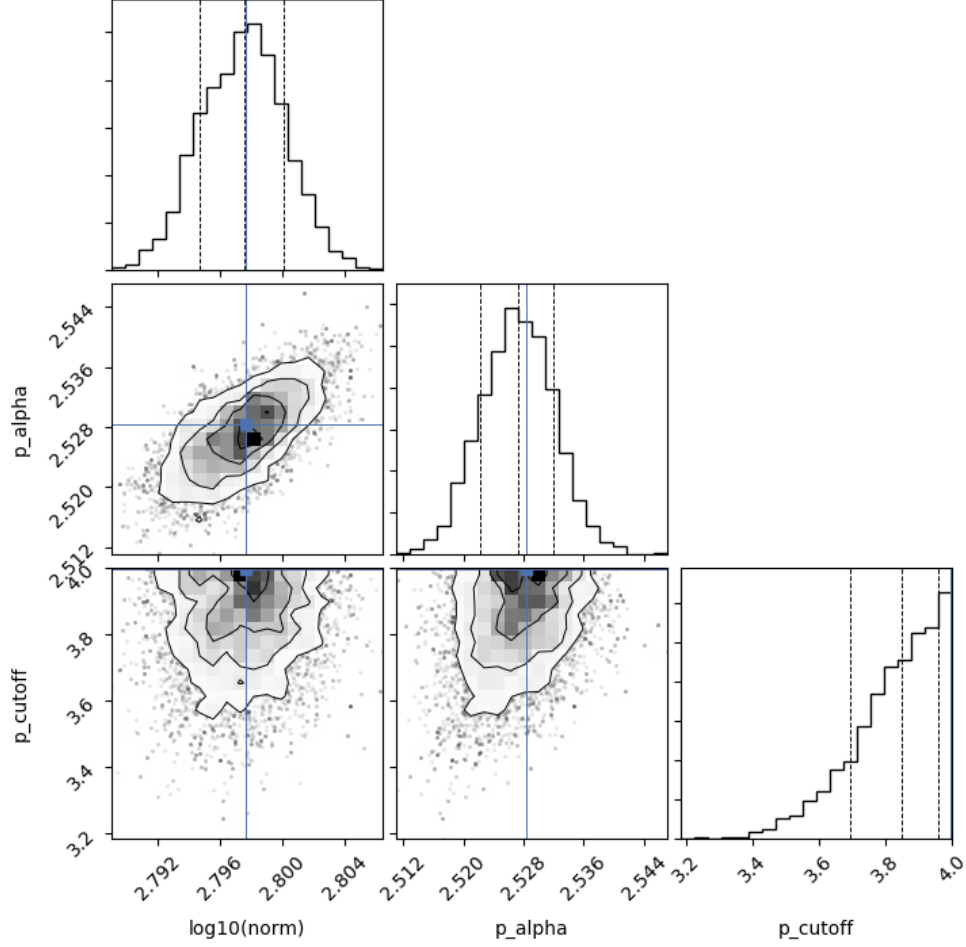


Figure 4.13: Multi-wavelength fitting results of HESS J1614–518 with three free parameters in **hadronic** case. The corner plot of the corresponding parameters.

4.3.3.2 HESS J1912+101

The Sino-German Urumqi λ -6-cm survey and the Effelsberg λ -11-cm and λ -21-cm surveys support that HESS J1912+101 is an old SNR [102] with distance around 4.1 kpc [103]. Even if no identifying counterpart was found for HESS J1912+101 in other wavelengths, it remains a SNR candidate [74]. Fig. 4.16 and fig. 4.17 gives the MWL fitting results for hadronic case. The corresponding proton cutoff energy is $\log_{10} E_{cut,p} [\text{TeV}] = 3.4 \pm 0.4$. $\log_{10} A_p$ and α_p have good Gaussian distribution while $\log_{10} E_{cut,p}$ has a non-Gaussian distribution. Again the maximum allowed cutoff energy is favored.

4.3.3.3 Conclusions for group (3)

When we consider the DC-1 data only, HESS J1614–518 and HESS J1912+101 are promising PeVatron candidates for pure hadronic models. Nonetheless, the lack of MWL data prevents a firm conclusion.

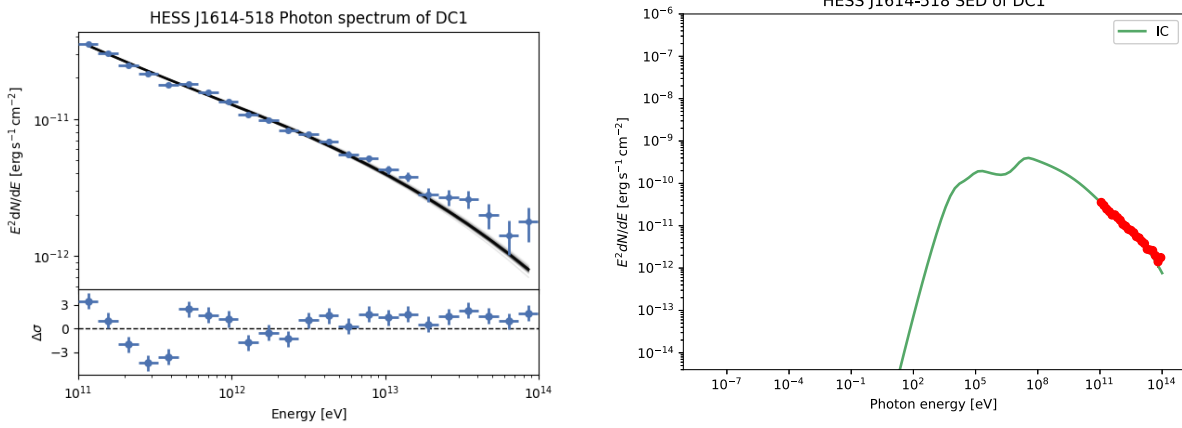


Figure 4.14: Multi-wavelength fitting results of HESS J1614–518 with three free parameters in **leptonic** case. Left: the fitting results of MWL photon spectrum. Right: Corresponding best-fit SED with IC model.

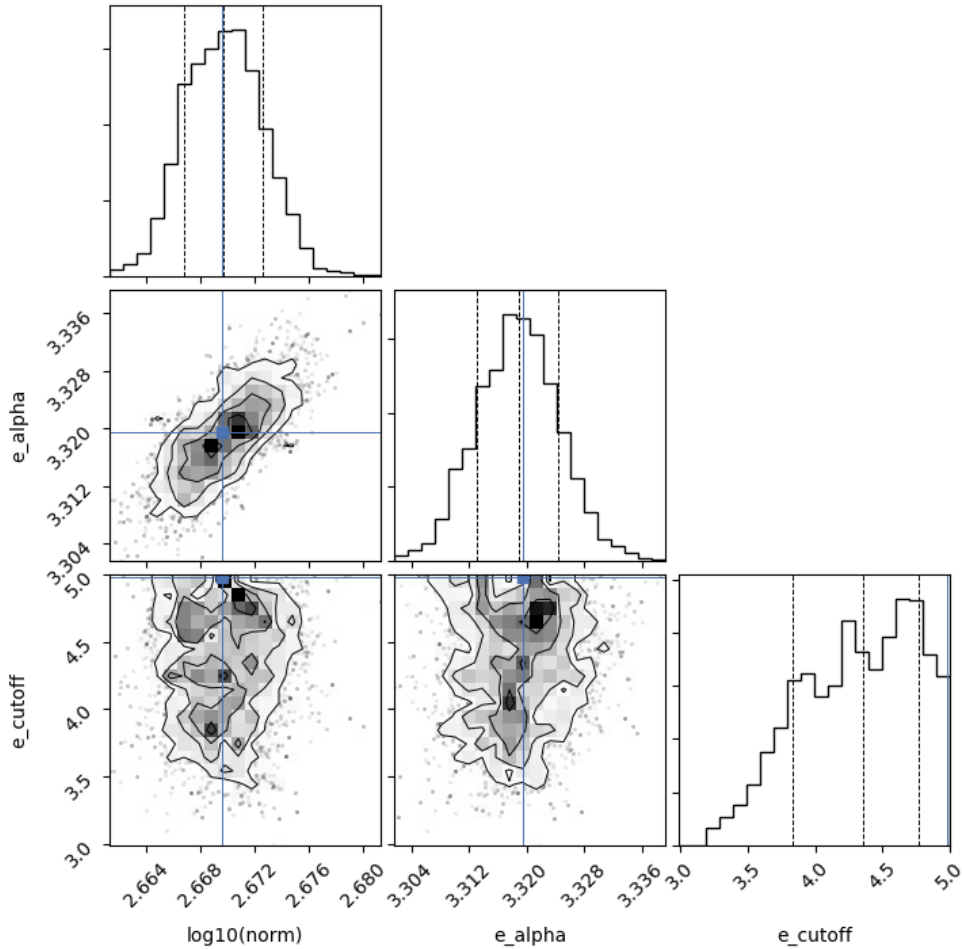


Figure 4.15: Multi-wavelength fitting results of HESS J1614–518 with three free parameters in **leptonic** case. The corner plot of the corresponding parameters.

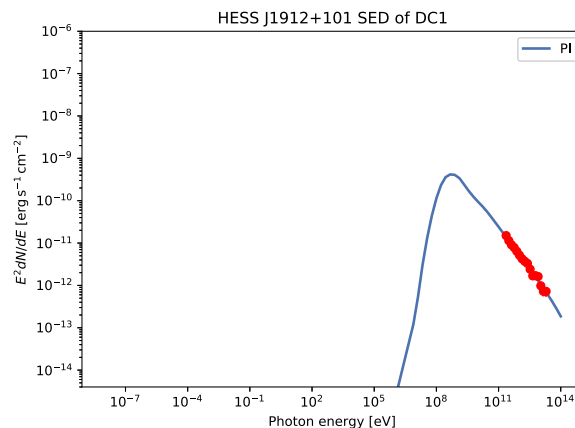
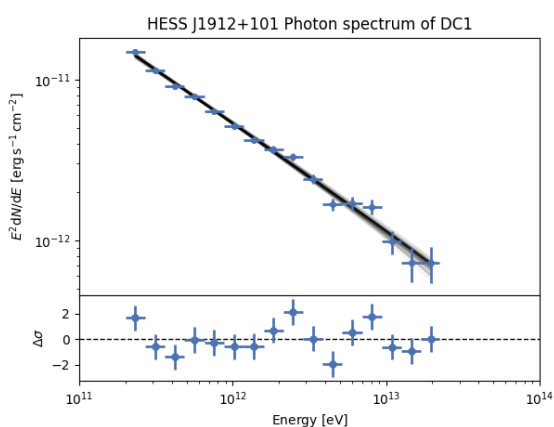


Figure 4.16: Multi-wavelength fitting results of HESS J1912+101 with three free parameters in **hadronic** case. Left: the fitting results of MWL photon spectrum. Right: Corresponding best-fit SED with PI model.

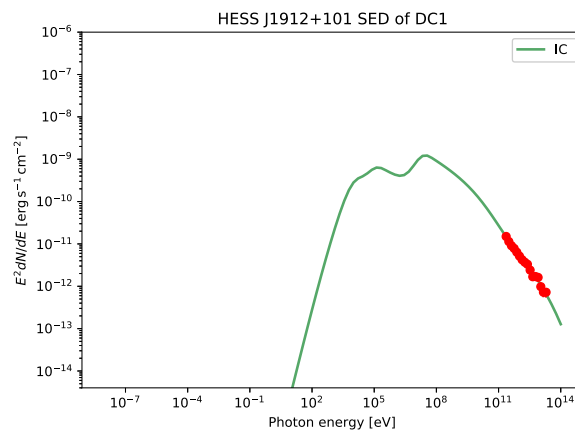
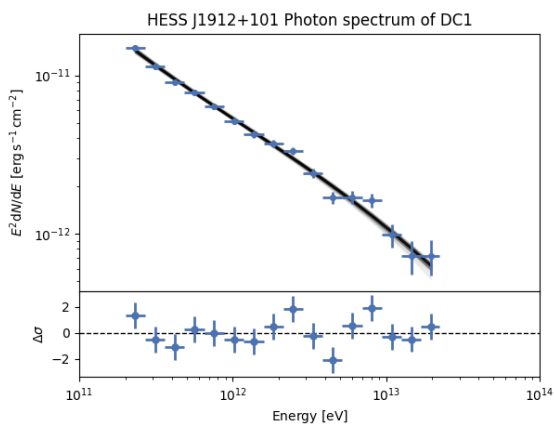


Figure 4.17: Multi-wavelength fitting results of HESS J1912+101 with three free parameters in **leptonic** case. Left: the fitting results of MWL photon spectrum. Right: the corner plot of the corresponding parameters.

SNR name	K_{ep}	$\log_{10} A_{\text{p}}$ [TeV $^{-1}$]	α_{e}	α_{p}	$\log_{10} E_{\text{cut,e}}$ [TeV]	$\log_{10} E_{\text{cut,p}}$ [TeV]	B [μG]	N_{H} [cm $^{-3}$]
RX J1713.7–3946	0.06 ± 0.01	47.99 ± 0.05	2.53 ± 0.02	1.27 ± 0.16	1.503 ± 0.016	-0.21 ± 0.05	17.29 ± 0.15	0.08 ± 0.02
HESS J1731–347	0.42 ± 0.12	47.09 ± 0.10	2.45 ± 0.11	1.0 ± 0.6	1.51 ± 0.06	0.12 ± 0.08	16.8 ± 0.5	0.04 ± 0.03
W 49B	0.61 ± 0.15	49.85 ± 0.14	2.17 ± 0.03	0.10 ± 0.04	-0.28 ± 0.02	1.02 ± 0.09	0.27 ± 0.11	0.004 ± 0.001
HESS J1745–303	0.09 ± 0.02	48.72 ± 0.10	2.92 ± 0.06	2.2 ± 0.7	0.64 ± 0.05	0.69 ± 0.19	56 ± 18	0.004 ± 0.001
HESS J1745–303 *		47.86 ± 0.02		1.91 ± 0.03		0.09 ± 0.03		
HESS J1800–240A	0.82 ± 0.18	47.28 ± 0.12	1.9 ± 0.2	0.15 ± 0.16	0.07 ± 0.07	1.18 ± 0.09	3 ± 2	0.07 ± 0.03
HESS J1800–240A *		47.35 ± 0.02		1.64 ± 0.06		-0.09 ± 0.03		
W 28	0.30 ± 0.09	47.78 ± 0.11	3.98 ± 0.05	2.7 ± 1.3	2.3 ± 0.3	2.1 ± 0.8	29 ± 12	0.04 ± 0.02
W 28 *		47.45 ± 0.02		2.03 ± 0.07		-0.03 ± 0.03		
W 51C	0.49 ± 0.09	49.00 ± 0.19	2.94 ± 0.15	1.10 ± 0.12	-0.02 ± 0.14	1.82 ± 0.17	15 ± 8	0.04 ± 0.01
W 51C *		48.15 ± 0.02		2.48 ± 0.01		-0.16 ± 0.05		

Table 4.3: Best-fit parameters for group (1) and (2). From the left to the right are the SNRs’ name, ratio between electron and proton, proton amplitude, electron distribution index, proton distribution index, electron spectrum cutoff energy, proton spectrum cutoff energy, magnetic field, and target proton density. * indicates that we freeze the parameters related to electrons.

SNR name	$\log_{10} A_e$ [TeV ⁻¹]	$\log_{10} A_p$ [TeV ⁻¹]	α_e	α_p	$\log_{10} E_{\text{cut},e}$ [TeV]	$\log_{10} E_{\text{cut},p}$ [TeV]
HESS J1614–518 hadronic		49.798 ± 0.003		2.527 ± 0.005		3.85 ± 0.11
HESS J1614–518 leptonic	47.670 ± 0.003		3.319 ± 0.006		4.4 ± 0.5	
HESS J1912+101 hadronic		50.037 ± 0.012		2.719 ± 0.017		3.4 ± 0.4
HESS J1912+101 leptonic	47.918 ± 0.012		3.562 ± 0.016		3.8 ± 0.8	

Table 4.4: Best-fit parameters for group (3). From the left to the right are the SNRs’ name, electron amplitude, proton amplitude, electron distribution index, proton distribution index, electron spectrum cutoff energy, proton spectrum cutoff energy.

4.4 Possible Improvements for DC-1

In this section, we show the analysis results of real TeV data (H.E.S.S.) to suggest possible improvements for the simulated data. Difference between H.E.S.S. data and DC-1 data of group (1) can be seen. Fig. 4.18, Fig. 4.19 and Fig. 4.20 show the MWL fitting results for the real data. Comparing these plots to the Fig. 4.5, Fig. 4.6 and Fig. 4.7, we can see that the models of SED of HESS J1731–347 and W 49B with real data are similar to those obtained with DC-1 data. For RX J1713.7–3946, a better fit is obtained with respect to DC-1 data. Table 4.5 gives the corresponding parameters for the analysis. We suggest that the future simulation for CTA data can be based on these values. The comparison between DC-1 and real data can be seen in Appendix A. The modeled SED of DC-1 data and real data are similar at low energy (e.g. for RX J1713.7–3946, DC-1 data and real data are similar below 10 TeV). However, here are still some differences in the best-fit parameters.

Obviously, for high-density environments (e.g. SNR-MC systems), the γ -ray emission should be PI dominated since such environments include more proton targets. Note that SNRs in SNR-MC systems are mostly with old age. As the magnetic field increases, the IC component will be suppressed for a given synchrotron flux due to the decrease of the electrons number. In this case, the number of CR protons needs to be increased to account for the observed γ -ray flux.

Although CTA is a γ -ray facility with crucial information on the maximum energy of the accelerated particles, MWL data (e.g. X-ray observation) are also important to study PeVatron candidates. In particular, X-ray data can be used in the following way:

- In morphological analysis, SNRs with strong correlation between GeV to TeV γ -ray imply a likely leptonic origin of the emission.
- The lack of thermal X-ray emission implies low gas density. As a result, there should be a high energy content of accelerated protons in the hadronic model of the TeV γ -rays.

A likely important phenomenon for SNR-MC system is magnetic field amplification. The considerable difference between the velocity of the MC and that of the SNR shock generates a velocity shear that is responsible for such magnetic-field amplification, resulting in a magnetic field value above $100 \mu\text{G}$. In addition, when the SNR collisionless shock accelerates particles effectively which results in CRs streaming instability [23], magnetic field amplification will also happen.

Further steps could be:

- Comparison between X-ray and TeV γ -ray morphology;
- Comparison of the results from model fitting with and without X-ray data;
- Simulation of magnetic field amplification;
- Spatially resolved high resolution spectroscopy of the shock.

SNR name	K_{ep}	$\log_{10} A_{\text{p}}$ [TeV ⁻¹]	α_{e}	α_{p}	$\log_{10} E_{\text{cut,e}}$ [TeV]	$\log_{10} E_{\text{cut,p}}$ [TeV]	B [μG]	N_{H} [cm ⁻³]
RX J1713.7–3946	0.23 ± 0.03	47.18 ± 0.05	2.41 ± 0.04	1.8 ± 0.4	1.64 ± 0.03	0.38 ± 0.09	14.8 ± 0.3	0.023 ± 0.010
HESS J1731–347	0.37 ± 0.12	47.22 ± 0.18	2.38 ± 0.09	0.7 ± 0.5	1.25 ± 0.06	0.5 ± 1.1	20.1 ± 1.0	0.023 ± 0.016
W 49B	0.74 ± 0.17	50.23 ± 0.15	2.05 ± 0.04	0.07 ± 0.03	-0.61 ± 0.06	0.72 ± 0.11	0.68 ± 0.20	0.015 ± 0.005

Table 4.5: The results of parameters for group (1) from real data. From the left to the right are the SNRs' name, ratio between electron and proton, proton amplitude, electron distribution index, proton distribution index, electron spectrum cutoff energy, proton spectrum cutoff energy, magnetic field, and particle number density.

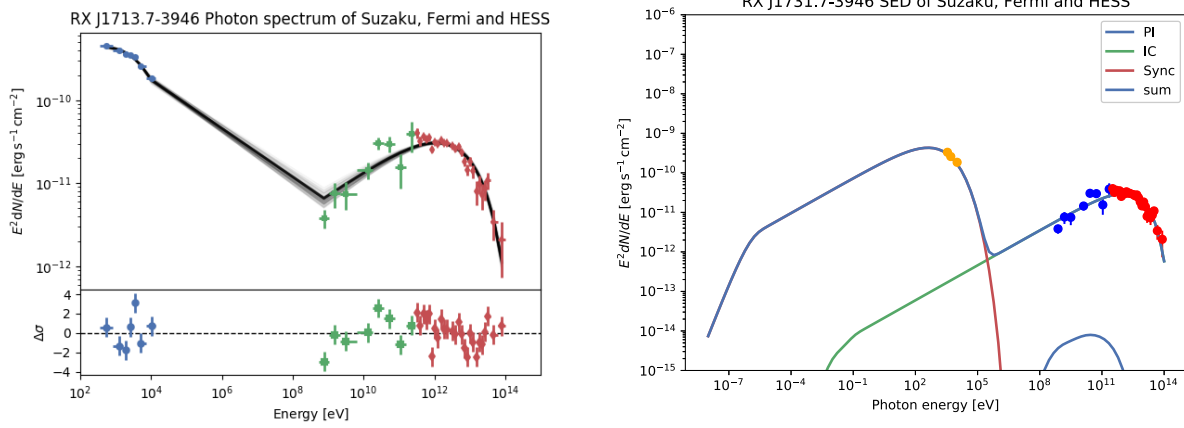


Figure 4.18: Real data fitting results of RX J1713.7–3946 with eight free parameters. Left: the fitting results of real photon spectrum. Right: the real data and the radiative models of fitting.

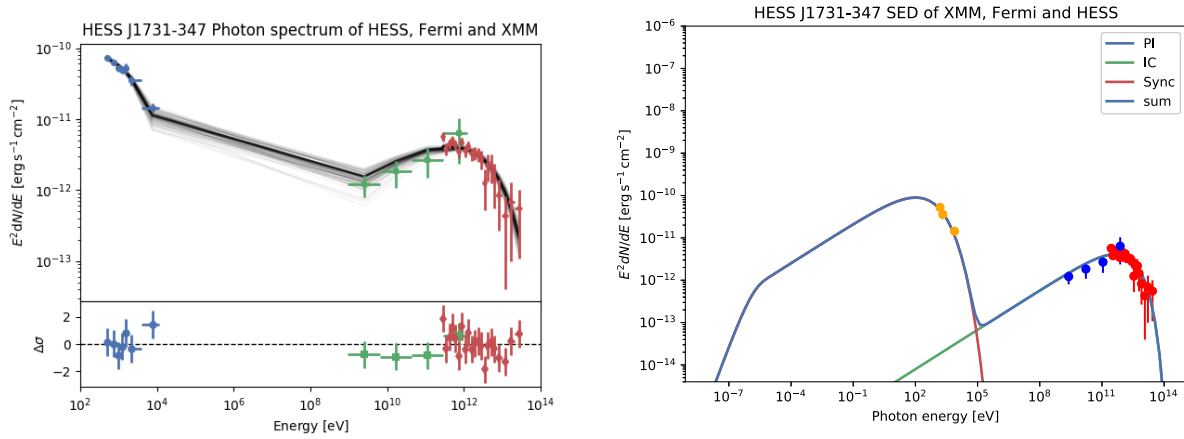


Figure 4.19: Real data fitting results of HESS J1731–347 with eight free parameters. Left: the fitting results of real photon spectrum. Right: the real data and the radiative models of fitting.

4.5 Discussion

Leptonic model can not explain a hard spectrum at high energies. In the group (1), we notice that there are discrepancies between the models and *Fermi*-LAT data at low energies. However, considering that the DC-1 data are close to real data (see Fig. A.1), we can use the best fit parameters from real data in table 4.5 and plot the corresponding SED (same as section 4.4) together with the simulated DC-1 data. Fig. 4.21 shows the best-fit SED from real data together with simulated DC-1 data. We can see that the low-energy part of *Fermi*-LAT data appears to be well modeled. It is probably due to the larger flux uncertainty of H.E.S.S. compared to DC-1 data.

There has been a strong debate about leptonic domination or hadronic domination for RX J1713.7–3946. Both the PI [12] and the IC [59] processes are suggested as the dominant

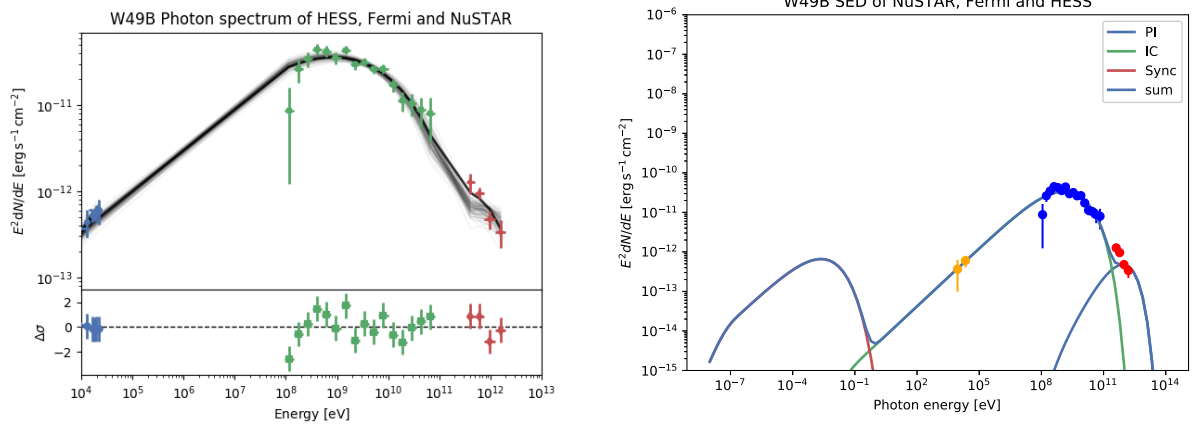


Figure 4.20: Real data fitting results of W 49B with eight free parameters. Left: the fitting results of real photon spectrum. Right: the real data and the radiative models of fitting.

radiative process. By applying a non-linear kinetic theory of CR acceleration in SNRs, RX J1713.7–3946 can be interpreted as a source that converts more than 35% of the kinetic energy of explosion into nuclear CRs with hadronic origin [12]. Under the assumption of uniform circumstellar medium (CSM) models, high relativistic electron-to-proton ratios and a low density are required to match the *Suzaku* X-ray observations of RX J1713.7–3946, which rules out PI as the dominant process in the γ -ray band [59].

A possible argument for pion-decay in RX J1713.7–3946 comes from the high magnetic field strength in SNRs (> 1 mG), which means a low relativistic electron density for a given X-ray synchrotron flux [110]. The corresponding contribution to the TeV flux will be low. However, the broadband γ -ray emission observed by *Fermi*-LAT is more consistent with IC component [46]. The high magnetic fields (100 – 600 μ G) inferred from X-ray observations also suggest that there are probably some magnetic field amplification mechanism associated with the shocks of SNRs [24]. Therefore, detailed X-ray observations for SNRs to derive their magnetic field is necessary for searching PeVatron candidates.

We also notice that the PI component is almost non-existent for HESS J1731–347. However, this is not the case if we do not consider the X-ray data in the fit, as seen in Fig. 4.22. With $\log_{10} E_{\text{cut,p}} [\text{TeV}] = 2.39 \pm 0.15$, it gets closer to a PeVatron candidate.

In group (2), by comparing two different fitting methods, it seems more reasonable to freeze the leptonic parameters. If we fit with eight parameters, the MCMC method will produce some unphysical values with non-Gaussian distributions. Such values result in a non-physical shape of the SED, and the non-Gaussian distributions lead to some ‘branches’ in the SED. When there is a break in the *Fermi*-LAT data, a PI component often reproduces well the low-energy γ -ray data. On the contrary, in the case of a hard TeV spectrum, we need a PI component at high energies. In this group, HESS J1745–303, W 28 and W 51C have unreasonable values of α_e . It is one of the reasons for fitting leptonic parameters. HESS J1800–240A and W51C have unreasonable values of α_p . We do not plan to solve this problem since it is likely related to the simulation

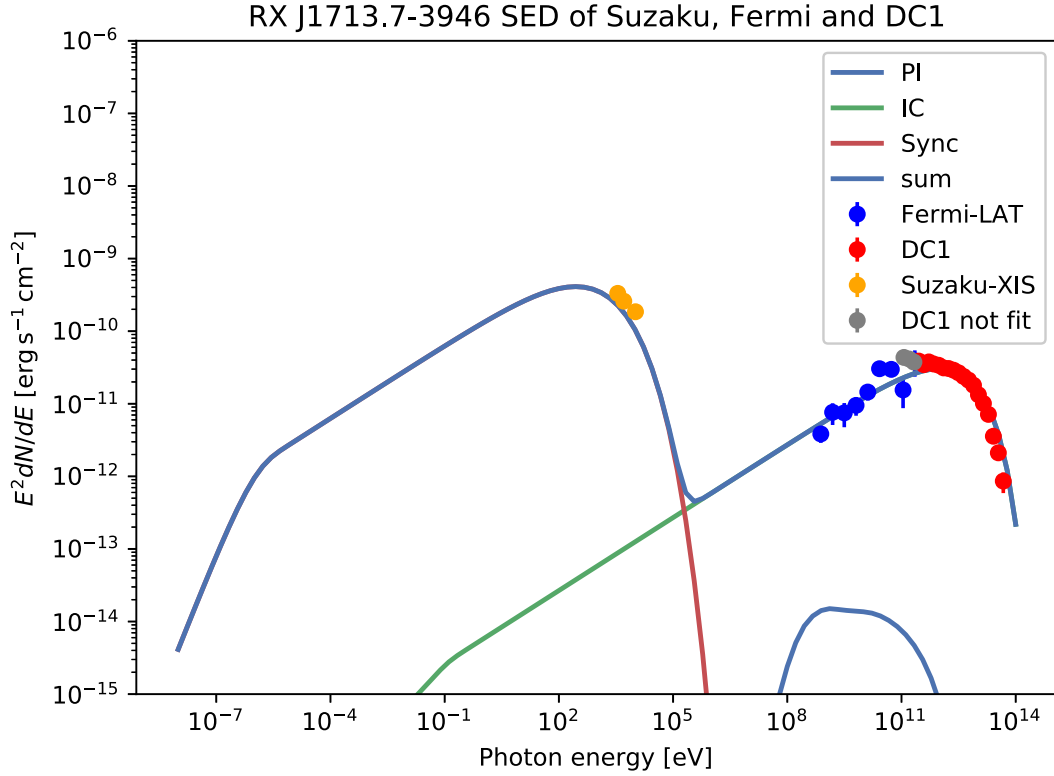


Figure 4.21: Best-fit SED with radiative models from real data. Red points, grey points, and blue points are DC-1 data fit in the program, DC-1 data not fit in the program, and *Fermi*-LAT data, respectively.

process of DC-1.

To search PeVatron in a MWL view, a main debate point concerns the lack on presence of thermal X-ray emission. No thermal X-ray emission implies the need of a large synchrotron component, resulting in a huge IC contribution to the γ -ray flux, and consequently a low PI contribution. The lack of thermal X-ray emission may be understood from the low gas density resulting efficient CR acceleration [97]. It means that the gas heating can be suppressed to the point where thermal X-ray emission by strong particle acceleration is no longer expected. Therefore, X-ray observations to search thermal X-ray emission can help us to find PeVatron candidates.

We do not consider bremsstrahlung in this thesis following the *Naima* example. This process has no significant impact on the SED in hadro-leptonic case (e.g. Ref. [71] Fig. 5 right panel).

4.6 Conclusion

The best-fit parameters are shown in table 4.3 and table 4.4. If the DC-1 data were representative of reality, we could rule out most of the sources in table 4.3 as PeVatron candidates. None of the sources has $\log_{10} E_{\text{cut,p}} [\text{TeV}] \geq 3$ in lepto-hadronic models. All the two sources (HESS

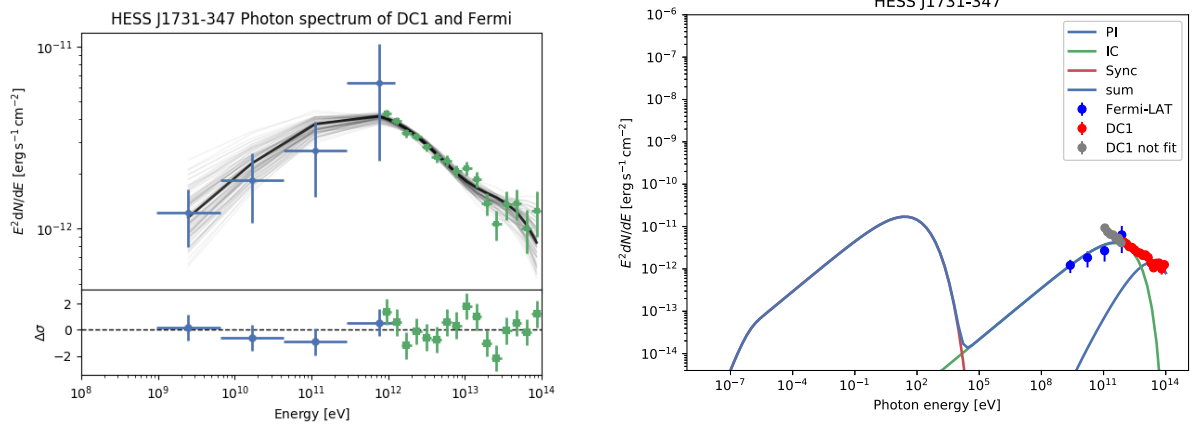


Figure 4.22: Multi-wavelength fitting results of HESS J1731–347 with eight free parameters. Left: the fitting results of MWL photon spectrum. Right: Corresponding best-fit SED with radiative models. Red points, grey points, and blue points are DC-1 data fit in the program, DC-1 data not fit in the program, and *Fermi*-LAT data, respectively.

J1614–518 and HESS J1912+101) of group (3) in table 4.4 have $\log_{10} E_{\text{cut,p}} [\text{TeV}] \geq 3$ in the purely hadronic case, but we can not say they are PeVatron candidates since only very-high-energy data are considered.

If CTA observes what current IACT have seen, sources with good MWL coverage could be ruled out as PeVatron candidates. Notice that in the CTA Science Paper, the targets of PeVatron include four sources of unknown type.

RX J1713.7–3946 appear to be dominated by leptonic component. HESS J1731–347 (considering *Fermi*-LAT and DC-1 data) and W 49B are dominated by hadronic components at high energies and by a leptonic component at low energies. The sources with *Fermi*-LAT and DC-1 data are dominated by hadronic component at low energies and by leptonic component at high energies. We also find for some objects a hadronic component at lower energies, typically corresponding to a break in the *Fermi*-LAT SED. The modelling that we have performed for MWL real data of the sources can be useful in the future to simulate more realistic data. We can draw the conclusion that MWL data are essential to distinguish a lepto-hadronic model from a hadronic model, which can be seen by comparing the three groups.

Conclusion

CTA is a powerful upcoming observatory for VHE γ -ray astronomy. Located in two sites, in the Northern and Southern hemispheres, respectively, the CTA observatory will have access to the entire sky with an unprecedented sensitivity, 5 – 20 times better (depending on energy) than current observatories. One of the key science programs of CTA is the search of CR PeVatrons. The origin of the knee of the CR spectrum can be figured out according to the γ -ray emission from accelerated particles in such PeVatrons, with SNRs being the favored accelerators.

The CTA Consortium has simulated observations of SNRs in the first data challenge, DC-1, whose goal has been the preparation of high-level CTA analysis. We reconstructed simulated DC-1 spectra of SNRs using *ctools*. The reconstructed parameters are in overall good agreement with the input simulations, demonstrating the robustness of the analysis tools. Nonetheless, we observe significant residuals for some of the objects that are suspected to arise from the modeling of the field of view. Only the brightest sources are included in the fit procedure, so that contamination from multiple faint objects could cause deviations from the true model. Ongoing work within the CTA Consortium to catalog the entire Galactic plane, accounting for overlapping sources, will benefit to studies of individual bright sources, such as presented in this thesis.

We collected MWL data for DC-1 objects to build the broad-band SEDs of prominent PeVatron candidates. We modeled their broad-band SEDs with the *Naima* fitting package, considering in particular synchrotron radiation, inverse Compton radiation, and pion decay resulting from accelerated protons. Most of the broad-band SEDs are successfully reproduced by such a simple model. For some of the objects, the low-energy γ -ray break in the *Fermi*-LAT data suggests acceleration of cosmic rays up to TeV energies. The hadronic component could dominate the higher γ -ray energy band, suggesting acceleration of protons beyond TeV energies.

The DC-1 data were simulated following a simple spectral model (power-law or power-law with an exponential cutoff). Given the high γ -ray statistics, the fit of radiative models to DC-1 spectra does not enable firm conclusions as to whether CTA can retrieve a clear-cut signature of PeV acceleration. We suggest possible improvements for the next data challenge, with inputs of the CTA simulations derived directly from radiative models, which could help assessing the full potential of CTA in PeVatron searches. The combination of γ -ray spectral observations and morphological studies with MWL data will likely be crucial to determine whether SNR systems indeed accelerate CRs up to the knee or whether new candidates should be identified.

Appendix A

Comparison of spectra between H.E.S.S. and DC-1

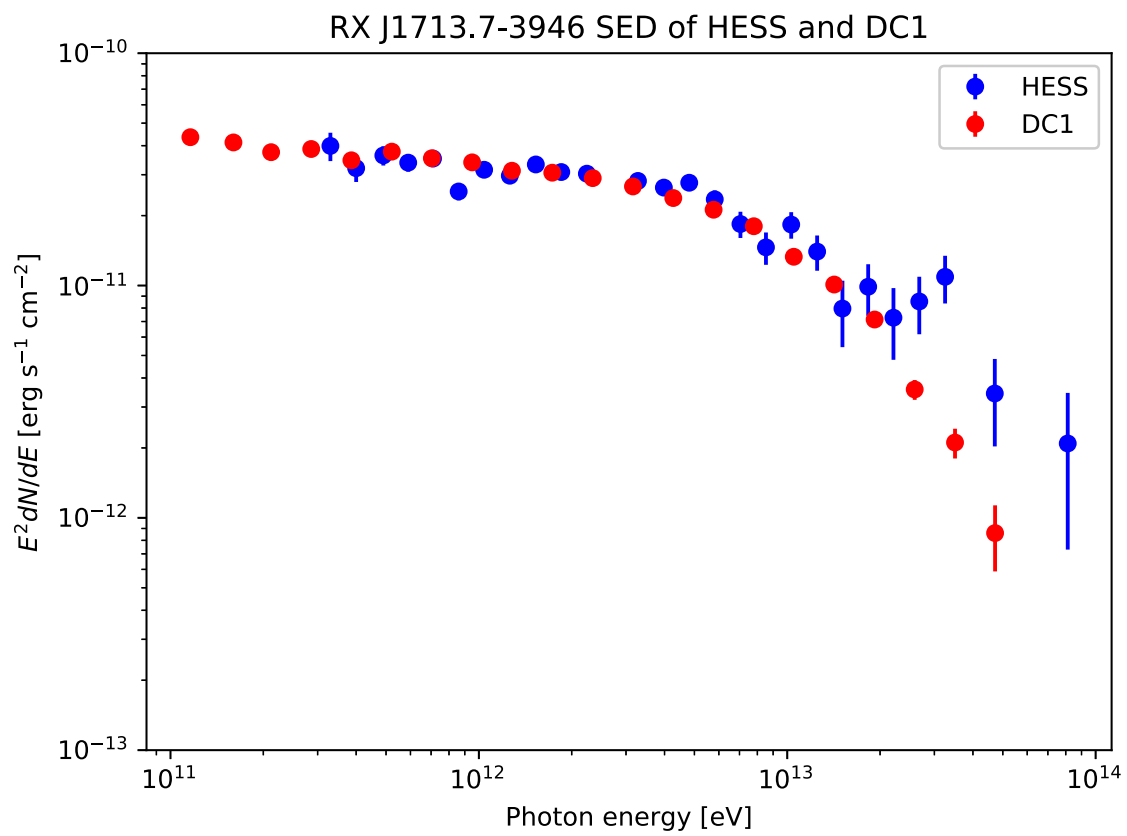


Figure A.1: Spectra from H.E.S.S. and DC-1 of RX J1713.7–3946.

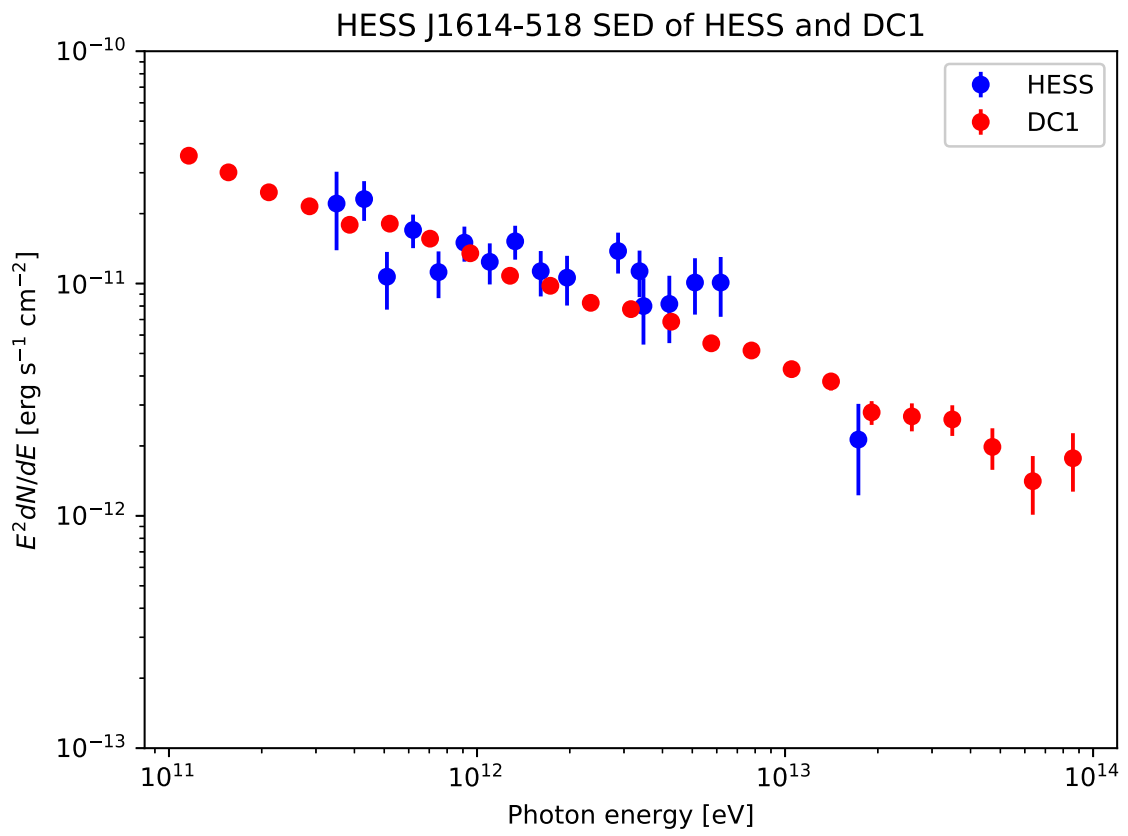


Figure A.2: Spectra from H.E.S.S. and DC-1 of HESS J1614–518.

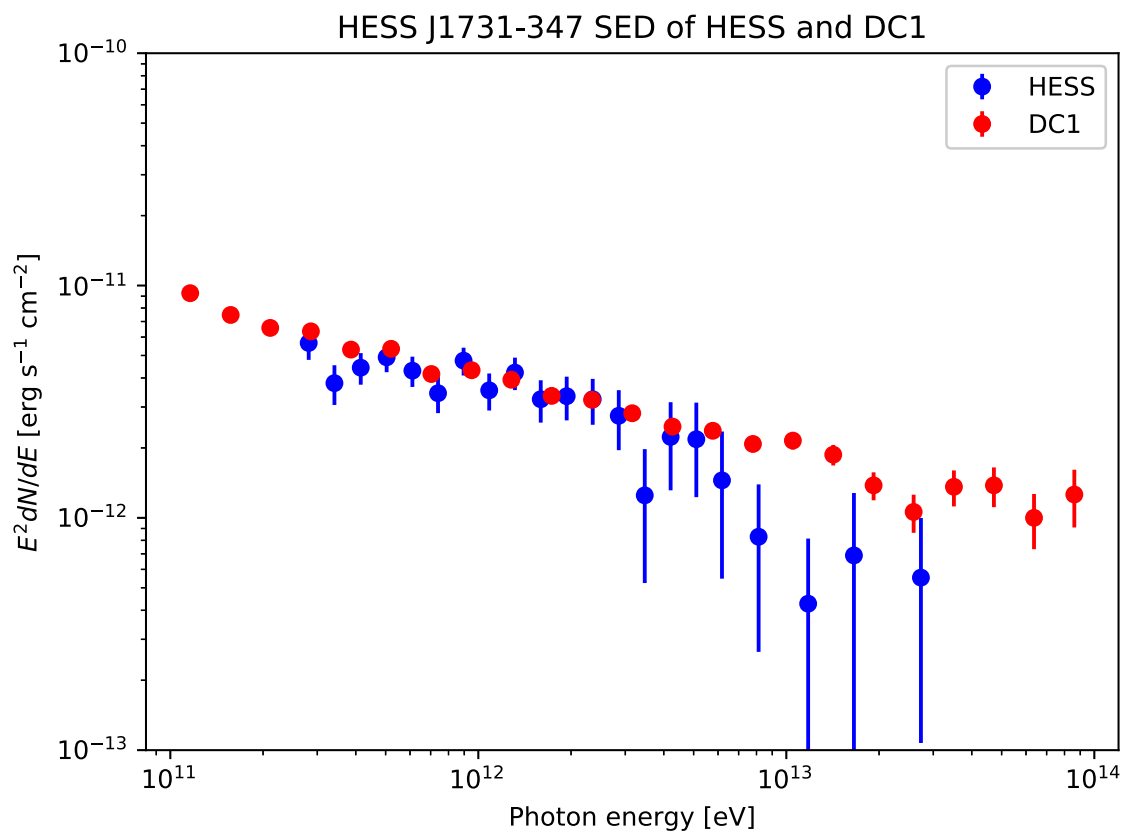


Figure A.3: Spectra from H.E.S.S. and DC-1 of HESS J1731–347.

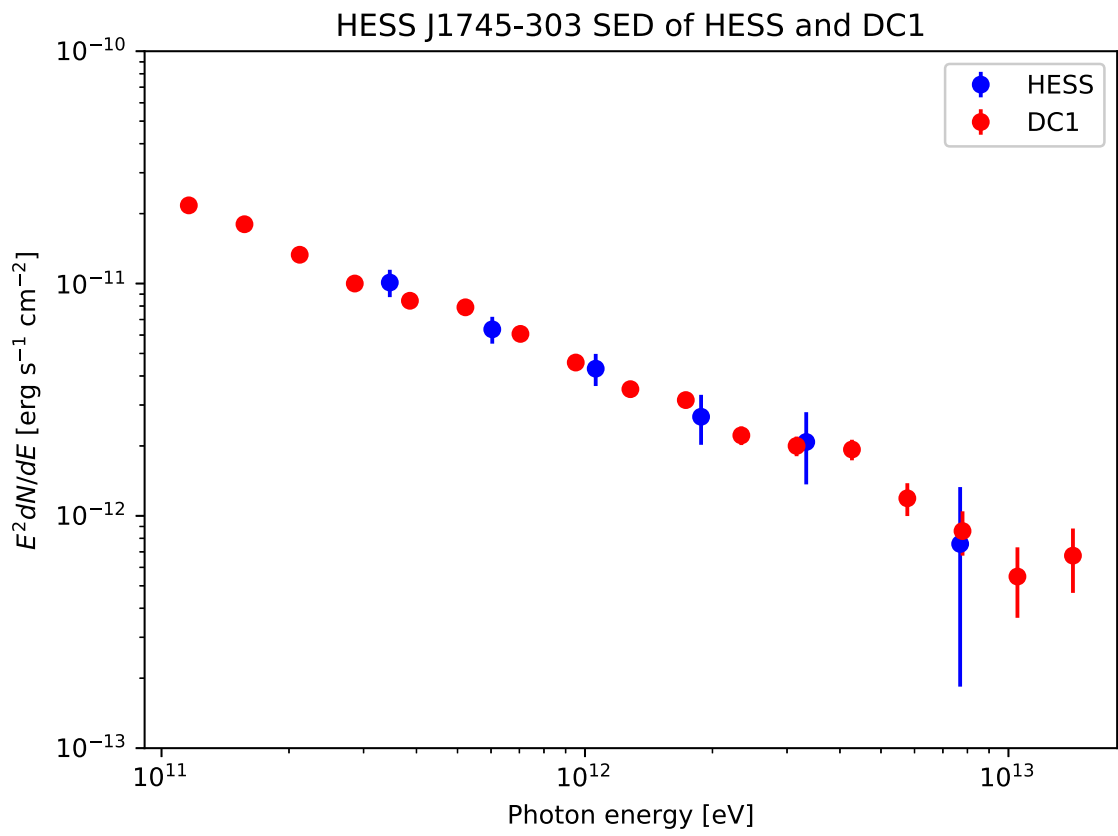


Figure A.4: Spectra from H.E.S.S. and DC-1 of HESS J1745–303.

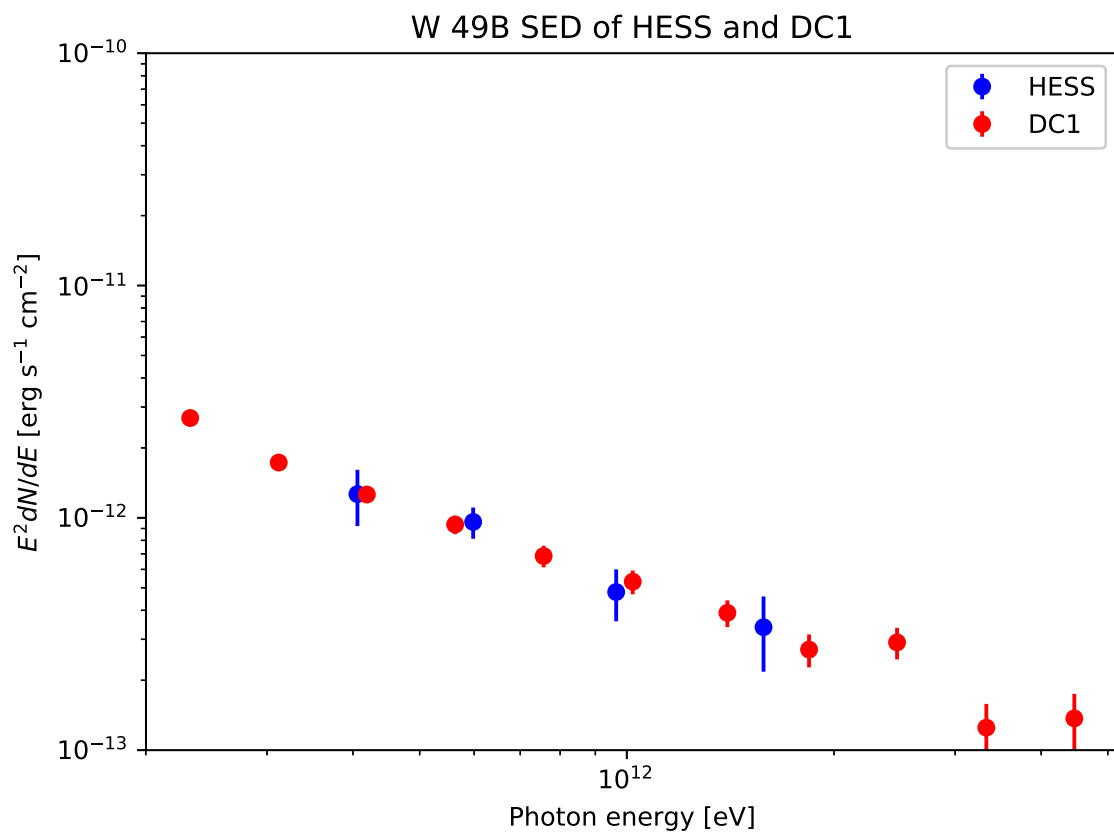


Figure A.5: Spectra from H.E.S.S. and DC-1 of W 49B.

Appendix B

AGN flare simulation

Active Galactic Nuclei (AGN) consist of a supermassive black hole (SMBH), an accretion disk, a dust corona, and a relativistic jet. VHE γ -ray observations of AGN help us to probe the physics of extreme environments. AGNs show variability across the entire electromagnetic spectrum at different time scales. Understanding AGN flares help us to constrain the physical processes of AGN. However, the definition of AGN flares is unclear. The most violent outbursts are often called 'flares'.

Besides my work on spectral and morphological reconstruction of SNRs discussed in the thesis, I dedicated part of my work to variability studies of AGN within the CTA Collaboration. This work is summarized in the following proceedings, published by the French Society of Astronomy and Astrophysics (SF2A).

In a nutshell, I used a generic definition of a flare, based on the coherent emission of a source above a given flux level, to determine the flare duty cycle of AGNs based on simulations of a red-noise log-normal process.

Backward Fourier transform is used for constructing AGN light curve. Notice that such method can be used not only at γ -ray energies but also at other energies (e.g. X-ray). The visibility window is important for ground-based γ -ray telescopes. It is studied to estimate the effect of sampling on the observable number of flares. According to this study, the duty cycle can be estimated for any fractional rms variability and power spectral density index.

ESTIMATION OF THE FLARE DUTY CYCLE OF AGNS BASED ON LOG-NORMAL RED-NOISE PROCESSES

Z.-W. Ou¹ and J. Biteau¹

Abstract. Active Galactic Nuclei (AGN) show variability on time scales ranging from years down to minutes, e.g. in the TeV band, with outbursts often called flares. We aim at estimating the number of flares observable during a long-term monitoring campaign, depending on their flux and variability time scales. We use backward Fourier transform to construct AGN light curves as realizations of a pseudo-red-noise, log-normal process. Using a simple definition of a flare, we map their duty cycle as a function of threshold-flux and flare-duration values. The flare duty cycle can be entirely defined by two quantities: the slope of the power spectral density and the normalized variance of the process. We also produce visibility windows in order to estimate the effect of sampling on the observable number of flares.

Keywords: galaxy: nucleus, galaxies: active, gamma rays: galaxies, methods: statistical

1 Introduction

An active galactic nucleus (AGN) is a compact region in the center of a galaxy, which consists of a supermassive black hole with an accretion disk. AGNs emit relativistic jets and have strong radiation with flux variability from radio to γ -ray. However, the definition of an AGN flare, providing the amplitude and duration of flux variations, can be ambiguous. What fraction of the time does an AGN spend above a given flux with a coherent behavior? We propose a simple definition that can be used to jointly study the flux distribution and variability time scales of flares. We evaluate the duty cycle of AGN flares through simulations, assuming that the emission can be modeled as a red-noise, log-normal process.

2 Method

Long-term high-energy observations from *Fermi*-LAT reveal AGN light curves behaving as red-noise processes (Abdo et al. 2010). This means that the power spectral density (PSD) of the observed lightcurves follows a power-law spectrum as a function of frequency, $P(f) \sim f^{-\beta}$, where β is the index of the PSD and $P(f)$ is the power at frequency f . The average power-law index of FSRQs and BL Lacs was estimated by Abdo et al. (2010) to be $\beta = 1.4 \pm 0.1$ and $\beta = 1.7 \pm 0.3$, respectively.

The variations in flux are furthermore often found to have a log-normal distribution and the average amplitude of variability is proportional to the flux level (e.g. Giebels & Degrange 2009). The amplitude of flux variations is sometimes characterized by the fractional root mean square (rms) variability, F_{var} , which is an estimator of the rms flux divided by the average flux. TeV γ -ray observations of PKS 2155–304 by the High Energy Stereoscopic System (H.E.S.S.) for example displayed strong flux variability with fractional rms variations between $F_{\text{var}} = 0.13 \pm 0.09$ and $F_{\text{var}} = 0.67 \pm 0.03$ (Abramowski et al. 2010).

In the following, we simulate light curves from log-normal flux distributions based on red-noise processes, investigating $F_{\text{var}} = 0.1, 0.5$ and $\beta = 1, 2$ as test values. Timmer & Koenig (1995) propose a method for generating AGN light curves from a red-noise process. Here are the steps of our simulations:

(1) We construct a random PSD following a power-law spectrum of index β . We draw two normally distributed random numbers for each Fourier frequency f_i and multiply them by $\sqrt{P(f_i)}/2 \sim f_i^{-\beta/2}$. The results are used as the real part and imaginary part of the Fourier transform. Light curves are then generated through backward

¹ Institut de Physique Nucl aire d’Orsay, Universit  Paris-Sud, Univ. Paris/Saclay, CNRS/IN2P3, 91406 Orsay, France

Fourier transform. We notice that such simulations can be affected by windowing and aliasing effects (Uttley, McHardy & Papadakis 2002), but we do not consider these two effects at the early stage of this study.

(2) To get a log-normal distribution, we exponentiate the flux values, $\Phi_{TK}(t)$, from the light curve obtained with the method of Timmer & Koenig (1995), noting that small distortions of the PSD are expected. $\Phi_{TK}(t)$ represents here a red-noise Gaussian process with an average of 0 and variance of 1. We rescale $\Phi_{TK}(t)$ so that the average of Φ_t is set to 1 arbitrary units and its fractional rms amplitude is set to a value of F_{var} . We obtain the corresponding log-normally distributed random flux Φ_t , using two parameters μ and σ that are the mean and standard deviation of the natural logarithm of Φ_t :

$$\Phi_t = \exp(\mu + \sigma\Phi_{TK}(t)). \quad (2.1)$$

We set $\mu = -\frac{1}{2} \ln(1 + F_{\text{var}}^2)$ and $\sigma^2 = \ln(1 + F_{\text{var}}^2)$, which indeed results in $\langle \Phi_t \rangle = 1$ and $\sigma_{\Phi_t} / \langle \Phi_t \rangle = F_{\text{var}}$. In the method described above, only two parameters, β and F_{var} , are needed to fix the statistical characteristics of the light curves and therefore to describe the flare duty cycle.

For each lightcurve, we define flares above a given flux threshold as events for which the emission remains strictly above the threshold for a given duration. We collect the start and stop times of each flare for various realizations of the lightcurves and store the duration of each flare in a 2D histogram. We define the flare duty cycle as the ratio between the sum of flare durations and the light curve duration.

3 Results

Fig. 1, left, shows a single AGN light curve simulated as a pseudo-red-noise, log-normal process. We set $\beta = 2$ and $F_{\text{var}} = 0.5$ as an example that is in rough agreement with γ -ray observations from *Fermi*-LAT and H.E.S.S. We assume here an observation duration of 1 week, and a sampling of the flux every 0.5 hour.

Fig. 1, right, shows the flare duty cycle as a function of the flare duration and threshold flux obtained from simulations of 10^4 lightcurves, with the same β and F_{var} values as set to generate Fig. 1, left. We checked that integrating the 2D histogram over flare durations for given flux thresholds results in a 1D distribution compatible with the cumulative distribution function expected from a log-normal process.

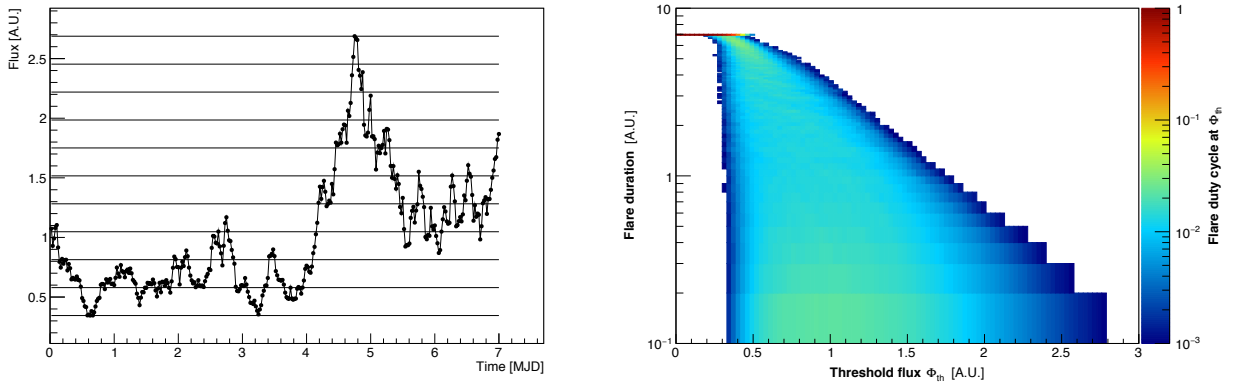


Fig. 1. Left: Example of a simulated light curve obtained with $F_{\text{var}} = 0.5$ and $\beta = 2$. Horizontal lines illustrate threshold fluxes above which the start and stop times of flaring events are collected. **Right:** Flare duty cycle obtained with $F_{\text{var}} = 0.5$ and $\beta = 2$.

3.1 Varying β and F_{var}

The distribution of flare duty cycle depends on β and F_{var} . The index of the PSD, β , reflects the ratio of long-term fluctuation power and short-term fluctuation power while the fractional rms variability, F_{var} , reflects the average amplitude of the variations.

In Fig. 2, left, we illustrate the duty cycle obtained with $\beta = 1$ and $F_{\text{var}} = 0.5$ for 10^4 simulations. In Fig. 2, right, we choose to illustrate the behavior of the duty cycle for $F_{\text{var}} = 0.1$ and $\beta = 2$.

(1) The comparison of Fig. 2, left, ($\beta = 1$) and Fig. 1, right, ($\beta = 2$), shows that for larger β values, the flare duty cycle covers a wider area of the flare duration – threshold flux plane. The interpretation is that, as β is

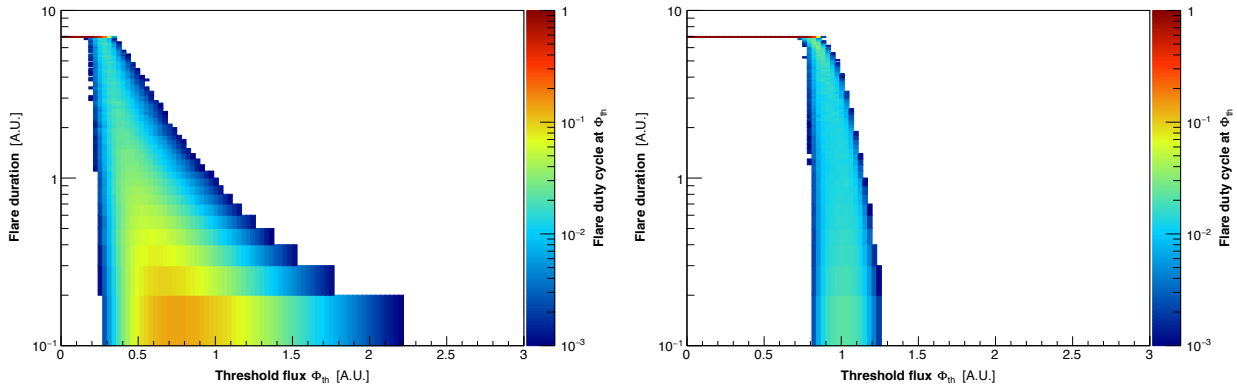


Fig. 2. Left: Flare duty cycle obtained with $F_{\text{var}} = 0.5$ and $\beta = 1$. **Right:** Flare duty cycle obtained with $F_{\text{var}} = 0.1$ and $\beta = 2$.

larger, more variability power is present at low frequencies. Long-duration flares are more frequent, and more time is given to build up large amplitude variations.

(2) The comparison of Fig. 2, right, ($F_{\text{var}} = 0.1$) and Fig. 1, right, ($F_{\text{var}} = 0.5$) also shows that for higher F_{var} , the flare duty cycle covers a wider area of the flare duration – threshold flux plane. The interpretation is that, as F_{var} is larger, the flux can vary in a larger range and spread out more. Larger amplitude flares build up, but the time scale distribution remains similar to that observed in Fig. 1, right.

3.2 Simulations with observation windows

Ground-based γ -ray observations from imaging atmospheric Cherenkov telescopes such as H.E.S.S., MAGIC, and VERITAS, are usually performed during dark, moonless nights, so that realistic light curves are affected by observation windows. We illustrate in Fig. 3 the effect of windowing on a single realization of a light curve from the method discussed in Sec. 2. The red points correspond to a 5-week-long lightcurve sampled on a 0.5-hour timescale, while the black points correspond to the subsample of observations falling within H.E.S.S. visibility, assuming a source located in the direction of PKS 2155–304. We follow the visibility definition of Giomi, Gerard & Maier (2016) and exploit the code from these authors, which is based on AstroPy (<http://www.astropy.org/>). In the example chosen here, PKS 2155–304 can only be observed by H.E.S.S. in blocks of 4–5 consecutive days.

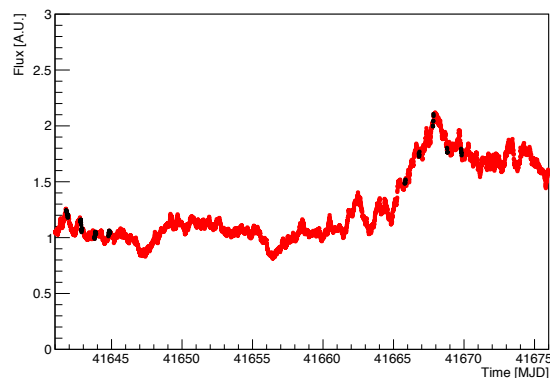


Fig. 3. Simulated light curve with $F_{\text{var}} = 2$ and $\beta = 0.5$ over a 5-week term (red points) with a 0.5-hour sampling. Black points illustrate the visibility of a given source by a ground-based γ -ray observatory.

Fig. 4, left, shows the flare duty cycle obtained by simulating 10^4 lightcurves with characteristics similar to the red curve in Fig. 3 (no windowing). Fig. 4, right, shows the flare duty cycle obtained by simulating the

same lightcurves affected by windowing, i.e. lightcurves similar to the black points in Fig. 3.

The mapping of the flare duty cycle is clearly affected by the observational windowing, with characteristic time scales imprinted directly in the 2D histogram. Further studies will be dedicated to understanding how the duty cycle is distorted by the observation schedule and to how one could optimize long-term monitoring campaigns to minimize biases inherent to the windowing, e.g. in the context of long-term observations with the Cherenkov Telescope Array.

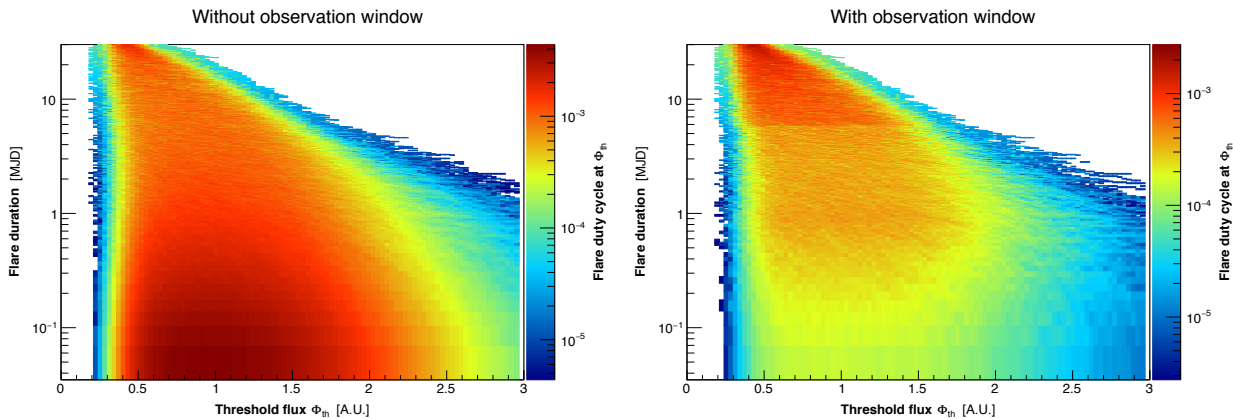


Fig. 4. Left: Flare duty cycle obtained with $F_{\text{var}} = 0.5$ and $\beta = 2$ for a 5-week-long lightcurve. No observation window is considered. **Right:** Flare duty cycle obtained with the same simulations applying the observation windows illustrated in Fig. 3.

4 Conclusions and outlook

We have adopted a simple definition of flaring events from AGNs to jointly investigate the flux distribution and variability timescales of pseudo-red-noise, log-normal processes. We summarized the main conclusions here:

(1) We can estimate the duty cycle for any fractional rms variability, F_{var} , and power spectral density index, β , as a function of the flare duration and threshold flux. All the flare information can be derived from these two parameters.

(2) Larger F_{var} values correspond to a wider range of flux variations, affecting the mapping of the flare duty cycle as a function of the threshold flux. Larger β values correspond to more power at low frequencies, resulting in longer flares as well as higher-amplitude flares, which have sufficient time to build up.

(3) The observational windowing affects the mapping of the duty cycle. Long-term monitoring campaigns could exploit tools such as presented in these proceedings to optimize the mapping of the duty cycle of AGN flares.

In the future, further developments for long-term γ -ray monitoring campaigns could include:

(1) A joint, unbiased, determination of F_{var} and β based on observations (e.g. from *Fermi*-LAT), focused on archetypal objects or populations.

(2) Simulations of long-term lightcurves to study more indepth the mapping of the duty cycle. Parallel computing appears to be a good solution to pursue such efforts.

The authors thank Matteo Giomi from DESY for the visibility code used in this study.

References

- Abdo, A. et al. 2010, ApJ, 722, 520
- Abramowski et al. 2010, A&A, 520, 83
- Giebels, B. & Degrange, B. 2009, A&A, 503, 797
- Giomi, M., Gerard, L., & Maier, G. 2016, APh, 80, 8
- Timmer, J., & Koenig, M. 1995, A&A, 300, 707
- Uttley P., McHardy I. & Papadakis I. 2002, MNRAS, 332, 231

Bibliography

- [1] A. Aab, P. Abreu, M. Aglietta, I. A. Samarai, I. F. M. Albuquerque, I. Allekotte, A. Almela, J. Alvarez Castillo, J. Alvarez-Muñiz, G. A. Anastasi, and et al. Combined fit of spectrum and composition data as measured by the Pierre Auger Observatory. *JCAP*, 4:038, April 2017. doi: 10.1088/1475-7516/2017/04/038. Cited on page 17.
- [2] A. A. Abdo, B. Allen, D. Berley, S. Casanova, C. Chen, D. G. Coyne, B. L. Dings, R. W. Ellsworth, L. Fleyscher, R. Fleyscher, M. M. Gonzalez, J. A. Goodman, E. Hays, C. M. Hoffman, B. Hopper, P. H. Hütemeyer, B. E. Kolterman, C. P. Lansdell, J. T. Linnemann, J. E. McEnery, A. I. Mincer, P. Nemethy, D. Noyes, J. M. Ryan, P. M. Saz Parkinson, A. Shoup, G. Sinnis, A. J. Smith, G. W. Sullivan, V. Vasileiou, G. P. Walker, D. A. Williams, X. W. Xu, and G. B. Yodh. TeV Gamma-Ray Sources from a Survey of the Galactic Plane with Milagro. *ApJL*, 664:L91–L94, August 2007. doi: 10.1086/520717. Cited on page 35.
- [3] A. A. Abdo, M. Ajello, and A. et al. Allafort. The Second Fermi Large Area Telescope Catalog of Gamma-Ray Pulsars. *ApJS*, 208:17, October 2013. doi: 10.1088/0067-0049/208/2/17. Cited on page 27.
- [4] J. Abraham, P. Abreu, M. Aglietta, C. Aguirre, D. Allard, I. Allekotte, J. Allen, P. Allison, J. Alvarez-Muñiz, M. Ambrosio, and et al. Observation of the Suppression of the Flux of Cosmic Rays above 4×10^{19} eV. *Physical Review Letters*, 101(6):061101, August 2008. doi: 10.1103/PhysRevLett.101.061101. Cited on page 17.
- [5] V. A. et al. Acciari. Measurement of the extragalactic background light using MAGIC and Fermi-LAT gamma-ray observations of blazars up to $z = 1$. *MNRAS*, 486:4233–4251, July 2019. doi: 10.1093/mnras/stz943. Cited on page 23.
- [6] F. Acero, M. Lemoine-Goumard, M. Renaud, J. Ballet, J. W. Hewitt, R. Rousseau, and T. Tanaka. Study of TeV shell supernova remnants at gamma-ray energies. *A&A*, 580:A74, August 2015. doi: 10.1051/0004-6361/201525932. Cited on page 50.
- [7] F. A. Aharonian. *Very high energy cosmic gamma radiation : a crucial window on the extreme Universe*. World Scientific Publishing Co, 2004. doi: 10.1142/4657. Cited on page 72.

- [8] F. A. Aharonian and A. M. Atoyan. Compton scattering of relativistic electrons in compact X-ray sources. *Ap&SS*, 79:321–336, October 1981. doi: 10.1007/BF00649428. Cited on page 73.
- [9] F. A. Aharonian, S. R. Kelner, and A. Y. Prosekin. Angular, spectral, and time distributions of highest energy protons and associated secondary gamma rays and neutrinos propagating through extragalactic magnetic and radiation fields. *PRD*, 82(4):043002, August 2010. doi: 10.1103/PhysRevD.82.043002. Cited on pages 71 and 74.
- [10] M. G. Baring, D. C. Ellison, S. P. Reynolds, I. A. Grenier, and P. Goret. Radio to Gamma-Ray Emission from Shell-Type Supernova Remnants: Predictions from Nonlinear Shock Acceleration Models. *ApJ*, 513:311–338, March 1999. doi: 10.1086/306829. Cited on page 71.
- [11] E. G. Berezhko and H. J. Völk. Kinetic theory of cosmic ray and gamma-ray production in supernova remnants expanding into wind bubbles. *A&A*, 357:283–300, May 2000. Cited on page 19.
- [12] E. G. Berezhko and H. J. Völk. Nonthermal and thermal emission from the supernova remnant RX J1713.7-3946. *A&A*, 511:A34, February 2010. doi: 10.1051/0004-6361/200913312. Cited on pages 98 and 99.
- [13] D. Berge, S. Funk, and J. Hinton. Background modelling in very-high-energy γ -ray astronomy. *A&A*, 466:1219–1229, May 2007. doi: 10.1051/0004-6361:20066674. Cited on page 45.
- [14] P. L. Biermann, N. Langer, Eun-Suk Seo, and T. Stanev. Cosmic rays IX. Interactions and transport of cosmic rays in the Galaxy. *A&A*, 369:269–277, Apr 2001. doi: 10.1051/0004-6361:20010083. Cited on page 18.
- [15] J. Biteau and D. A. Williams. The Extragalactic Background Light, the Hubble Constant, and Anomalies: Conclusions from 20 Years of TeV Gamma-ray Observations. *ApJ*, 812:60, October 2015. doi: 10.1088/0004-637X/812/1/60. Cited on page 23.
- [16] R. D. Blandford and J. P. Ostriker. Particle acceleration by astrophysical shocks. *ApJL*, 221:L29–L32, April 1978. doi: 10.1086/182658. Cited on page 19.
- [17] P. Blasi. The origin of galactic cosmic rays. *A&AR*, 21:70, November 2013. doi: 10.1007/s00159-013-0070-7. Cited on page 17.
- [18] G. R. Blumenthal and R. J. Gould. Bremsstrahlung, Synchrotron Radiation, and Compton Scattering of High-Energy Electrons Traversing Dilute Gases. *Reviews of Modern Physics*, 42:237–271, 1970. doi: 10.1103/RevModPhys.42.237. Cited on page 73.

- [19] R. Buehler. Space-based gamma-ray astronomy. In *34th International Cosmic Ray Conference (ICRC2015)*, volume 34 of *International Cosmic Ray Conference*, page 17, July 2015. Cited on page 21.
- [20] A. Bulgarelli, V. Fioretti, N. Parmiggiani, F. Verrecchia, C. Pittori, F. Lucarelli, M. Tavani, A. Aboudan, M. Cardillo, A. Giuliani, P. W. Cattaneo, A. W. Chen, G. Piano, A. Rappoldi, L. Baroncelli, A. Argan, L. A. Antonelli, I. Donnarumma, F. Gianotti, P. Giommi, M. Giusti, F. Longo, A. Pellizzoni, M. Pilia, M. Trifoglio, A. Trois, S. Vercellone, and A. Zoli. Second AGILE catalogue of gamma-ray sources. *A & A*, 627:A13, July 2019. doi: 10.1051/0004-6361/201834143. Cited on page 31.
- [21] A. Bykov, N. Gehrels, H. Krawczynski, M. Lemoine, G. Pelletier, and M. Pohl. Particle Acceleration in Relativistic Outflows. *SSR*, 173:309–339, November 2012. doi: 10.1007/s11214-012-9896-y. Cited on page 18.
- [22] A. M. Bykov. Nonthermal particles and photons in starburst regions and superbubbles. *A&AR*, 22:77, November 2014. doi: 10.1007/s00159-014-0077-8. Cited on page 18.
- [23] A. M. Bykov, D. C. Ellison, S. M. Osipov, and A. E. Vladimirov. Magnetic Field Amplification in Nonlinear Diffusive Shock Acceleration Including Resonant and Non-resonant Cosmic-Ray Driven Instabilities. *ApJ*, 789:137, July 2014. doi: 10.1088/0004-637X/789/2/137. Cited on page 96.
- [24] A. M. Bykov, D. C. Ellison, A. Marcowith, and S. M. Osipov. Cosmic Ray Production in Supernovae. *SSR*, 214:41, February 2018. doi: 10.1007/s11214-018-0479-4. Cited on page 99.
- [25] A. M. Bykov, F. Vazza, J. A. Kropotina, K. P. Levenfish, and F. B. S. Paerels. Shocks and Non-thermal Particles in Clusters of Galaxies. *SSR*, 215:14, February 2019. doi: 10.1007/s11214-019-0585-y. Cited on page 18.
- [26] D. Caprioli, E. Amato, and P. Blasi. The contribution of supernova remnants to the galactic cosmic ray spectrum. *Astroparticle Physics*, 33:160–168, April 2010. doi: 10.1016/j.astropartphys.2010.01.002. Cited on page 18.
- [27] G. L. Case and D. Bhattacharya. A New Σ -D Relation and Its Application to the Galactic Supernova Remnant Distribution. *ApJ*, 504:761–772, September 1998. doi: 10.1086/306089. Cited on page 51.
- [28] G. Castelletti, L. Supan, G. Dubner, B. C. Joshi, and M. P. Surnis. A hadronic scenario for HESS J1818-154. *A&A*, 557:L15, September 2013. doi: 10.1051/0004-6361/201322350. Cited on page 51.

- [29] K. S. Cheng, C. Ho, and M. Ruderman. Energetic radiation from rapidly spinning pulsars. I - Outer magnetosphere gaps. II - VELA and Crab. *ApJ*, 300:500–539, January 1986. doi: 10.1086/163829. Cited on page 27.
- [30] Fermi LAT Collaboration. The Fermi-LAT High-Latitude Survey: Source Count Distributions and the Origin of the Extragalactic Diffuse Background. *ApJ*, 720:435–453, September 2010. doi: 10.1088/0004-637X/720/1/435. Cited on page 27.
- [31] Fermi-LAT Collaboration. The Second Catalog of Flaring Gamma-Ray Sources from the Fermi All-sky Variability Analysis. *ApJ*, 846(1):34, Sep 2017. doi: 10.3847/1538-4357/aa8092. Cited on page 23.
- [32] H. E. S. S. Collaboration. Discovery of very high energy gamma-ray emission coincident with molecular clouds in the W 28 (G6.4-0.1) field. *A&A*, 481:401–410, April 2008. doi: 10.1051/0004-6361:20077765. Cited on pages 51 and 77.
- [33] H. E. S. S. Collaboration. Exploring a SNR/molecular cloud association within HESS J1745-303. *A&A*, 483:509–517, May 2008. doi: 10.1051/0004-6361:20079230. Cited on page 77.
- [34] H. E. S. S. Collaboration. Discovery of very-high-energy γ -ray emission from the vicinity of PSR J1913+1011 with HESS. *A&A*, 484:435–440, June 2008. doi: 10.1051/0004-6361:20078715. Cited on page 77.
- [35] H. E. S. S. Collaboration. A new SNR with TeV shell-type morphology: HESS J1731-347. *A&A*, 531:A81, July 2011. doi: 10.1051/0004-6361/201016425. Cited on pages 77 and 83.
- [36] H. E. S. S. Collaboration. H.E.S.S. detection of TeV emission from the interaction region between the supernova remnant G349.7+0.2 and a molecular cloud. *A&A*, 574:A100, January 2015. doi: 10.1051/0004-6361/201425070. Cited on page 51.
- [37] HAWC Collaboration. Observation of the Crab Nebula with the HAWC Gamma-Ray Observatory. *ApJ*, 843:39, July 2017. doi: 10.3847/1538-4357/aa7555. Cited on page 29.
- [38] HAWC Collaboration. All-particle cosmic ray energy spectrum measured by the HAWC experiment from 10 to 500 TeV. *PRD*, 96(12):122001, December 2017. doi: 10.1103/PhysRevD.96.122001. Cited on page 29.
- [39] H.E.S.S. Collaboration. Diffuse Galactic gamma-ray emission with H.E.S.S. *PRD*, 90(12):122007, December 2014. doi: 10.1103/PhysRevD.90.122007. Cited on page 27.
- [40] MAGIC Collaboration. Morphological and spectral properties of the W51 region measured with the MAGIC telescopes. *A&A*, 541:A13, May 2012. doi: 10.1051/0004-6361/201218846. Cited on page 89.

- [41] The Fermi-LAT Collaboration. A detailed spectral and morphological study of the gamma-ray supernova remnant RX J1713.7-3946 with HESS. *A&A*, 449:223–242, April 2006. doi: 10.1051/0004-6361:20054279. Cited on page 51.
- [42] The Fermi-LAT collaboration. Fermi LAT Discovery of Extended Gamma-Ray Emission in the Direction of Supernova Remnant W51C. *ApJL*, 706:L1–L6, November 2009. doi: 10.1088/0004-637X/706/1/L1. Cited on page 89.
- [43] The Fermi-LAT Collaboration. Fermi Large Area Telescope Observations of the Supernova Remnant W28 (G6.4-0.1). *ApJ*, 718:348–356, July 2010. doi: 10.1088/0004-637X/718/1/348. Cited on pages 77 and 88.
- [44] The Fermi-LAT collaboration. Fermi-LAT Study of Gamma-ray Emission in the Direction of Supernova Remnant W49B. *ApJ*, 722:1303–1311, October 2010. doi: 10.1088/0004-637X/722/2/1303. Cited on pages 77 and 84.
- [45] The Fermi-LAT Collaboration. Gamma-Ray Emission from the Shell of Supernova Remnant W44 Revealed by the Fermi LAT. *Science*, 327:1103, February 2010. doi: 10.1126/science.1182787. Cited on page 50.
- [46] The Fermi-LAT collaboration. Observations of the Young Supernova Remnant RX J1713.7-3946 with the Fermi Large Area Telescope. *ApJ*, 734:28, June 2011. doi: 10.1088/0004-637X/734/1/28. Cited on page 99.
- [47] The Fermi-LAT Collaboration. The First Fermi LAT Supernova Remnant Catalog. *ApJS*, 224:8, May 2016. doi: 10.3847/0067-0049/224/1/8. Cited on pages 24, 25, and 51.
- [48] The Fermi-LAT collaboration. Fermi Large Area Telescope Fourth Source Catalog. *arXiv:1902.10045*, February 2019. Cited on pages 21 and 25.
- [49] The Fermi-LAT collaboration. The Fourth Catalog of Active Galactic Nuclei Detected by the Fermi Large Area Telescope. *arXiv:1905.10771*, art. arXiv:1905.10771, May 2019. Cited on page 23.
- [50] B. Condon, M. Lemoine-Goumard, F. Acero, and H. Katagiri. Detection of Two TeV Shell-type Remnants at GeV Energies with FERMI LAT: HESS J1731-347 and SN 1006. *ApJ*, 851:100, December 2017. doi: 10.3847/1538-4357/aa9be8. Cited on pages 77 and 83.
- [51] CTA Consortium. *Science with the Cherenkov Telescope Array*. World Scientific Publishing Co, 2019. doi: 10.1142/10986. Cited on pages 27, 28, and 82.
- [52] Y. Cui, P. K. H. Yeung, P. H. T. Tam, and G. Pühlhofer. Leaked GeV CRs from a Broken Shell: Explaining 9 Years of Fermi-LAT Data of SNR W28. *ApJ*, 860:69, June 2018. doi: 10.3847/1538-4357/aac37b. Cited on pages 77 and 87.

- [53] A. De Angelis. (Very)-high-energy gamma-ray astrophysics: The future. In *European Physical Journal Web of Conferences*, volume 116 of *European Physical Journal Web of Conferences*, page 11012, April 2016. doi: 10.1051/epjconf/201611611012. Cited on page 37.
- [54] M. de Naurois and D. Mazin. Ground-based detectors in very-high-energy gamma-ray astronomy. *Comptes Rendus Physique*, 16:610–627, August 2015. doi: 10.1016/j.crhy.2015.08.011. Cited on page 21.
- [55] A. Desai, K. Helgason, M. Ajello, V. Paliya, A. Domínguez, J. Finke, and D. Hartmann. A GeV-TeV Measurement of the Extragalactic Background Light. *ApJL*, 874:L7, March 2019. doi: 10.3847/2041-8213/ab0c10. Cited on page 23.
- [56] G. Di Sciascio. Ground-based Gamma-Ray Astronomy: an Introduction. In *Journal of Physics Conference Series*, volume 1263 of *Journal of Physics Conference Series*, page 012003, June 2019. doi: 10.1088/1742-6596/1263/1/012003. Cited on pages 35 and 38.
- [57] A. Donath, C. Deil, M. P. Arribas, J. King, E. Owen, R. Terrier, I. Reichardt, J. Harris, R. Buehler, and S. Klepser. Gammapy: An open-source Python package for gamma-ray astronomy. In *34th International Cosmic Ray Conference (ICRC2015)*, volume 34 of *International Cosmic Ray Conference*, page 789, July 2015. Cited on page 43.
- [58] V. Doroshenko, G. Pühlhofer, A. Bamba, F. Acero, W. W. Tian, D. Klochkov, and A. Santangelo. XMM-Newton observations of the non-thermal supernova remnant HESS J1731-347 (G353.6-0.7). *A&A*, 608:A23, December 2017. doi: 10.1051/0004-6361/201730983. Cited on pages 77 and 83.
- [59] D. C. Ellison, D. J. Patnaude, P. Slane, and J. Raymond. Efficient Cosmic Ray Acceleration, Hydrodynamics, and Self-Consistent Thermal X-Ray Emission Applied to Supernova Remnant RX J1713.7-3946. *ApJ*, 712:287–293, March 2010. doi: 10.1088/0004-637X/712/1/287. Cited on pages 71, 98, and 99.
- [60] J. Fang and L. Zhang. On the non-thermal emission from the supernova remnant W51C. *MNRAS*, 405:462–466, June 2010. doi: 10.1111/j.1365-2966.2010.16455.x. Cited on pages 77 and 89.
- [61] S. Federici, M. Pohl, I. Telezhinsky, A. Wilhelm, and V. V. Dwarkadas. Analysis of GeV-band γ -ray emission from supernova remnant RX J1713.7-3946. *A&A*, 577:A12, May 2015. doi: 10.1051/0004-6361/201424947. Cited on pages 77 and 82.
- [62] E. Fermi. On the Origin of the Cosmic Radiation. *Physical Review*, 75:1169–1174, April 1949. doi: 10.1103/PhysRev.75.1169. Cited on page 19.

- [63] G. Ferrand, A. Decourchelle, and S. Safi-Harb. Three-dimensional Simulations of the Thermal X-Ray Emission from Young Supernova Remnants Including Efficient Particle Acceleration. *ApJ*, 760:34, November 2012. doi: 10.1088/0004-637X/760/1/34. Cited on page 71.
- [64] J. D. Finke, L. C. Reyes, M. Georganopoulos, K. Reynolds, M. Ajello, S. J. Fegan, and K. McCann. Constraints on the Intergalactic Magnetic Field with Gamma-Ray Observations of Blazars. *ApJ*, 814:20, November 2015. doi: 10.1088/0004-637X/814/1/20. Cited on page 23.
- [65] D. Foreman-Mackey, D. W. Hogg, D. Lang, and J. Goodman. emcee: The MCMC Hammer. *PASP*, 125:306, March 2013. doi: 10.1086/670067. Cited on page 81.
- [66] Y. Fukui, Y. Moriguchi, K. Tamura, H. Yamamoto, Y. Tawara, N. Mizuno, T. Onishi, A. Mizuno, Y. Uchiyama, J. Hiraga, T. Takahashi, K. Yamashita, and S. Ikeuchi. Discovery of Interacting Molecular Gas toward the TeV Gamma-Ray Peak of the SNR G 347.3–0.5. *PASJ*, 55:L61–L64, October 2003. doi: 10.1093/pasj/55.5.L61. Cited on page 52.
- [67] S. Funk. Ground- and Space-Based Gamma-Ray Astronomy. *Annual Review of Nuclear and Particle Science*, 65:245–277, October 2015. doi: 10.1146/annurev-nucl-102014-022036. Cited on page 21.
- [68] J. A. Gaunt. Continuous Absorption. *Philosophical Transactions of the Royal Society of London Series A*, 229:163–204, 1930. doi: 10.1098/rsta.1930.0005. Cited on page 72.
- [69] K. Greisen. End to the Cosmic-Ray Spectrum? *Physical Review Letters*, 16:748–750, April 1966. doi: 10.1103/PhysRevLett.16.748. Cited on page 18.
- [70] I. A. Grenier, J. H. Black, and A. W. Strong. The Nine Lives of Cosmic Rays in Galaxies. *ARA&A*, 53:199–246, August 2015. doi: 10.1146/annurev-astro-082214-122457. Cited on page 17.
- [71] X.-L. Guo, Y.-L. Xin, N.-H. Liao, Q. Yuan, W.-H. Gao, and Y.-Z. Fan. Detection of GeV Gamma-Ray Emission in the Direction of HESS J1731-347 with Fermi-LAT. *ApJ*, 853:2, January 2018. doi: 10.3847/1538-4357/aaa3f8. Cited on pages 83 and 100.
- [72] H. E. S. S. Collaboration, H. Abdalla, A. Abramowski, F. Aharonian, F. Ait Benkhali, E. O. Angüner, M. Arakawa, M. Arrieta, P. Aubert, M. Backes, and et al. Population study of Galactic supernova remnants at very high γ -ray energies with H.E.S.S. *A&A*, 612:A3, April 2018. doi: 10.1051/0004-6361/201732125. Cited on pages 25 and 26.
- [73] W. Heitler. *Dover Publications*. Cambridge University Press, 1954. Cited on page 32.

- [74] H.E.S.S. Collaboration, H. Abdalla, A. Abramowski, F. Aharonian, F. Ait Benkhali, A. G. Akhperjanian, T. Andersson, E. O. Angüner, M. Arakawa, M. Arrieta, and et al. A search for new supernova remnant shells in the Galactic plane with H.E.S.S. *A&A*, 612:A8, April 2018. doi: 10.1051/0004-6361/201730737. Cited on page 91.
- [75] H.E.S.S. Collaboration, H. Abdalla, A. Abramowski, F. Aharonian, F. Ait Benkhali, A. G. Akhperjanian, T. Andersson, E. O. Angüner, M. Arrieta, P. Aubert, and et al. The supernova remnant W49B as seen with H.E.S.S. and Fermi-LAT. *A&A*, 612:A5, April 2018. doi: 10.1051/0004-6361/201527843. Cited on pages 77 and 84.
- [76] H.E.S.S. Collaboration, H. Abdalla, A. Abramowski, F. Aharonian, F. Ait Benkhali, E. O. Angüner, M. Arakawa, M. Arrieta, P. Aubert, M. Backes, and et al. The H.E.S.S. Galactic plane survey. *A&A*, 612:A1, April 2018. doi: 10.1051/0004-6361/201732098. Cited on pages 22 and 23.
- [77] A. M. Hillas. Cerenkov light images of EAS produced by primary gamma. *International Cosmic Ray Conference*, 3, August 1985. Cited on pages 36 and 37.
- [78] C. Y. Hui, E. M. H. Wu, J. H. K. Wu, R. H. H. Huang, K. S. Cheng, P. H. T. Tam, and A. K. H. Kong. Exploring the Dark Accelerator HESS J1745-303 with the Fermi Large Area Telescope. *ApJ*, 735:115, July 2011. doi: 10.1088/0004-637X/735/2/115. Cited on pages 77 and 86.
- [79] E. Kafexhiu, F. Aharonian, A. M. Taylor, and G. S. Vila. Parametrization of gamma-ray production cross sections for p p interactions in a broad proton energy range from the kinematic threshold to PeV energies. *PRD*, 90(12):123014, December 2014. doi: 10.1103/PhysRevD.90.123014. Cited on pages 71 and 74.
- [80] T. Kamae, N. Karlsson, T. Mizuno, T. Abe, and T. Koi. Parameterization of γ , $e^{+/-}$, and Neutrino Spectra Produced by p-p Interaction in Astronomical Environments. *ApJ*, 647: 692–708, August 2006. doi: 10.1086/505189. Cited on page 74.
- [81] S. Katsuda, F. Acero, N. Tominaga, Y. Fukui, J. S. Hiraga, K. Koyama, S.-H. Lee, K. Mori, S. Nagataki, Y. Ohira, R. Petre, H. Sano, Y. Takeuchi, T. Tamagawa, N. Tsuji, H. Tsunemi, and Y. Uchiyama. Evidence for Thermal X-Ray Line Emission from the Synchrotron-dominated Supernova Remnant RX J1713.7-3946. *ApJ*, 814:29, November 2015. doi: 10.1088/0004-637X/814/1/29. Cited on page 71.
- [82] S. R. Kelner, F. A. Aharonian, and V. V. Bugayov. Energy spectra of gamma rays, electrons, and neutrinos produced at proton-proton interactions in the very high energy regime. *PRD*, 74(3):034018, August 2006. doi: 10.1103/PhysRevD.74.034018. Cited on page 74.

- [83] D. Khangulyan, F. A. Aharonian, and S. R. Kelner. Simple Analytical Approximations for Treatment of Inverse Compton Scattering of Relativistic Electrons in the Blackbody Radiation Field. *ApJ*, 783:100, March 2014. doi: 10.1088/0004-637X/783/2/100. Cited on pages 71, 73, and 74.
- [84] J. Knödlseder, M. Mayer, C. Deil, J.-B. Cayrou, E. Owen, N. Kelley-Hoskins, C.-C. Lu, R. Buehler, F. Forest, T. Louge, H. Siejkowski, K. Kosack, L. Gerard, A. Schulz, P. Martin, D. Sanchez, S. Ohm, T. Hassan, and S. Brau-Nogu e. GammaLib and ctools. A software framework for the analysis of astronomical gamma-ray data. *A&A*, 593:A1, August 2016. doi: 10.1051/0004-6361/201628822. Cited on pages 43 and 45.
- [85] K. Kotera and A. V. Olinto. The Astrophysics of Ultrahigh-Energy Cosmic Rays. *ARA&A*, 49:119–153, September 2011. doi: 10.1146/annurev-astro-081710-102620. Cited on pages 17 and 18.
- [86] J. S. Lazendic, M. Wardle, J. B. Whiteoak, M. G. Burton, and A. J. Green. Multiwavelength observations of the supernova remnant G349.7+0.2 interacting with a molecular cloud. *MNRAS*, 409:371–388, November 2010. doi: 10.1111/j.1365-2966.2010.17315.x. Cited on page 50.
- [87] M. Lemoine-Goumard. Ground-based gamma-ray astronomy. In *34th International Cosmic Ray Conference (ICRC2015)*, volume 34 of *International Cosmic Ray Conference*, page 12, July 2015. Cited on page 21.
- [88] M. Lemoine-Goumard, B. Degrange, and M. Tluczykont. Selection and 3D-reconstruction of gamma-ray-induced air showers with a stereoscopic system of atmospheric Cherenkov telescopes. *Astroparticle Physics*, 25:195–211, April 2006. doi: 10.1016/j.astropartphys.2006.01.005. Cited on page 37.
- [89] M. Lisanti, S. Mishra-Sharma, L. Necib, and B. R. Safdi. Deciphering Contributions to the Extragalactic Gamma-Ray Background from 2 GeV to 2 TeV. *ApJ*, 832:117, December 2016. doi: 10.3847/0004-637X/832/2/117. Cited on page 27.
- [90] M. S. Longair. *High Energy Astrophysics*. Cambridge University Press, February 2011. Cited on pages 19 and 72.
- [91] E. Lorenz and R. Wagner. Very-high energy gamma-ray astronomy. A 23-year success story in high-energy astroparticle physics. *European Physical Journal H*, 37:459–513, August 2012. doi: 10.1140/epjh/e2012-30016-x. Cited on pages 33 and 36.
- [92] T. A. Lozinskaya. The radio brightness-diameter relation for supernova remnants - Some new distance calibrators. *Soviet Astronomy Letters*, 7:29–32, February 1981. Cited on page 52.

- [93] J. Matthews. A Heitler model of extensive air showers. *Astroparticle Physics*, 22:387–397, January 2005. doi: 10.1016/j.astropartphys.2004.09.003. Cited on pages 32 and 33.
- [94] N. Maxted, M. Burton, C. Braiding, G. Rowell, H. Sano, F. Voisin, M. Capasso, G. Pühlhofer, and Y. Fukui. Probing the local environment of the supernova remnant HESS J1731-347 with CO and CS observations. *MNRAS*, 474:662–676, February 2018. doi: 10.1093/mnras/stx2727. Cited on pages 51 and 52.
- [95] M. Meyer, J. Conrad, and H. Dickinson. Sensitivity of the Cherenkov Telescope Array to the Detection of Intergalactic Magnetic Fields. *ApJ*, 827:147, August 2016. doi: 10.3847/0004-637X/827/2/147. Cited on page 23.
- [96] A. Neronov, D. Malyshev, M. Chernyakova, and A. Lutovinov. Search for variable gamma-ray emission from the Galactic plane in the Fermi data. *A&A*, 543:L9, July 2012. doi: 10.1051/0004-6361/201219420. Cited on page 88.
- [97] L. O’C. Drury, F. A. Aharonian, D. Malyshev, and S. Gabici. On the plasma temperature in supernova remnants with cosmic-ray modified shocks. *A&A*, 496:1–6, March 2009. doi: 10.1051/0004-6361/200811394. Cited on page 100.
- [98] E. N. Parker. Galactic Effects of the Cosmic-Ray Gas. *SSR*, 9:651–712, August 1969. doi: 10.1007/BF00174032. Cited on page 29.
- [99] J. S. Perkins. ICRC Rapporteur: Space Based Gamma-ray Astronomy. *International Cosmic Ray Conference*, 35:1117, January 2017. Cited on page 21.
- [100] V. Ptuskin, V. Zirakashvili, and E.-S. Seo. Spectrum of Galactic Cosmic Rays Accelerated in Supernova Remnants. *ApJ*, 718:31–36, July 2010. doi: 10.1088/0004-637X/718/1/31. Cited on page 19.
- [101] S. Ranasinghe and D. A. Leahy. Revised Distances to 21 Supernova Remnants. *AJ*, 155:204, May 2018. doi: 10.3847/1538-3881/aab9be. Cited on pages 51 and 52.
- [102] W. Reich and X.-H. Sun. Polarised radio emission associated with HESS J1912+101. *Research in Astronomy and Astrophysics*, 19:045, March 2019. doi: 10.1088/1674-4527/19/3/45. Cited on pages 51 and 91.
- [103] Y. Su, X. Zhou, J. Yang, Y. Chen, X. Chen, Y. Gong, and S. Zhang. Is HESS J1912+101 Associated with an Old Supernova Remnant? *ApJ*, 845:48, August 2017. doi: 10.3847/1538-4357/aa7f2a. Cited on pages 52 and 91.
- [104] L. G. Sveshnikova. The knee in the Galactic cosmic ray spectrum and variety in Supernovae. *A&A*, 409:799–807, Oct 2003. doi: 10.1051/0004-6361:20030909. Cited on page 18.

- [105] T. Tanaka, Y. Uchiyama, F. A. Aharonian, T. Takahashi, A. Bamba, J. S. Hiraga, J. Kataoka, T. Kishishita, M. Kokubun, K. Mori, K. Nakazawa, R. Petre, H. Tajima, and S. Watanabe. Study of Nonthermal Emission from SNR RX J1713.7-3946 with Suzaku. *ApJ*, 685: 988–1004, October 2008. doi: 10.1086/591020. Cited on pages 75, 77, and 82.
- [106] T. Tanaka, H. Yamaguchi, D. R. Wik, F. A. Aharonian, A. Bamba, D. Castro, A. R. Foster, R. Petre, J. Rho, R. K. Smith, H. Uchida, Y. Uchiyama, and B. J. Williams. NuSTAR Detection of Nonthermal Bremsstrahlung from the Supernova Remnant W49B. *ApJL*, 866:L26, October 2018. doi: 10.3847/2041-8213/aae709. Cited on pages 77 and 84.
- [107] W. W. Tian and D. A. Leahy. The radio SNR G65.1+0.6 and its associated pulsar J1957+2831. *A&A*, 455:1053–1058, September 2006. doi: 10.1051/0004-6361:20065140. Cited on page 51.
- [108] W. W. Tian and D. A. Leahy. Distances of the TeV supernova remnant complex CTB 37 towards the Galactic bar. *MNRAS*, 421:2593–2597, April 2012. doi: 10.1111/j.1365-2966.2012.20491.x. Cited on page 51.
- [109] Y. Tsubone, M. Sawada, A. Bamba, S. Katsuda, and J. Vink. A Systematic Study of the Thermal and Nonthermal Emission in the Supernova Remnant RCW 86 with Suzaku. *ApJ*, 835:34, January 2017. doi: 10.3847/1538-4357/835/1/34. Cited on page 71.
- [110] Y. Uchiyama, F. A. Aharonian, T. Tanaka, T. Takahashi, and Y. Maeda. Extremely fast acceleration of cosmic rays in a supernova remnant. *Nature*, 449:576–578, October 2007. doi: 10.1038/nature06210. Cited on page 99.
- [111] P. F. Velázquez, G. M. Dubner, W. M. Goss, and A. J. Green. Investigation of the Large-scale Neutral Hydrogen near the Supernova Remnant W28. *AJ*, 124:2145–2151, October 2002. doi: 10.1086/342936. Cited on page 51.
- [112] T. M. Venters. Contribution to the Extragalactic Gamma-Ray Background from the Cascades of very High Energy Gamma Rays from Blazars. *ApJ*, 710:1530–1540, February 2010. doi: 10.1088/0004-637X/710/2/1530. Cited on page 20.
- [113] H. J. Völk and V. N. Zirakashvili. Cosmic ray acceleration by spiral shocks in the galactic wind. *A&A*, 417:807–817, April 2004. doi: 10.1051/0004-6361:20040018. Cited on page 19.
- [114] C. Winkler, R. Diehl, P. Ubertini, and J. Wilms. INTEGRAL: Science Highlights and Future Prospects. *SSR*, 161:149–177, November 2011. doi: 10.1007/s11214-011-9846-0. Cited on page 31.

- [115] R.-z. Yang, X. Zhang, Q. Yuan, and S. Liu. Fermi Large Area Telescope observations of the supernova remnant HESS J1731-347. *A&A*, 567:A23, July 2014. doi: 10.1051/0004-6361/201322737. Cited on page 83.
- [116] Q. Yuan, S. Liu, and X. Bi. An Attempt at a Unified Model for the Gamma-Ray Emission of Supernova Remnants. *ApJ*, 761:133, December 2012. doi: 10.1088/0004-637X/761/2/133. Cited on page 85.
- [117] V. Zabalza. Naima: a Python package for inference of particle distribution properties from nonthermal spectra. In A. S. Borisov, V. G. Denisova, Z. M. Guseva, E. A. Kanevskaya, M. G. Kogan, A. E. Morozov, V. S. Puchkov, S. E. Pyatovsky, G. P. Shoziyoev, M. D. Smirnova, A. V. Vargasov, V. I. Galkin, S. I. Nazarov, and R. A. Mukhamedshin, editors, *34th International Cosmic Ray Conference (ICRC2015)*, volume 34 of *International Cosmic Ray Conference*, page 922, July 2015. Cited on pages 71 and 74.
- [118] G. T. Zatsepin and V. A. Kuz'min. Upper Limit of the Spectrum of Cosmic Rays. *Soviet Journal of Experimental and Theoretical Physics Letters*, 4:78, August 1966. Cited on page 18.

Titre : Restes de supernova comme candidats PeVatrons: analyse et modélisation de données simulées de Cherenkov Telescope Array

Les rayons cosmiques (CRS) contiennent des informations sur les processus les plus puissants de l'univers. La spectrométrie des CRS de 10^{20} eV a été mesurée avec une grande précision. Il y a une rupture dans le spectre des particules entières autour de PeV (10^{15} eV), appelée "genou". L'origine de l'articulation du genou dans le spectre PeV reste un problème en suspens. Grâce à son budget énergétique considérable, le site Supernova (SNR) est le candidat potentiel de ces prétendus PeVatron.

Les CRS sont des particules chargées qui sont déviées par le champ magnétique, ce qui entraîne la perte d'informations de direction de la source. Les particules chargées sont accélérées pour produire un rayonnement électromagnétique. Limiter la distribution d'énergie du rayonnement électromagnétique est la clef de l'accélération des particules chargées de la matrice. Dans le spectre électromagnétique, les rayons gamma ultra-haute énergie (VHE) (30 GeV à 300 TeV) ouvrent la "dernière fenêtre".

Les particules chargées accélérées interagissent avec la substance environnante pour produire des particules neutres de particules de pidium qui se désintègrent en rayons gamma haute énergie. Ces rayons gamma peuvent ensuite être détectés par le télescope de Cherenkov ou par d'autres observatoires gamma à l'énergie TeV de PeVatron. Ici, nous avons étudié le potentiel du réseau de télescopes

de Cherenkov (CTA) pour l'observation de ces rayons gamma.

Le télescope CTA est encore en construction et il n'a pas encore été produit de données réelles. En conséquence, les données du défi 1 (DC-1) de la modélisation de la CTA ont été utilisées pour préparer la science de la CTA. Après avoir sélectionné la candidature de PeVatron, galaxie potentielle dans le DC-1 analogique de la CTA, nous avons reconstruit leur distribution d'énergie spectrale (SED) avec des paquets Tools. Après analyse des données de DC-1 analogiques, nous avons construit le sed à large bande du candidat de PeVatron de la galaxie sélectionné à l'aide des données de longueurs d'onde multiples (MWL). Ensuite, nous avons mis en correspondance les modèles Light-strong, pur-light et pur-strong dans les données MWL.

En comparant les différents modèles de rayonnement, on détermine si le procédé léger ou le processus fort permet de contrôler le rayonnement du SNR de la galaxie sélectionnée. Les calculs de modélisation sont effectués à l'aide du logiciel Naima et sont alignés sur le SEDs.

La capacité d'arrêt des protons est un paramètre essentiel pour déterminer si le SNR souhaite devenir candidat de PeVatron (c'est-à-dire que lorsque la limite des protons de la source est supérieure à 1 PeV, la source peut accélérer les protons jusqu'à l'énergie de PeV, ce qui indique que la source est un candidat de PeVatron). Nous avons présenté les résultats MWL des sources de rayonnement, examiné les résultats obtenus et expliqué comment les données DC-1, combinées à d'autres données sur les longueurs d'onde, pouvaient être utilisées pour limiter ce modèle.

S'il existe d'autres mesures de longueurs d'onde, nous les combinons avec les SEDs analogiques pour l'analyse MWL. Les SEDs sont ensuite affinés à l'aide de différents modèles de rayonnement non thermique mis en oeuvre dans le boîtier de Naima, y compris des sous-ensembles diélectriques pipi à neutrons solides.

Trois mécanismes de rayonnement potentiel pour l'émission de rayons GeV-TeV gamma pour les SNRs: diffusion de photons par des électrons à haute énergie, connue sous le nom de diffusion de Compton inverse; rayonnement télescopique résultant de l'interaction d'électrons relativistes et d'ions; collision entre protons et protons (PP), entraînant la production de pions et la production de rayons gamma. En outre, le rayonnement de synchronisation peut être utilisé pour affiner des spectres photoniques à faible

énergie (radioélectricité et rayons X) afin de limiter le champ magnétique et le spectre électronique.

Différents modèles de rayonnement décrivent les interactions entre les particules et l'environnement (champ magnétique, champ photonique, particule). Le rayonnement particulaire est un rayonnement non thermique, ce qui signifie que le rayonnement continu produit par la distribution des particules est un spectre d'énergie non Maxwellian.

Plusieurs résultats ont été obtenus. Les paramètres spectraux reconstruits sont identiques à ceux du DC-1. La simulation peut donc inspirer confiance au processus d'analyse des données. Des candidats potentiels de PeVatron ayant un spectre d'énergie dur ont été identifiés dans le SNR étudié. Les résultats montrent également que les données MWL ont un bon effet restrictif sur la modélisation SED et permettent de déterminer s'il y a des composants de Hadron dans les données. Si le spectre SNR observé par la CTA correspond à la simulation DC-1, on peut exclure la plupart des sources PeVatrons. Dans le même temps, la combinaison des données Fermi-LAT et CTA permettra de limiter ou de mesurer strictement la contribution relative des hadrons et des légers aux émissions de rayons SNR gamma. Des améliorations possibles ont été apportées à la modélisation du spectre d'entrée pour répondre au défi posé par les données pour la prochaine étape de la CTA.

À l'évidence, pour les environnements à haute densité (par exemple, les systèmes SNR-MC), les émissions de rayons gamma devraient être dominées par les Pi, car ces

environnements contiennent davantage d'objectifs protoniques. Il convient de noter que la plupart des SNR du système SNR-MC sont des personnes âgées. Avec l'augmentation du champ magnétique, l'élément ci est supprimé en raison de la réduction du nombre d'électrons dans un flux de rayonnement synchrone donné. Dans ce cas, il est nécessaire d'augmenter le nombre de chromes pour expliquer le flux gamma observé.

Bien que la CTA soit un appareil à rayons gamma qui possède des informations essentielles pour accélérer l'énergie maximale des particules, les données MWL (par exemple, l'observation des rayons X) sont également importantes pour l'étude des particules candidates de PeVatron. En particulier, les données relatives aux rayons X peuvent être utilisées de la manière suivante. Tout d'abord, dans l'analyse morphologique, le SNR, qui a une forte corrélation entre les rayons GeV et TeV gamma, suggère qu'une source légère possible d'émission est émise. Deuxièmement, l'absence d'émission de rayons X thermiques signifie une faible densité gazeuse. Par conséquent, la teneur en énergie des protons d'accélération devrait être élevée dans le modèle de particules à rayons gamma TeV.

L'amplification du champ magnétique est un phénomène important par rapport au signal-bruit du système SNR-MC. En outre, lorsque le SNR n'a pas d'impact de collision, il est possible d'accélérer efficacement les particules, ce qui entraîne une instabilité du flux de CRs, L'amplification du champ magnétique peut également se produire.

Les paramètres restructurés correspondent mieux aux résultats de la simulation d'entrée, ce qui témoigne de la robustesse de l'outil d'analyse. Néanmoins, nous avons constaté des défauts importants dans certains objets qui sont soupçonnés d'avoir été provoqués par la modélisation du champ de vision. Le processus d'affinage ne contient que la source lumineuse la plus lumineuse, de sorte que la pollution provenant de plusieurs objets faibles peut entraîner une déviation par rapport au modèle réel. L'inventaire de l'ensemble du plan de la galaxie, y compris les sources qui se recoupent, actuellement en cours au sein de l'Association de la CTA, facilitera l'étude des sources d'éclairage uniques, comme indiqué dans le présent document.

La simulation des données DC-1 suit un modèle Spectral simple (loi de puissance ou loi de fin d'indice). Compte tenu des caractéristiques statistiques du rayonnement gamma élevé, la fusion simultanée du modèle de rayonnement et du spectre DC-1 ne permet pas de déterminer si la CTA obtient des caractéristiques d'accélération PeV claires.

Titre : Restes de supernova comme candidats PeVatrons: analyse et modélisation de données simulées de Cherenkov Telescope Array

Mots clés : observation gamma de haute énergie, restes de supernova, Cherenkov Telescope Array, rayons cosmiques galactiques, modèles radiatifs

Résumé :

L'origine du genou dans le spectre des rayons cosmiques aux énergies autour du PeV reste une question ouverte. En raison de leur budget énergétique élevé, les restes de supernovae (SNR) sont des candidats plausibles pour ces dénommés PeVatrons. Les particules chargées accélérées interagissent avec la matière environnante et produisent des pions neutres qui se désintègrent ensuite en rayons γ de haute énergie. Ces rayons γ , qui sont aux énergies du TeV pour les PeVatrons, peuvent ensuite être détectés par des télescopes Cherenkov ou d'autres observations en rayons γ . Dans ce travail de thèse, nous étudions le potentiel du réseau de télescopes Cherenkov CTA à observer de tels rayons γ .

Après avoir sélectionné les candidats potentiels PeVatrons Galactiques présents dans le Data Challenge One (DC-1) de CTA, nous reconstruisons leur distribution spectrale d'énergie (SED) à l'aide du package *ctools*. Si des données mesurées existent à d'autres longueurs d'onde, nous les combinons aux SED simulés pour effectuer une analyse multi-longueur d'onde (MWL). Les SED sont ensuite ajustées à l'aide

de différents modèles radiatifs non thermiques mis en oeuvre dans le logiciel *Naima*, en particulier la composante pion neutre hadronique.

Plusieurs résultats sont obtenus. Les paramètres spectraux reconstruits sont en bon accord avec les paramètres utilisés dans le DC-1. Les simulations donnent ainsi confiance dans le processus d'analyse des données. Parmi les SNRs étudiés, certains candidats PeVatrons potentiels ayant des spectres d'énergie durs sont trouvés. Il est également montré que les données MWL donnent une bonne contrainte pour la modélisation des SED et permettent de déterminer si une composante hadronique est présente dans les données. Si les spectres des SNRs observables avec CTA suivaient ceux simulés pour le DC-1, nous pourrions exclure la plupart des sources en tant que PeVatrons. La combinaison des données de *Fermi-LAT* et des données CTA permettrait cependant de contraindre ou de mesurer les contributions relatives hadroniques et leptoniques à l'émission γ des SNRs. Des améliorations possibles des modèles spectraux à simuler pour le prochain Data Challenge de CTA sont proposées.

Title : Supernova remnants as PeVatron candidates: analysis and modeling of simulated data from the Cherenkov Telescope Array

Keywords : high-energy gamma observation, supernova remnant, Cherenkov Telescope Array, galactic cosmic-rays, radiative models

Abstract :

The origin of the knee in the cosmic-ray spectrum at PeV energies is still an open question. Due to their large energy budget, Supernova Remnants (SNRs) are plausible candidates for these so-called PeVatrons. The accelerated charged particles interact with surrounding matter and produce π^0 particles that consequently decay into high-energy γ rays. These γ rays, which are at TeV energies for PeVatrons, can then be detected by Cherenkov telescopes or other γ -ray observations. In this thesis work, we study the potential of the Cherenkov Telescope Array (CTA) to observe such γ rays.

After selecting potential Galactic PeVatron candidates present in the simulated Data Challenge One (DC-1) of CTA, we reconstruct their spectral energy distribution (SED) by using the *ctools* package. In case measured data at other wavelengths exist, we combine them to the simulated SEDs to perform Multi-Wavelength (MWL) analysis. The SEDs are then fitted

by using different non-thermal radiative models implemented in *Naima* package, including hadronic π^0 component.

Several results are obtained. The spectral parameters are reconstructed in good agreement with parameters used in DC-1. Simulations thus give confidence in the data analysis process. Some potential PeVatron candidates having hard energy spectra are found among the studied SNRs. It is also shown that the MWL data gives good constrain for SED modelling and allows us to determine whether a hadronic component is present in the data. If the spectra of SNRs observable by CTA followed the DC-1 simulation, we could rule out most of the sources as PeVatrons. The combination of *Fermi-LAT* data with CTA data would at the same time enable firm constraints on or measurements of the hadronic and leptonic relative contributions to the γ -ray emission of SNRs. Possible improvements in the input spectral models to be simulated for the next Data Challenge of CTA are proposed.

